Deciphering Neural Population Dynamics in Health and Disease

by

Tibin T. John

A dissertation submitted in partial fulfillment
of the requirements for the degree of
Doctor of Philosophy
(Neuroscience)
in the University of Michigan
2022

Doctoral Committee:

Assistant Professor Omar J. Ahmed, Chair
Professor Victoria Booth
Associate Professor Kamran Diba
Professor W. Michael King
Professor Michal Zochowski

Tibin T John. 2022

tibintj@umich.edu

ORCID iD: 0000-0002-6825-7166

DEDICATION

To my ever-patient family, friends, and puppy Millo, who have waited for my time long enough!

ACKNOWLEDGEMENTS

I would like to express my sincere thanks first to my mentor Omar Ahmed, who 5 years ago brought me to Ann Arbor by promising an exciting exploration of my longstanding interest in the deep principles behind space, time, and speed in the brain, as well as rare data that could make a large impact in our understanding of epilepsy, and this is precisely where we ended up. Thank you so much for your guidance and advice along that path, also teaching me the importance of presenting science in a way that it is easily recognizable and quickly digested, a lesson that will stick with me lifelong. Your support was irreplaceable and I look forward to traveling the roads of future directions that our work has opened up.

Thank you to my dissertation committee for your interest, enthusiasm, and patience, I couldn't have gotten to this point without your insights and feedback. Thanks particularly to Victoria, in whose Computational Neuroscience course I became officially inspired to pursue the spatial information processing problem as mapping sensory inputs to voltage and time-dependent neural processes with no inherent substrate for space. Thanks also to Michal for your inspiring dedication to empirical support combined with clear theoretical reasoning, I hope to find a balance in theoretical but applied neuroscience in my future career much like you have accomplished. Thank you Kamran for your crucial insights to the theta phase coding project and dedication to getting the analysis as thorough and fair as possible, it was an eye-opening experience

and I'm so glad you were open to joining the committee and giving so much useful, specialized feedback even in a short time, I hope we can continue to collaborate on theta phase coding in the future. Thank you Mike for introducing me to the neurophysiology of the vestibular system in an interactive and engaging way that inspired me to consider head movements as supporting a neural code for spatial navigation. Your instruction also fueled my interest to work as a medical scribe with balance disorder patients under the fantastic mentor and neuro-otologist Dr. Greg Basura at Michigan Medicine, who inspired me by example towards the career path of a physician-scientist.

This also would not be possible without the support of my family and friends – thanks to my mother for encouraging me to keep moving forward in a loving way countless times, and to my sister for always being someone I could rely on to talk things through and come out with better understanding regardless of the topic. Thank you to everyone in the Omar Lab for keeping up our mutual enthusiasm over the years, along with frequent coffee breaks and entertaining discussions. I definitely would not have made it here without the always reassuring, wise, and encouraging discussions I had with my best friend Alcides Lorenzo Gonzalez - you have helped me in ways I'll never be able to repay but will keep trying! I have had a fantastic support system here and hope to continue to pay forward this tradition in my next career steps, while keeping in touch with you all as much as possible.

TABLE OF CONTENTS

DEDICATION ii

ACKNOWLEDGEMENTS iii

LIST OF FIGURES viii

ABSTRACT xiii

CHAPTER 1: Introduction 1

1.1 Neural population dynamics in healthy brain function 1

1.1.1 Coordinating neural and environmental dynamics 1

1.1.2 The temporal sequence coding problem 2

1.1.3 The sequence coding problem in spatial navigation 5

1.1.4 Stable spatial coding in hippocampus despite variable running speed 6

1.1.5 Current models of phase precession and theta sequences in place cells 8

1.2 Neural population dynamics in epilepsy 12

1.2.1 Epilepsy as instability in a dynamical system 12

1.2.2 Epilepsy as propensity to excitation-inhibition imbalance 13

1.2.3 Role of FS vs RS cells in animal models of TLE 15

1.2.4 Role of FS vs RS cells in human patients with TLE 16

CHAPTER 2: Time-warped Behaviors are Logarithmically Transformed into Stable Hippocampal Sequences 18

2.1 Abstract 18

2.2 Introduction 19

2.3 Results 23

Spatiotemporal coding and the behavioral time-warp problem 23

The logarithmic theta transform framework 24

Prediction 1: Theta phase is sensitive to the logarithm of remaining time in field 27

Prediction 2: Theta sequences show non-uniform spacing within single cycles 37

Prediction 3: Time-warp (speed change) leads to selective phase shift in theta sequences without corresponding change in phase separation 39

2.4 Discussion 47

Implications for sequence coding 47

Implications for the hippocampal neural code 51

2.5 Materials and Methods 57

Data subjects 57

Data analysis 58

2.6 Acknowledgements 71

2.7 Author Contributions 71

2.8 Supplemental Figures and Tables 71

CHAPTER 3: Two Modes of Inhibitory Shutdown Distinctly Amplify Seizures In Humans 91

3.1 Abstract 91

3.2 Introduction 92

3.3 Results 94

3.4 Discussion 115

3.5 Materials and Methods 117

3.5.1 Patients & Clinical/Research Electrode Placement 118
3.5.2 NeuroPort Recordings, Data Collection & Analysis 121
3.5.3 Cluster isolation quality assessment: Dynamic L_{Ratio} 122
3.5.4 Membrane potential trajectory analysis 124
3.5.5 Computational model 124
3.5.6 Statistical analyses 125
3.6 Acknowledgements 126
3.8 Supplemental Figures and Tables 127
CHAPTER 4: Discussion and Future Directions 145
4.1 Network and cell-intrinsic dynamics interact in health and disease 145
4.2 Comparison to previous studies on distance vs time coding by theta phase 146
4.3 Method of time-keeping in LTT in comparison to previous literature 152
4.4 Future Directions 153
BIBLIOGRAPHY 155

LIST OF FIGURES

Chapter 2:

Figure 2-1. The behavioral time-warp problem for recognition of place field sequences can theoretically be solved using the logarithmic theta transform (LTT). 25

Figure 2-2. Testing logarithmic theta transform (LTT) prediction 1: Theta phase is sensitive to remaining time in place fields in addition to remaining distance in field. 32

Figure 2-3. Testing logarithmic theta transform (LTT) prediction 1 (continued): Theta phase has logarithmic relationship with time remaining in place fields with quantitative specificity. 36

Figure 2-4. Testing logarithmic theta transform (LTT) prediction 2: Theta sequences display a logarithmic spike timing difference gradient, decreasing in phase separation from early to late within theta cycles. 38

Figure 2-5. Testing logarithmic theta transform (LTT) prediction 3: When running speed increases, theta sequences display no change in phase separation, increase in phase-time compression ratio, and decrease in mean phase. 43

Supplementary Figure 2-1. Firing rate level response to time-warp amongst place cells. 74

Supplementary Figure 2-2. Testing logarithmic theta transform (LTT) prediction 1 (continued): Theta phase correlates strongly with remaining time in field within individual fields. 76

Supplementary Figure 2-3. Testing logarithmic theta transform (LTT) prediction 1 (continued): Theta phase correlates strongly with remaining time in field when controlling for distance. 78

Supplementary Figure 2-4. Testing logarithmic theta transform (LTT) prediction 1 (continued): Theta phase has logarithmic relationship with theta-discretized distance remaining in place fields with quantitative specificity. 79

Supplementary Figure 2-5. The cognitive space-warp problem for warping of spike time patterns at different theta sequence trajectory lengths can be solved using the logarithmic theta transform (LTT) with respect to distance. 81

Supplementary Figure 2-6. Illustration of how logarithm base controls curvature and its coding properties. 82

Supplementary Figure 2-7. Testing logarithmic theta transform (LTT) prediction 2: Theta sequences display a logarithmic spike timing difference gradient, decreasing in phase separation from early to late within theta cycles. 83

Supplementary Figure 2-8. Testing logarithmic theta transform (LTT) prediction 3 (continued): Distance within and between fields are well-controlled across speed groups, while time between fields is allowed to vary. 84

Supplementary Figure 2-9. Effect of realistic accelerations and decelerations on LTT predictions, empirical phase precession, and empirical theta sequence properties..... 86

Supplementary Figure 2-10. Testing logarithmic theta transform (LTT) prediction 1 (continued): Theta phase has logarithmic relationship with continuous time (total theta phase) remaining in place fields with quantitative specificity. 87

Supplementary Figure 2-11. Testing logarithmic theta transform (LTT) prediction 1 (continued): Theta phase has logarithmic relationship with continuous distance remaining in place fields with quantitative specificity. 88

Supplementary Figure 2-12. Testing logarithmic theta transform (LTT) prediction 1 (continued): Theta phase at given distance becomes lower at higher running speeds in individual fields. 90

Figure 3-1: Human neocortical inhibitory and excitatory neurons have different temporal profiles relative to secondarily generalized focal seizure progression on local electrodes 105

Figure 3-2: Analyzing unit subpopulations by isolation quality demonstrates consistent cell-type specific activity profiles and cessation order despite changing unit amplitude and noise structure. 107

Figure 3-3: Fast-spiking inhibitory neurons, when still firing, impede the spread of epileptic traveling waves. 109

Figure 3-4. Cessation of individual FS unit activity is consistently associated with inferred membrane potential signatures of depolarization block, despite prior hyperpolarized pauses 111

Figure 3-5. Mechanistic model of unit dynamics across seizure progression: inhibition followed by over-excitation in conductance-based neuron model reproduces key features of extracellular unit behavior during seizures. 113

Extended Data Figure 3-1: Human neural activity classification 128

Extended Data Figure 3-2: Human neocortical inhibitory and excitatory neuron activities have distinct temporal profiles relative to secondarily generalized focal seizure progression on local electrodes, Patient A, Seizure 2 130

Extended Data Figure 3-3: Human neocortical inhibitory and excitatory neuron activities have distinct temporal profiles relative to secondarily generalized focal seizure progression on local electrodes, Patient C, Seizure 2.....131

Extended Data Figure 3-4: Human neocortical inhibitory and excitatory neuron activities have distinct temporal profiles relative to secondarily generalized focal seizure progression on local electrodes, Patient B, Seizure 1.....134

Extended Data Figure 3-5: Cluster isolation quality assessment suggests RS units are well-isolatable across seizure despite changing unit amplitude and noise structure, allowing analysis of firing rate changes across seizure. 135

Extended Data Figure 3-6: Cluster isolation quality assessment suggests RS and FS units on same channel are well-isolatable across seizure despite changing unit amplitude and noise structure, allowing analysis of firing rate changes across seizure for multiple patients. 138

Extended Data Figure 3-7: Cessation of individual RS unit activity is consistently associated with inferred membrane potential signatures of depolarization block, despite prior pauses139

Extended Data Figure 3-8: Seizure progression is consistently associated with extracellular signs of depolarization block preceded by inhibition in single units. 141

Extended Data Figure 3-9: Seizure progression is consistently associated with extracellular signs of depolarization block preceded by inhibition in single units. 144

Figure 4-1. Even with dominant distance coding, just 20% time dependence of phase precession leads to contraction of spike time patterns with running speed. 149

Figure 4-2. Even with dominant distance coding, logarithmic time coding of just the time-dependent portion of phase precession leads to stabilization of spike time patterns with respect to running speed. 151

ABSTRACT

The dynamics of neural populations must maintain stability while also performing behaviorally useful representation and processing of rapidly changing environmental inputs. How the nervous system accomplishes this flexible coordination of its own dynamics with that of the sensory stream, while also maintaining its own stability, is poorly understood. However, answers to this puzzle promise better understanding of neurological disorders involving dynamic instability such as epilepsy, as well as uncovering evolutionarily-optimized algorithms for processing information that evolves over time, more robustly than our current technology. Given that relevant information can change rapidly in the case of spatial navigation at different running speeds, hippocampal neural circuits that support both externally-tuned spatial cognition and internally stable memory must particularly employ such mechanisms. In Chapter 2, we propose and find empirical support for a novel framework that allows hippocampal cells to maintain stability in the face of rapidly changing external inputs, called the logarithmic theta transform (LTT), as implemented by the nonlinear shape of theta phase precession in individual place cells. Findings suggest how space and time coding mechanisms in hippocampal networks come together to stabilize the internal organization of place cell activity within theta cycles. In Chapter 3, we investigate mechanisms controlling the rapid progression of seizures in epilepsy patients with a focus on fast-spiking inhibitory neuronal activity. These findings suggest that cell-type

specific propensities to depolarization block play an important role in the evolution of sequential neural dynamics during focal seizures with secondary generalization, with implications for therapeutic approaches needing the proper timing relative to this sequence. Overall, this work points toward properties on the level of individual cells as supporting stable population dynamics that are nevertheless flexible in responding to changing information.

CHAPTER 1: Introduction

1.1 Neural population dynamics in healthy brain function

1.1.1 Coordinating neural and environmental dynamics

Deciphering the coding system used by the brain to internally represent and efficiently process information about the environment is a key task to understanding brain function and inspire better information processing algorithms. At the core of such neural coding is a behaviorally useful mapping between the rules governing environmental patterns and the rules governing representational neural activity. The dynamics of useful representations and those of the environment need not have the same governing rules, yet must be coordinated in a functional and responsive nervous system. These external and internal pattern generating systems, also referred to as implicit and explicit neural spaces, respectively (Zemel et al., 1997), often cannot be coupled in a trivial way. For example, sensory and motor representations at the interface of the nervous system with the environment may only need signal-transducing ion channels or neurotransmitter release to couple neural and behavioral information. However, central pattern generators in the brainstem or spinal cord that drive and sustain their own activity necessitate more dynamic strategies to relate ongoing neural and behavioral activity,

such as by using oscillatory resonance and phase resetting to coordinate otherwise independently evolving processes (John et al., 2014; Phillips et al., 2019; X.-J. Wang, 2010; Yuste et al., 2005). When environmental dynamics change in implicit space, neural states should be correspondingly updated without violating the internal rules of explicit neural or representational space. Considering the neural coding mechanisms that simultaneously satisfy the rules of dynamics in both the implicit and explicit systems eliminates a large part of hypothesis space about neural function. Thus, specifying the method of mapping between environmental dynamics and neural dynamics will be a critical component of the effort to understand neurophysiology. Furthermore, observing when neural biophysics and the physics of the environment would naturally diverge, but nevertheless become coupled by the operations of local neural circuits, is a promising approach to discovering fundamental principles of neural coding. One prominent instance of natural divergence between external input dynamics and internal neural dynamics occurs in the problem of temporal sequence coding.

1.1.2 **The temporal sequence coding problem**

Representing a sequence requires forming symbols for a set of environmental elements and the order in which they present across time. However, inputs do not arrive at sense organs such that the identity of the environmental elements and their relative order are unambiguously represented by features of neural activity. Instead, sensory transduction creates initial neural representations that are sensitive to input timing and magnitude but not necessarily to segmented element identity or order. Robust representations of these properties must be computed through combination and transformation of evoked sensory activity by internal neural dynamics (Long et al., 2010; Vogels et al., 2005). In

particular, brain circuits must represent this sequence information in a way that is robust against noise and yet receptive to updates based on changing external inputs, i.e. in a way that is both stable and flexible.

The basic neural principles behind the stable and flexible representation of time and temporal sequence can be experimentally studied in central pattern generators, which accomplish this par excellence (Marder & Bucher, 2001; J. E. Rubin, Shevtsova, et al., 2009). One such model system is that of the respiratory rhythm generator located in the brainstem, with time-keeping methods having implications for higher order circuits that likely reused these principles over the course of evolution (Katz, 2016; Yuste et al., 2005). This rhythm generating circuit can be thought of as keeping track of time and temporal sequence by neuronally representing and computing the time between the broad phases of inspiration and expiration.

What neural or biochemical entity does the brainstem wait for in order to signal the start of our next breath? A rich history of experimental and theoretical research has revealed the importance of the dynamics of bursting in individual cells guided by their slow intrinsic conductances, such as the persistent sodium conductance, in determining the timing of inspiration (Butera et al., 1999; Koizumi & Smith, 2008). Furthermore, these initially unsynchronized neurons dynamically couple their bursts with each other and use the timing of the spread of their synchrony across the whole network (Ashhad & Feldman, 2020; Smith et al., 2009) to create the breathing rhythm as a high-dimensional, robust oscillator with a large dynamic range of frequencies. These timing

circuits generate stable rhythms despite using the noisy components of stochastically firing neurons because of weakly coupled oscillators from which synchrony emerges (J. Rubin & Smith, 2019) without a common, potentially unreliable, central drive. Because of the voltage-dependence of the frequency of their bursting neural components (Koizumi & Smith, 2008; Phillips et al., 2019), these circuits can nevertheless retain a large dynamic range in response to inputs like blood oxygenation levels and higher order inputs from cortex. Because these neurons also display criticality, resting in between silent, tonically firing, and bursting states (Butera et al., 1999), these circuits can also change their frequency rapidly in response to external inputs without affecting their oscillatory stability, generated on a more network level as a “group pacemaker” (J. E. Rubin, Hayes, et al., 2009; Smith et al., 2009). As a result, the temporal sequence of inspiration, post-inspiration, and expiration is stably represented by ventral medullary circuits despite also being highly responsive to external inputs that modulate its pace and timing (Smith et al., 2013).

Studies in higher order neural circuits involved in temporal sequence coding have also pointed towards the importance of internally generated dynamics operating stably yet in harmony with external drives, dubbed the “stability-flexibility dilemma” (Liljenström, 2003). The requirements for stability and flexibility are particularly prominent in the circuits responsible for representing space since the code is stable over time yet highly receptive to environmental cues. The processes determining the timing of spikes relative to the theta rhythm and relative to other cells coding for space are not

completely understood, but they are likely required to exhibit both stability and flexibility in order to constitute an effective sequence coding scheme.

1.1.3 **The sequence coding problem in spatial navigation**

Identifying and representing sequences is a core challenge in the process of constructing a cognitive map of one's surrounding environment from sensory and motor signals evolving over time (Tolman, 1948; Wikenheiser & Redish, 2015b). Such spatial computation involves a significant dimensionality reduction from a sensory stream that changes across time and across an array of dedicated sense receptors into a representation of connectedness amongst segmented features (Howard et al., 2014). The ability to retain an independence from certain aspects of sensory input, such as intensity or duration, despite a sensitivity to relationships amongst those inputs, such as distance and order, allows spatial cognition to apply successfully to many different, even novel, environments (Kaplan et al., 2012). Even in the case of recognizing a spatial sequence in an essentially one-dimensional environment, sensory inputs are constantly changing as an organism moves forward at various speeds. Despite this, the spatial map construct in which all of this occurs must remain stable in keeping with the objective structure of the environment. Sensory inputs and the internal neural activities computing their spatial context are thus both dynamic, each evolving in time according to their own rules which often naturally mismatch. Spatial map or sequence coding is consequently a promising model problem testing the limits of effective coordination between otherwise independent internal and external dynamics, making it fruitful to elucidate the precise strategies the hippocampal formation uses to accomplish it.

1.1.4 Stable spatial coding in hippocampus despite variable running speed

The hippocampus is necessary for forming new memories and is also essential to constructing our notion of space and time (Eichenbaum 2017). When rats are exposed to a new environment while experimenters make electrical recordings from the dorsal hippocampus, cells emerge that increase their firing rate only when the rat is at a particular location in the environment, and are thus named place cells (O'Keefe & Dostrovsky, 1971). Two major models describing how the hippocampus represents spatial information are the continuous attractor network and oscillatory interference model, each purporting a different feature of neural activity that changes with speed to stably track spatial patterns. Continuous attractor networks consist of an abstract 2D plane of position-encoding neurons with Gaussian-shaped local excitatory connectivity and global inhibitory connections (Samsonovich & McNaughton, 1997). They implement path integration of externally generated speed signals through the movement of a stable bump of activity that is self-sustained and contained by this connectivity to represent position as a vector of firing rates across the population. The speed of the activity bump in this model is determined by the strength of spatially asymmetric influences relative to symmetric influences such as recurrent synaptic strengths or afferent input. Information about the self-motion must be relayed in a form that increases asymmetry only in the direction of motion and in proportion to the speed of that motion (McNaughton et al., 1996). Errors accumulate in the path integration strategy so this model also requires a mechanism for allowing sensory input to robustly recalibrate the position of the bump, which is possible due to the stimulus integration property of such attractor networks (Clark and Taube, 2012). How the finely-tuned synaptic connections would self-organize

to implement a continuous attractor network that is appropriately receptive to self-motion signals and sensory reset is an open question. The observed saturation and diversity of the response to speed across the hippocampal formation (Hinman et al., 2016) should also be taken into account in the connectivity of future attractor models. Thus, while a continuous attractor network is dynamically stable by virtue of its connectivity, how the bump of activity representing position can be reliably moved by incoming speed signals to alter the symmetry of connections towards the direction of motion remains an open question.

Rather than expressing spatial position solely in a population firing rate vector, the oscillatory interference model proposes that such information can also be represented on a finer timescale in the phase difference between neural oscillators, which are found extensively in spatial navigation circuits (Burgess et al., 2007). This model rests on the mathematical fact that the time integral of the frequency difference between sinusoids is precisely equal to their phase difference and thus their degree of constructive interference at any given time. This suggests a natural way to implement the instantaneous storage and readout of the result of path integration if speed were encoded by frequency difference between neural oscillators that sum together as proposed by this model. This model also predicts a coupling between place fields and the phase of spiking in proportion to the frequency difference of the oscillators. Nevertheless, this integration of speed is still subject to error accumulation and this model leaves open the question of how speed would lead to precise changes in frequency despite the inherently noisy variability of theta rhythm and neural oscillator

cycle durations. These models thus both leave open the question of precisely how position become stably coded by place cells by an internal neural code despite fluctuations in external inputs due to speed changes. The logarithmic theta transform model is proposed as a possible solution implemented by hippocampal place cell circuits in Chapter 2, based on the spike timing based code exhibited by these cells called theta phase precession, as explored next.

1.1.5 Current models of phase precession and theta sequences in place cells

Interestingly, place cells not only systematically change their firing rate depending on the location of the rat, but also the time at which they fire bursts of spikes on a tens of milliseconds timescale with respect to individual cycles of the total population drive oscillating at 4-12Hz (O'Keefe & Recce, 1993). In particular, place cell spikes start near the end of these ~100 millisecond cycles of this rhythm (the theta rhythm) when the animal enters the place specific to that cell (the cell's place field). Place cells then fire earlier and earlier on successive bursts of spikes in direct proportion to the distance the animal has travelled within its place field. This phenomenon is known as phase precession (O'Keefe & Burgess, 2005; O'Keefe & Recce, 1993). Cells with overlapping place fields also organize their spike times into sequences that span half of a theta cycle, i.e. ~50ms, based on the order of their traversal (Dragoi & Buzsáki, 2006; Schmidt et al., 2009). How spike times are made to be organized into sequences on the timescale of milliseconds so as to reflect behavioral events that occur on the time scale of seconds (movement in space) is unknown, but there are several theories (Booth & Bose, 2001; Lengyel et al., 2003; O'Keefe & Burgess, 2005; Tsodyks et al., 1996). This

organization could provide the link between sensory input during behavior and the rich field of learning through synaptic plasticity, which traditionally operates on the millisecond timescale through mechanisms such as spike timing-dependent plasticity (Lever et al., 2002; Shen et al., 2008). Knowing these relationships, and their sensitivity to internal dynamics and external drives, is crucial to discovering how the hippocampus organizes learned information stably and flexibly, sensitive to spatial properties but invariant to other contingencies of the sensory stream.

One of the first major questions that emerged after the discovery of phase precession was how it is generated in terms of cellular and network mechanisms in relation to its information content, and the related question of whether it constituted an independent signal from the firing rate signal emitted by place cells (Foster & Wilson, 2007; Huxter et al., 2003; Mehta et al., 2002). It was already clear that the phase code is at least somewhat independent from the place field firing rate in that it showed a monotonic relationship with position within a place field, whereas firing rate is modal, with both rising and falling branches. Models emerged with differing degrees of dependence between the firing rate and spike timing codes of place cells, with some proposing an asymmetric ramping drive across the field that crosses the rhythmic inhibitory theta drive at earlier and earlier phases with each passing cycle while also driving firing rate (Mehta et al., 2002). Others suggested a network-based look-ahead mechanism in which theta phase is determined by a moving bump attractor that moves across place cells on the timescale of each theta cycle, independent of a more sensory-driven input determining firing rate by moving the bump attractor on the timescale of behavior

(Tsodyks et al., 1996; Y. Wang et al., 2015). This network mechanism within theta cycles also inspired a third concept potentially independent from both place cell firing rate and phase precession in being a property of multiple place cells, i.e. the theta sequence (Foster & Wilson, 2007). Synaptic interactions between place cells could allow sequences of place cells on the behavioral scale of their partially overlapping place fields to be represented in their relative spike timing within theta cycles, forming theta sequences.

The independence of the existence of phase precession in individual place cells and that of theta sequences amongst a group of precessing cells has been demonstrated and attributed to the coordination or disagreement of the phase offset of the participating cells (Feng et al., 2015). Both theta phase precession and theta sequences exist without place fields when a spatial navigation tasks includes a “space-clamped” portion of a running wheel where hippocampal cells form “episode fields” or “time fields” that are similarly organized in term of spike timing within theta cycles as place fields (Pastalkova et al., 2008). Furthermore, the independence of place fields from theta sequences and phase precession was shown by blocking medial septum input driving the theta rhythm without abolishing the place field firing rate code (Y. Wang et al., 2015). The spatial extent of the phase coupling of spikes with the theta rhythm can also be vastly larger than the spatial extent of the firing rate based place field and show strong asymmetry relative to the place field center (Souza & Tort, 2017). All of these point towards a strong independence of the theta phase code from the place field rate

code in hippocampal cells and suggest a different mechanism and function for theta phase as opposed to place fields, likely related to sequence coding.

Accordingly, the asymmetry of phase precession across the place field center has been investigated for the clues it may offer towards how the hippocampus accomplishes sequence coding. Fitting multiple normal distributions to phase precession point clouds showed that phase precession is best approximated by two normal distributions, the first covering the later 180 degrees of the theta cycle and the 2nd covering the first 180 degrees of a theta cycle, with the former showing a higher phase-position correlation (Yamaguchi et al., 2001). A similar finding of more phase variability in the 2nd half of a place field (Dragoi & Buzsáki, 2006) supports a significant difference between first and second halves of the phase precession curve. Furthermore, differing power of fast and slow gamma rhythms in the respective dendritic regions for entorhinal cortical and CA3 inputs to CA1 place cells during the first and last halves of place fields (Fernández-Ruiz et al., 2017) suggests an important role for differences in phase precession in these two halves of a field in sequence coding. In Chapter 2, we propose the overall shape of phase precession is logarithmic to account for these differences across a place field, and as a novel mechanism to accomplish scale-invariant spatial sequence coding in a way comparable to J.J. Hopfield's logarithmic latency coding framework for analog pattern recognition (Hopfield, 1995).

1.2 Neural population dynamics in epilepsy

1.2.1 Epilepsy as instability in a dynamical system

Epilepsy is a neurological disorder characterized by a propensity to seizures, in which internal, explicit dynamics in neural circuits not only fail to adequately represent external, implicit dynamics in the environment or body, but also are dysfunctional in themselves. The dysfunction of a seizure is largely characterized by instability, or loss of equilibrium, which can be understood in the mathematical framework of dynamical systems. This framework is particularly needed because neural networks behave with nonlinear dynamics: their overall behavior is not always proportional to the activity of their underlying ion channels, neurons, and synapses. Dynamical systems theory offers a powerful geometric and analytical framework for thinking about the behavior of such nonlinear systems and has been extensively used to model what causes the dramatic transitions between normal and epileptic brain states (Jirsa et al., 2014; Silva et al., 2003). These models are characterized by so-called stable and unstable fixed points, regimes of the system that are either attracting or repelling, respectively. When a neural network is in a stable healthy regime, perturbations (inputs) such as sensory or electrical stimulation, or even interictal spikes (Avoli et al., 2006; Gotman, 1991), cannot easily switch this system into an epileptic state – the network absorbs the hit; it shakes, but remains resilient and quickly returns to its stable fixed point in the normal regime. All is well and the healthy regime is still standing strong. However, as a key parameter of the network – its overall excitability – slowly increases, the network becomes less resilient to perturbations. Exactly the same input as before, be it an interictal spike or electrical stimulation, can now severely rattle this excitable network and lead to

catastrophic changes (for the aficionados: a fold bifurcation best describes this loss of stability). The healthy state now falls dramatically and suddenly, replaced by an epileptic state. Is there a warning sign for this progressive network instability, for this slow loss of resilience? In dynamical systems theory, the process leading up to the tipping point is often characterized by “critical slowing” (not to be confused with the slowing seen in some EEG signals during and after seizures). Critical slowing refers to the fact that as a network starts to lose its resilience, it is much slower to recover from any perturbations (Maturana et al., 2020). This suggests a possible way to probe a neural network to see if it is starting to lose its resilience: weakly stimulate it at different times and see how long it takes to return to baseline. When the network starts to take a very long time to recover, then there might be a seizure around the corner. The apparent culprit is the interictal spike or electrical stimulation, belying the deeper contribution of a slowly changing excitability (bifurcation) parameter (Somjen, 2004; Ziburkus et al., 2006). Thus, the dynamical systems perspective allows for building intuition about the non-linear physiology of neural population activity surrounding seizures, which can then be applied to understanding the roles of the pathophysiological mechanisms themselves. In turn, this opens up the possibility of intervening to restrain this pathophysiology towards the goal of seizure freedom.

1.2.2 **Epilepsy as propensity to excitation-inhibition imbalance**

The physiological substrate of dynamic instability in epileptic seizures is thought to be in the transient loss of balance between excitatory and inhibitory neural activity, favoring excessive excitatory activity (Sritharan & Sarma, 2014; Žiburkus et al., 2012). Such

balance is in turn typically maintained through microcircuit organization that prevents excessive recurrent excitation, such as feed-back inhibition (Paz & Huguenard, 2015), feed-forward inhibition (Trevelyan et al., 2007), and the relative placement of inhibitory and excitatory synapses on excitatory cells favoring inhibitory override of excitatory input (Megías et al., 2001; Trevelyan & Schevon, 2013). The relative timing of spikes amongst inhibitory and excitatory neuron subpopulations, and the size of those recruited subpopulations, also determines their balance on a fine timescale, such that pathologically increased synchronization across a population can lead to epileptic seizures and the often associated high frequency oscillations (Charupanit et al., 2020; Weiss et al., 2016) and large amplitude spike potentials (Avoli et al., 2006). Even beyond microcircuit activity balance, factors from the extracellular matrix including its volume (Leifeld et al., 2022) and its concentration of potassium ions (Fisher et al., 1976; Somjen, 2004) can alter the passive electrophysiological properties of neurons to initiate or sustain activity imbalance. Thus, the cause of a temporary loss in sufficient inhibitory restraint in epilepsy can be manifold, making fine scale cell-type specific population-level, microcircuit-level, and even transmembrane voltage-level information crucial in understanding epileptic pathophysiology in any given case. Localizing the pathology will likely advance our understanding most efficiently, and the most common localizable form of epilepsy is temporal lobe epilepsy (TLE), in which seizures originate or primarily involve circuits in the temporal lobe (Bell et al., 2011; Weiss et al., 2016). Much experimental and theoretical work on how TLE manifests in intact animal models and brain slice models points towards deficits and excesses in activity in specific cell types as playing specific roles at different times during seizure onset and progression.

1.2.3 **Role of FS vs RS cells in animal models of TLE**

The broad cell type of most interest in investigating mechanisms initiating and supporting seizures is the GABAergic neuron, given the purported role of inhibition as a protective restraint against imbalanced hyperactivity as discussed above. In terms of how GABAergic neurons contribute to seizures, however, studies point to a variety of mechanisms including excessive activity and diminished activity. For example, recordings from in-vitro models of epilepsy suggest seizure-like events are sustained by alternating bursts of action potentials in excitatory (regular spiking or RS-like) neurons and inhibitory (putative fast-spiking or FS, parvalbumin-positive) cells, in which inhibitory cells are hyperactive (Ziburkus et al., 2006). FS cell activity can also become diminished due to inhibition by other types of inhibitory cells becoming overactive, facilitating seizure progression (Khoshkhoo et al., 2017; Miri et al., 2018). Other studies point toward a loss of effective inhibition during seizure initiation due to chloride ion accumulation raising the equilibrium potential of ionotropic GABA receptors (Buchin et al., 2016), depletion of GABA neurotransmitter release (Z. J. Zhang et al., 2012), or inhibitory neurons reaching depolarization block (Cammarota et al., 2013) in which the inactivation gate of spike-generating sodium ion channels becomes prolongedly closed due to excessive depolarization. Given this variety of cell-type specific mechanisms contributing to seizures in animal models, it is necessary to evaluate the relevance of such mechanisms in human patients where each factor in animal model studies may or may not also be involved.

1.2.4 **Role of FS vs RS cells in human patients with TLE**

Data from human patients on mechanisms actively contributing to seizures is rare, given that such recordings are inherently invasive and can only be obtained under the specific circumstance of TLE patients undergoing surgical resection treatment. The limited existing evidence from neocortical recordings in human TLE patients suggests that inhibitory neuron activity increases prior to seizure onset (Truccolo et al., 2011), potentially representing the activity of a feedforward inhibitory restraint mechanism that ultimately fails (Trevelyan & Schevon, 2013). There is also evidence that the fine-scale temporal pattern of spiking activity during seizures in humans is related to the oscillatory state more coarsely characterizing the seizure, with gamma-band (40-60 Hz) local field potential oscillation-related seizures involving irregular and asynchronous firing amongst both putative FS and putative RS cells, while seizures characterized by spike-wave complexes involved fine timescale synchrony also in both putative FS and putative RS cells (Truccolo et al., 2014). These suggest different microcircuit mechanisms sustaining these seizures, based on either population-wide activity levels or relative individual cell spike timings, respectively. These studies point toward the need to obtain more mechanism-specific information from recordings in human patients.

In Chapter 3 here, we start to address this need by classifying units from extracellular depth electrode recordings in TLE patients into the excitatory RS cell and inhibitory FS cell categories. We find evidence supporting the mechanism of depolarization block of FS cells explaining this dynamic as well as spike amplitude changes over the course of seizures in humans, inferring transmembrane potential changes beyond just

extracellularly detected spike times. We suggest a slowly changing factor such as accumulating potassium ions in extracellular space as driving this change, similar to the bifurcation or excitability parameter referred to in the above section on a dynamical systems perspective on epilepsy. The plausibility of this mechanism is shown with a computational model of spike amplitude in relation to holding potential. This mechanism could suggest novel treatment approaches for patients with epilepsy grounded in its timing relative to this cell-type specific, population activity sequence.

CHAPTER 2: Time-warped Behaviors are Logarithmically Transformed into Stable Hippocampal Sequences

2.1 Abstract

The mammalian brain evolved to robustly encode spatial sequences despite time-warp caused by movement at variable speeds, but time-warped behaviors are incompatible with traditionally-assumed fixed neural coding schemes. Here, we propose and empirically validate an alternative framework – the logarithmic theta transform (LTT) – that can convert variable behavioral time into stable neural spike timing patterns that do not change with speed. LTT makes three predictions about hippocampal place cells that go beyond previous assumptions: 1) a logarithmic theta-phase curve; 2) non-uniform sequence spacing within individual theta cycles; 3) phase-shifted theta sequences at faster running speeds. Analysis of place cells during spatial exploration confirms each prediction. We discover that the hippocampus implements LTT using a scaling-factor of 1.4, identical to the scaling-factor governing the spacing of entorhinal grid modules. Thus, LTT represents an evolutionarily-optimized neural algorithm for stable encoding of information despite the warping of time by natural speed variation.

2.2 Introduction

Facile processing of sequence information is critical for an organism to attain predictive control over its environment, yet representing sequential inputs that present on the variety of timescales relevant to natural behaviors is notoriously difficult (Burgess and Hitch, 2006; Hopfield and Brody, 2001; Howard et al., 2015). The hippocampal formation is likely to implement evolutionarily-optimized codes for handling spatiotemporal sequence information, as it is necessary for episodic memory across time (Buzsáki, 2005; Scoville and Milner, 1957; Spiers et al., 2001) and for navigation across time (Chersi and Burgess, 2015; O'Keefe and Nadel, 1978). One of the hippocampus's key computational units is the place cell (O'Keefe and Dostrovsky, 1971; O'Keefe and Nadel, 1978; Redish, 1999), whose activity is generally restricted to a particular location in an environment, corresponding to its place field. However, a given place cell can have multiple fields (Fenton et al., 2008; Park et al., 2011), and the positions of these fields change in different environments (Bostock et al., 1991; Lever et al., 2002), suggesting this neural activity constitutes a population code for position or sequence in which a single cell's field is meaningful only relative to the co-occurring activity of other place cells. This sequence-coding activity is generated by both internal and external drives (Dragoi, 2013; Pastalkova et al., 2008).

Manifestations of internal coordination between co-active place cells can be seen in patterns in the local field potential (LFP) that permeate the hippocampal formation. The LFP shows high amplitude oscillations in the theta (4-12 Hz) frequency range, particularly during spatial navigation (McNaughton et al., 1983; O'Keefe and

Dostrovsky, 1971). This high amplitude extracellular rhythm implies precise temporal summation involving widespread synchronization of activity on the sub-second scale amongst hundreds of hippocampal cells (Buzsáki et al., 2012; Kajikawa and Schroeder, 2011). Thus, describing place cell activity with respect to the hippocampal theta rhythm is an important window into the coordination responsible for constructing a spatiotemporal sequence code from individual place fields. Indeed, prominent patterns have been discovered in the regions of overlap between place fields in the rat, in the form of their coordination with the theta rhythm and with each other, termed theta phase precession (Huxter et al., 2003; O'Keefe and Recce, 1993; Skaggs et al., 1996) and theta sequences (Dragoi and Buzsáki, 2006; Foster and Wilson, 2007; Skaggs et al., 1996), respectively. Hippocampal phase coding during navigation is evolutionarily conserved, having been observed across other mammalian species including mice (Mou et al., 2018), bats (Eliav et al., 2018), and even humans (Qasim et al., 2021). Thus, the rules governing place cell activity within theta cycles likely point toward powerful neural strategies for achieving robust sequence coding.

What does theta phase precession encode? Foundational studies have systematically explored the behavioral correlates of the theta phase of spikes from place cells to reveal what information it represents during spatial navigation such as distance travelled or time elapsed within a field (Jeewajee et al., 2014; Schmidt et al., 2009). These support the optimality of distance correlations when aggregating data across all laps but leave open the possibility of some additional time correlation when considering single passes through a field. While some studies have further supported a distance coding function

for theta phase precession by advancing phase in proportion to instantaneous speed across time (Geisler et al., 2007; Huxter et al., 2003; O'Keefe and Recce, 1993), other work challenges this solution by pointing to time-dependence apart from simple distance phase coding (Gupta et al., 2012; Itskov et al., 2008; Parra-Barrero et al., 2021).

An open question persists about the nature of theta phase precession beyond the behavioral information it may code for. Several studies have noted that phase precession follows a nonlinear shape across a place field (the non-linear curvature of this shape has led to it being sometimes referred to simply as a "banana shape"; Huxter et al., 2003; McClain et al., 2019; Mehta et al., 2002). However, in explorations of its mechanisms and functions, phase precession is still modeled as approximating a linear shape (Burgess, 2008; McClain et al., 2019), notwithstanding phenomenological models that incorporate this shape for the purpose of biophysical realism (Jahnke et al., 2015). There is currently no framework attributing a function to the nonlinear shape of phase precession, which has heretofore justified the use of a first-order linear approximation despite visual evidence to the contrary. Furthermore, this linear framework makes the problematic (from a decoding perspective) prediction of a variable time separation between coded elements of a sequence (Geisler et al., 2007; Huxter et al., 2003), rendering the spacing of sequence elements expected by temporal summation at downstream decoders ambiguous (Figure 1). For spatial sequence coding, this framework is particularly insufficient because natural speed variability implies a corresponding wide range of neural timescales to which downstream sequence decoders must display invariance if they are to represent a stable map of space. The

problem of robustness to different timescales has been recognized in other behaviors such as word recognition within speech naturally occurring at different cadences, and was suggested to be solved by the neural coding strategy of logarithmic latency encoding (Hopfield, 1995, 1996). However, the potential utility of a similar framework for creating a stable neural code for space at different running speeds (Sheeran and Ahmed, 2020) has not yet been explored.

Here, we propose that a logarithmic framework is utilized for time-warp invariant sequence coding in hippocampal place cells, a theoretical framework that we call the logarithmic theta transform (LTT). LTT makes three explicit, non-trivial predictions about the evolution of theta phase statistics during movement, the form of sequence representations within individual theta cycles, and the coding of speed changes in properties of theta phase precession. Using large datasets with > 1000 place cells, we empirically validate each of these 3 predictions. Remarkably, our analysis of place cell temporal dynamics show an implementation of LTT in the hippocampus using a scaling-factor of 1.4, identical to the scaling-factor governing the relative spacing of entorhinal grid modules (Barry et al., 2007; Stensola et al., 2012). This suggests the possibility of a common system connecting hippocampal and cortical circuits for robustly processing episodic information despite behaviorally natural changes in the spatiotemporal scale of this information.

2.3 Results

Spatiotemporal coding and the behavioral time-warp problem

A stable representation of space requires that changing speed does not change the underlying representation of space, and, accordingly, this speed invariance of the theta phase code is supported in previous studies (Geisler et al., 2007; Huxter et al., 2003; Jeewajee et al., 2014). However, how speed-invariance arises in the theta phase code is not clear and even problematic for current theories about the nature of theta phase precession. In particular, the following problem arises when considering downstream readers of place field sequences (Buzsáki, 2010), which we refer to as the behavioral time-warp problem (Figure 1): If temporal sequence information is to be preserved between place fields, it first becomes necessary to have a physical representation of time such as a delay line system to recognize time-order (Hopfield, 1996; Howard et al., 2015; Tank & Hopfield, 1987). This representation may correspond to active processes generating dendritic sequence sensitivity on the timescale of a theta cycle for place cell sequences (Branco et al., 2010). However, such a physical representation of a time-order template involving linear time compression would suffer from rigidity and fail to achieve sufficient temporal summation in the case of multifold behavioral time warp (Figure 1), in which the sequence of interest can occur over vastly different time intervals. We note that this would be the case for a sequence of place fields being traversed at the wide range of running speeds that mammals exhibit during spatial navigation, covering multiple orders of magnitude and showing significant variation even in laboratory conditions as analyzed here (Supplementary Figure 1). Still, the theta phase differences between these overlapping place fields are also invariant to speed

(Geisler et al., 2007), as we verify in our later results section on theta sequence properties. This points to a time-order sensitive code produced by a presently unknown neural algorithm in hippocampal circuits that solves the behavioral time-warp problem.

The logarithmic theta transform framework

We propose the LTT solution in hippocampal circuits, inspired by foundational theoretical work solving the analog match problem (Hopfield, 1995, 1996). The key is a change from a rigid template representation of time between sequence elements into a logarithmic representation of the time between them, leading to equivalent downstream post-synaptic coincidence detection across a range of timescales. We illustrate how this would apply to place field sequences at different running speeds in Figure 1B,C in the form of phase precession implementing a nonlinear time compression and transformation. If this transformation is logarithmic, the resulting spike timing code retains the same pattern for a wide range of speeds, with an overall offset representing the warp factor. A temporally summating post-synaptic neuron can then respond to these input sequences identically, regardless of the level of time-warp, after this transformation (Figure 1B).

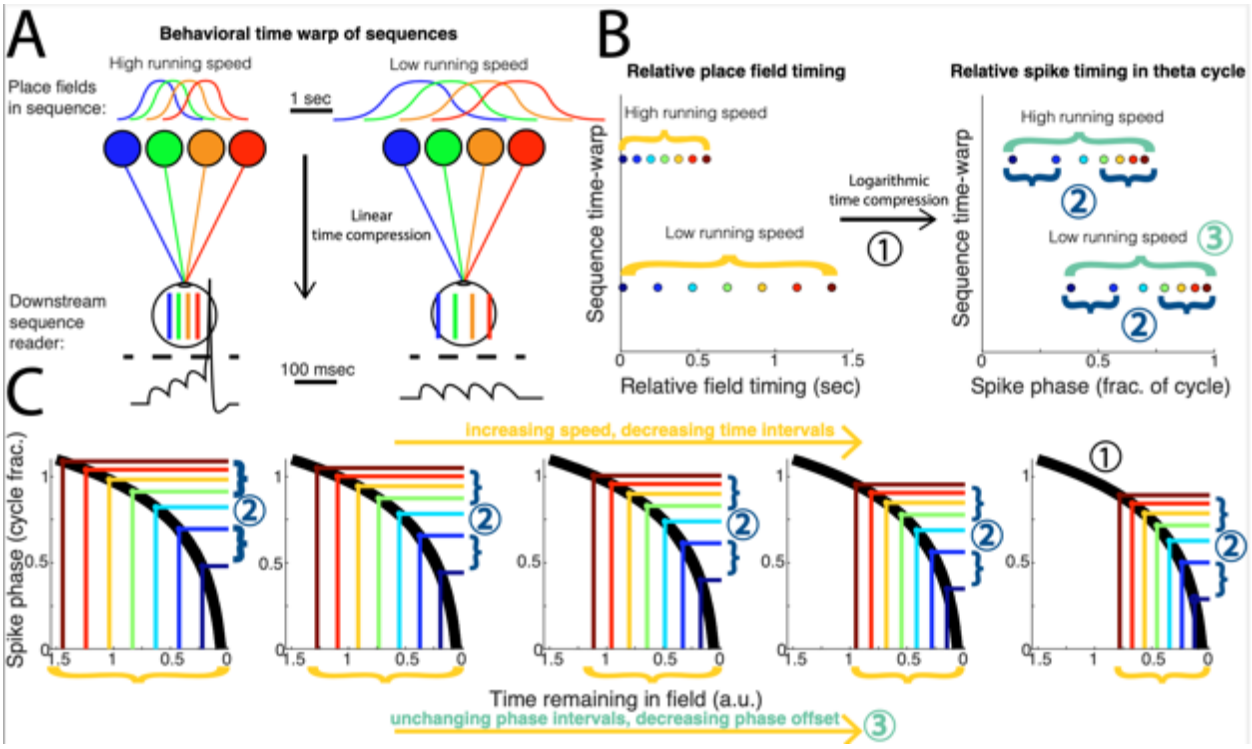

Figure 2-1. The behavioral time-warp problem for recognition of place field sequences can theoretically be solved using the logarithmic theta transform (LTT).

A) Example illustration of 4 spatiotemporally overlapping place fields (color-coded bell-shaped curves) plotted in time at high running speed (left column) and at low running speed (right column). According to the theta phase coding model in which time is compressed linearly into sequences on the theta cycle timescale, readout using a delay line system and temporal summation of place cell outputs would fail with different running speeds (bottom).

B) *Proposed implementation of time-warp invariant sequence coding using logarithmic time compression.* The effects of a logarithmic transformation of time for a sequence of 7 consecutive place field centers, occurring in the color-coded temporal order of (red, orange, yellow, green, blue, indigo, violet) at high running speed (upper) and at low running speed (lower). While they occur over ~0.7 sec (high speed) and ~1.4 sec (low speed) in behavioral time (left), they become time-compressed into a theta cycle lasting 0.1 sec (right) via phase precession and are mapped to the same temporal pattern only if the transformation is logarithmic.

C) *Schematic of theta-phase coded logarithmic transformation of time via phase precession.* Precession plotted as a function mapping inputs in behavioral time (x-axis) to outputs in time within a theta cycle (y-axis). Behavioral time axis is reversed here to maintain negative slope of standard phase precession plots for comparison to standard model without affecting overall shape or transformation effect. This is shown for the same sequence as in *(B)* at low (left) to high (right) running speeds.

*Colored numbers 1,2,3 in panels **B** and **C**:* Predictions of LTT tested in real place cell data in the remaining figures. *Prediction 1:* Theta phase has logarithmic relationship with time in place fields. *Prediction 2:* Theta sequences display a logarithmic spike timing difference gradient, decreasing in phase increment from early to late within theta cycles. *Prediction 3:* When running speed increases, theta sequences display no change in phase separation, increase in phase-time compression ratio, and decrease in mean phase.

The “characteristic banana shape” (McClain et al., 2019; Souza & Tort, 2017) of phase precession manifests as its progressively increasing steepness across a field (Figure 1C, Figure 2A). When the phase of spikes within theta cycles is visualized in relation to the rat’s concurrent position, the pattern of an initially shallow relationship between phase and distance that gradually increases in slope is evident across fields (Figure 2A). This ubiquitous curvature has not been given a mathematical significance or structure, which itself can lead to powerful implications through the rich theoretical background that is already established for such structures. If the shape of phase precession transforms time into the logarithm of time to produce time-warp invariant sequences in hippocampal activity, at least 3 falsifiable predictions can be made (Figure 1B,C): 1) theta phase has a logarithmic relationship with time in place fields; 2) sequence spacing within individual theta cycles is not uniform, and 3) when running speed increases, theta sequence patterns remain identical, but shift coherently to earlier theta phases. To test the LTT theory, we next assessed each of these predictions in hippocampal place cell datasets recorded from multiple rats during spatial navigation.

Prediction 1: Theta phase is sensitive to the logarithm of remaining time in field

We first sought to show whether a logarithmic formulation of the shape of phase precession with respect to time is also consistent with the data from place cells in navigating rats (Figure 2). In testing this, we first note that the traditional interpretation of phase precession as coding for distance within a place field (Geisler et al., 2007; Huxter et al., 2003), does not rule out an additional relationship with time since these studies do not control for potentially confounding variations in elapsed time that always

accompany changes in distance. An example session showing multiple place fields on a linear track is shown in Figure 2A. Theta oscillations in the local field potential are concurrently observed with place cell firing and these oscillations precisely modulate place cell spike timing: spikes shift to progressively earlier (lower) phases within theta cycles (phase precession). This phase precession follows a progressively steepening, non-linear, curved shape (often referred to as a “banana” shape) as a rat moves across each field (Figure 2A).

To understand how theta phase precession is controlled by distance versus time, it is illustrative to examine single lap place field traversals at different running speeds, allowing for empirical disambiguation between distance and time coding (Figure 2B). In particular, during a lap traversed at a low speed, phase-distance coding predicts that theta phase shows no change in slope with respect to distance but approaches zero (horizontal) slope with time. In contrast, phase-time coding predicts phase approaching infinite (vertical) slope with distance during a slow lap with no change in slope with respect to time (Figure 2B). Data from a place cell across traversals at low and high speeds are shown in Figure 2C (see also examples in Supplementary Figure 2). The changes in phase slope with respect to each behavioral variable are consistent with the existence of time-sensitivity in phase precession as predicted by LTT, alongside the well-established distance coding. This was verified on a population level amongst fields with at least 20% variation of speed across traversals relative to the typical speed, showing a significant increase in the slope of phase with respect to time in the top 10 percentile of speed traversals relative to the bottom 10 percentile (Figure 2D; Wilcoxon

signed rank p=1.575e-47), as well as a significant decrease in the slope of phase with respect to distance in the same (Figure 2D; Wilcoxon signed rank p=6.090e-17). These changes in slope with speed could not be explained by changes in correlation, as the pairwise difference between phase-time correlation ratio between speed categories and phase-distance correlation between speed categories for each field was not significantly different from 0 (Figure 2D; Wilcoxon signed rank p=0.36). Furthermore, 69% (490) of the 701 fields showed some decrease in distance-phase slope across speed categories (Figure 2D), consistent with time-coding existing to some extent in the majority of place cells studied here. Consistent with previous work on multiplexed distance and time coding in the hippocampal formation (Kraus et al., 2013, 2015), 530 (76%) of fields showed an increase time-phase slope from the low to high speed category indicative of with distance coding, and 335 (48%) of fields showed both signatures suggesting mixed distance and time coding. Indicating that essentially all place cells studied here track some form of progression in space and time, only 15 fields (2%) showed neither of these speed-slope signatures of distance or time coding (Figure 2D).

To more comprehensively disentangle the effects of distance and time on theta phase, we computed a “phase precession surface” with respect to both distance and time (Figure 2E). This clearly revealed that phase changes as a function of remaining time in addition to the expected changes with distance. Importantly, a fair comparison between distance and theta-cycle discretized time requires similarly discretizing the distance corresponding to each spike as the average distance within the relevant theta cycle as done here (see Methods) to avoid unequal contributions of within-cycle phase rolling to

phase correlation coefficients (Sloin et al., 2022). Conditional phase precession curves as population averages (Figure 2E; Supplementary Figure 3AB) also show that the phase precession can be controlled by time remaining in field, rather than only by distance (Figure 2E, Wilcoxon rank-sum test on best fit slope within surface, rank-sum=78, $p=4.883x10^{-4}$***). Finally, the strong relationship between phase and time remaining in field when restricting analysis to spikes occurring at a single distance is also seen robustly on an individual field level (Supplementary Figure 3; Wilcoxon signed rank test on phase-remaining time R given remaining distance, p=1.16e-126). Given this observation of phase-time coding in place cells in addition to distance-time coding, we next sought to more quantitatively characterize this phase-time and phase-distance relationships and their consistency with the aforementioned predictions of LTT.

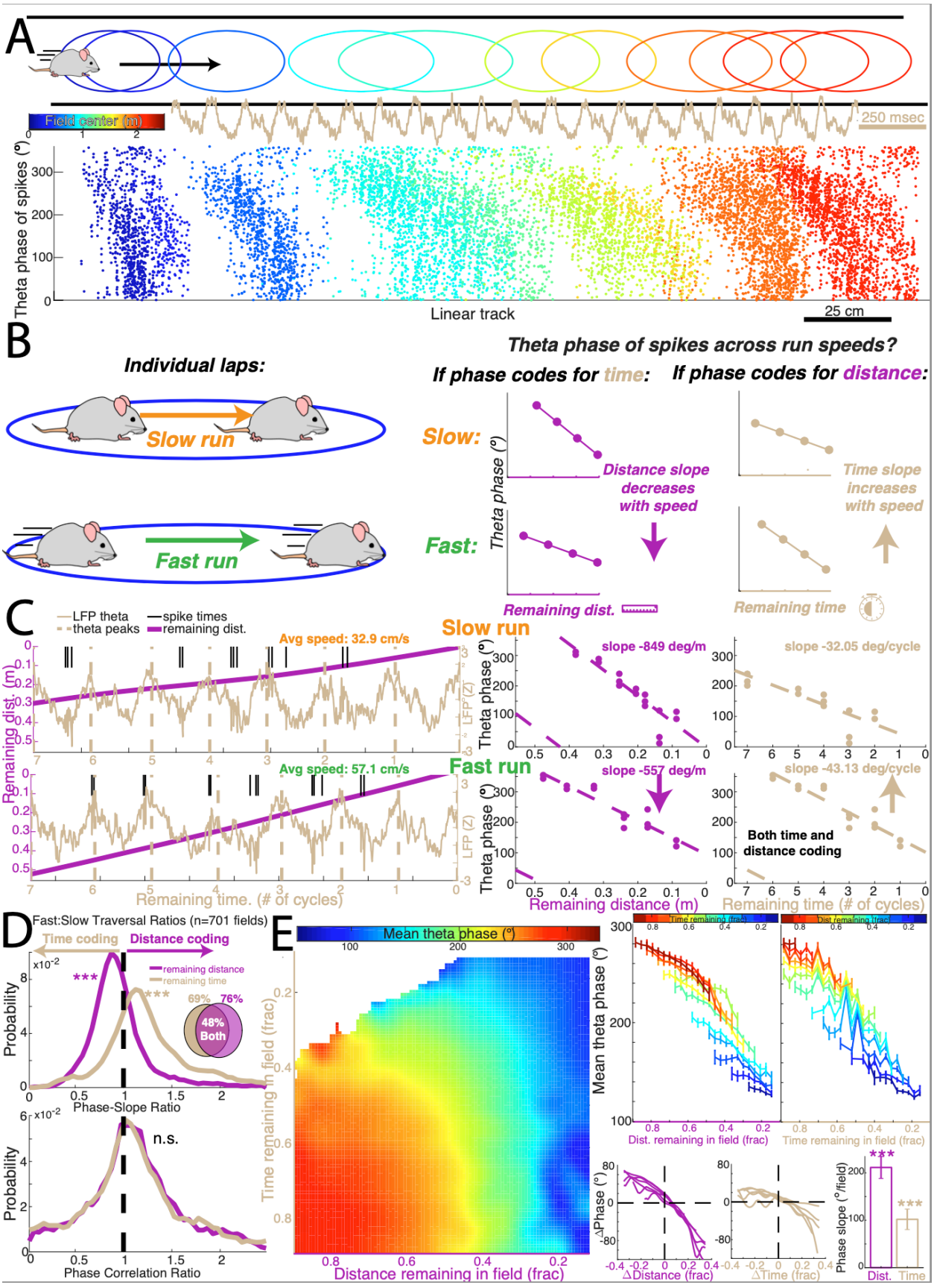
A
Field center (m)
250 msec
Theta phase of spikes (°)
Linear track
25 cm
B
Individual laps:
Slow run
Fast run
Theta phase of spikes across run speeds?
If phase codes for time:
If phase codes for distance:
Slow:
Fast:
Theta phase (°)
Distance slope decreases with speed
Time slope increases with speed
Remaining dist.
Remaining time
C
LFP theta
theta peaks
spike times
remaining dist.
Avg speed: 32.9 cm/s
Avg speed: 57.1 cm/s
Remaining dist. (m)
LFP (Z)
Remaining time. (# of cycles)
Slow run
Fast run
slope -849 deg/m
slope -557 deg/m
slope -32.05 deg/cycle
slope -43.13 deg/cycle
Both time and distance coding
Remaining distance (m)
Remaining time (# of cycles)
D
Fast:Slow Traversal Ratios (n=701 fields)
Time coding
Distance coding
remaining distance
remaining time
***
69%
76%
48% Both
Probability
Phase-Slope Ratio
n.s.
Phase Correlation Ratio
E
Mean theta phase (°)
Time remaining in field (frac)
Distance remaining in field (frac)
Mean theta phase (°)
Dist. remaining in field (frac)
Time remaining in field (frac)
ΔPhase (°)
ΔDistance (frac)
ΔTime (frac)
Phase slope (°/field)
Dist.
Time

Figure 2-2. Testing logarithmic theta transform (LTT) prediction 1: Theta phase is sensitive to remaining time in place fields in addition to remaining distance in field.

A) Example session depicting location of place fields formed along one direction of movement in linear track across several laps. Concurrent with place cell firing are oscillations in the local field potential (example raw trace shown in beige).
B) Illustration depicting how a change in speed across laps can empirically signify distance and/or time coding during movement.
C) Raw data from one example field during a lap with slow running (upper row) or fast running (lower row) but with the same remaining time (7 theta cycles) to the end of the field. Simultaneously shown are position (purple), theta oscillations (beige), and spike times (black) across time over the single traversal. Right panels corresponding to slow running lap (upper) and fast running lap (lower) show the theta phase of spikes plotted against remaining distance and remaining time, showing signatures of both distance and time coding.
D) Population level analysis of speed-based signatures of time coding and distance coding amongst 701 fields showing sufficient speed variation. Upper plot shows the ratio of the phase slope with respect to each variable obtained from the top 10% fastest traversals relative to that for the bottom 10% average speed traversals. Highlights both a speed-related increase in slope with time (distance-phase coding) and a speed-related decrease in slope with distance (time-phase coding, which cannot be explained by changes in correlation (bottom plot). Venn diagram shows the percentage of each class of outcomes resulting from this analysis, with fields showing a smaller magnitude slope with distance in the high speed category classified as time coding, those with a larger magnitude slope with time in the high speed classified as distance coding, and those with both classified as mixed time and distance coding.
E) On the left, circular mean theta phase was computed as a 2D function of remaining distance and remaining time coordinate pairs across 1226 place fields. Distance-time bins with less than 100 spikes across all fields are shown as blank. Only spikes where the rat displayed a speed of at least 5 cm/s were included for analysis. (*upper right*) Conditional relationship between phase and distance while controlling for time, and vice versa, obtained for 12 equal-width, constant-time bins whose centers are represented from 0 to 1 as cold to hot colors for bins with at least 50 spikes (n=1163 place fields). Highlights the dependence of phase on remaining time despite controlling for distance. (*lower left*) Each conditional phase precession curve with mean phase and mean x-coordinate in field subtracted out for emphasis on relative changes in each variable. (*lower right*) The conditional phase gain of distance and time are computed as the slope of the least-squares linear fit to each curve.

A logarithmic theta transform predicts that phase precession would take this logarithmic shape when theta phase is plotted against not just distance, but also against remaining time in a place field (Figure 3A-C), with an initially shallow slope that increases towards a steeper slope with time. This is confirmed in quantitative analysis of a large population of place cells from multiple rats. A quantitatively accessible yet defining criterion for achieving a logarithmic shape is that the temporal slope at any point on the curve should be proportional to the inverse of time at that point (Figure 3D-F; Methods Equation 1). In contrast, a linear form of phase precession, the average case predicted from the standard linear spatial phase precession model (Burgess, 2008; Jaramillo & Kempter, 2017) would predict a flat, independent relationship between time remaining in field and the slope of the relationship between theta phase and time (Figure 3D-F). Plotting the slope of the relationship between theta phase and remaining time across each field unambiguously supports a relationship between these two variables, arguing against a linear phase-time relationship (Figure 3H). In addition, this relationship can be well approximated by linear regression on inverse phase gain vs remaining time in field on the population level and in individual place fields, with the vast majority showing large correlation coefficients of typical value significantly less than 0 (Figure 3IJ; R=-0.50±0.02 [mean ± sem], signed rank z = -14.17, $p=1.475x10^{-45}$***). Furthermore, linear fit slopes cluster around a representative value corresponding to a base of 1.4 (Figure 3J; Supplementary Figure 6). Having identified the typical logarithm base and its variability across many place fields, we were then able to directly assess the relative error of logarithmic versus linear fits for each field (Figure 3K; less error in logarithmic fit; Wilcoxon signed rank p=1.4996e-27; 319 of 399 fields [80%]). Analyzing this error as

a function of remaining time within field also showed systematic bias in the circular-linear regression fit, starting with overestimation, then underestimation, then overestimation again (Figure 3L), a pattern which was eliminated when using a logarithmic model (Figure 3M). Very similar results were obtained when performing these same analyses with respect to remaining distance in a place field, with the same best fit base of 1.4 with respect to distance (Supplementary Figure 4). A logarithmic distance transformation can support a similar function as a logarithmic time transform in creating stable spike time patterns invariant to, rather than speed-related time-warp, cognition-related space-warp manifesting as differing theta sequence trajectory lengths depending on navigational goals independent of running speed (Gupta et al., 2012; Wikenheiser & Redish, 2015a). We illustrate how such logarithmic distance compression can be useful for this function in Supplementary Figure 5. Thus, these results are consistent with a quantitatively characteristic, logarithmic curvature in the phase-time coding and phase-distance coding exhibited by place cells.

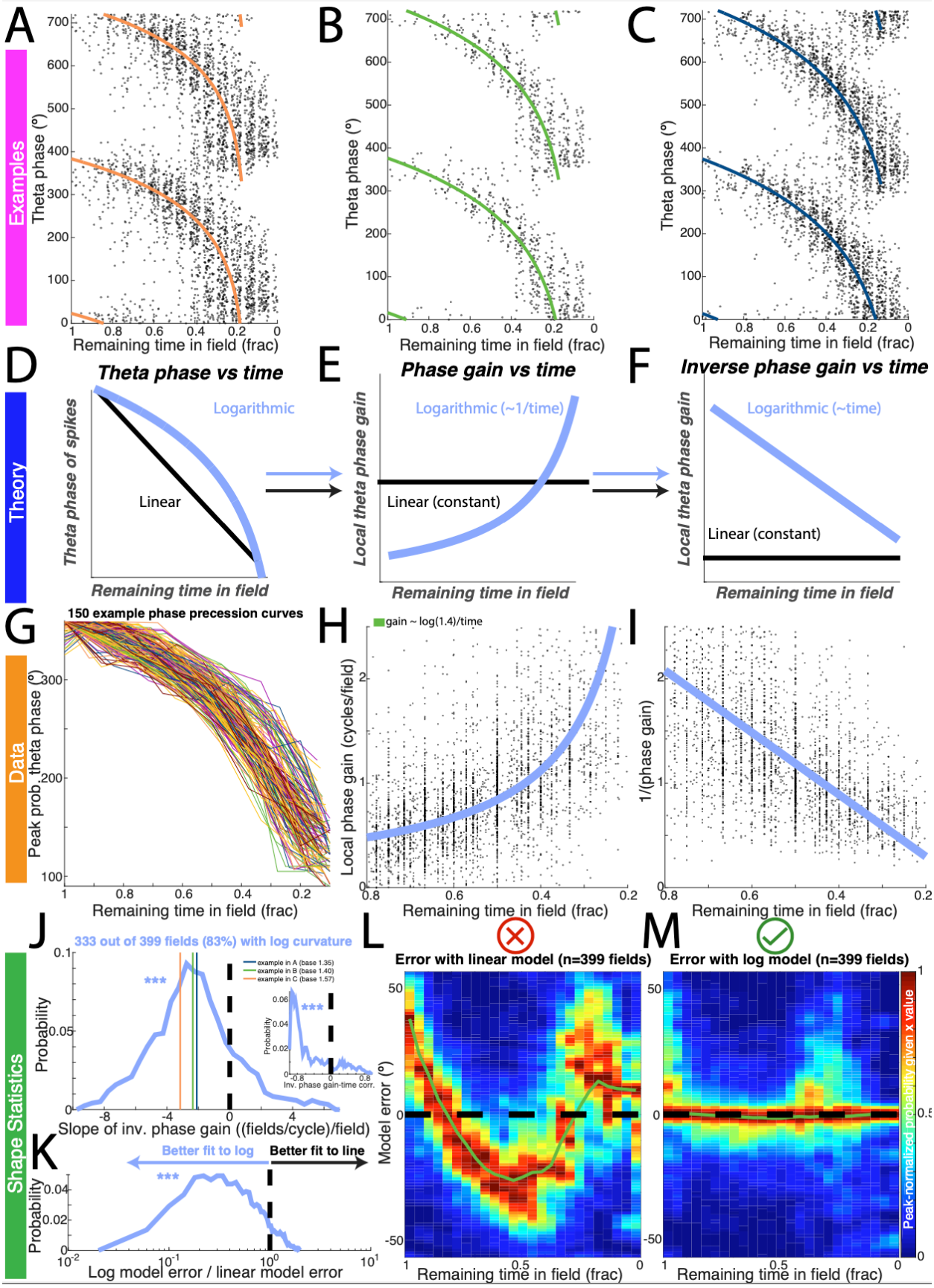
A
B
C
Examples
Theta phase (°)
Remaining time in field (frac)
D
E
F
Theory
Theta phase vs time
Phase gain vs time
Inverse phase gain vs time
Theta phase of spikes
Local theta phase gain
Logarithmic
Linear
Logarithmic (~1/time)
Linear (constant)
Logarithmic (~time)
Remaining time in field
G
H
I
Data
150 example phase precession curves
Peak prob. theta phase (°)
gain ~ log(1.4)/time
Local phase gain (cycles/field)
1/(phase gain)
J
K
L
M
Shape Statistics
333 out of 399 fields (83%) with log curvature
example in A (base 1.35)
example in B (base 1.40)
example in C (base 1.57)
Probability
Slope of inv. phase gain ((fields/cycle)/field)
Inv. phase gain-time corr.
Better fit to log
Better fit to line
Log model error / linear model error
Error with linear model (n=399 fields)
Error with log model (n=399 fields)
Model error (°)
Peak-normalized probability given x value

Figure 2-3. Testing logarithmic theta transform (LTT) prediction 1 (continued): Theta phase has logarithmic relationship with time remaining in place fields with quantitative specificity.

The following analysis is for all spikes from place fields with at least 100 spikes across all laps and at least 5 cycles in the central 60% of the field to estimate curvature (n=399 fields).

A) Raw data from an individual example field showing the theta phase of each spike against time remaining in field, with logarithmic fit in orange (see panel J)
B) Raw data from an individual example field showing the theta phase of each spike against time remaining in field, with logarithmic fit in green (see panel J)
C) Raw data from an individual example field showing the theta phase of each spike against time remaining in field, with logarithmic fit in purple (see panel J)
D) Schematic comparing predictions of LTT (*blue*) and linear time compression (*black*) for the evolution of theta phase over remaining time in field.
E) Schematic comparing predictions of LTT (*blue*) and linear time compression (*black*) for the evolution of theta phase gain over remaining time in field.
F) Schematic comparing predictions of LTT (*blue*) and linear time compression (*black*) for the evolution of the multiplicative inverse of phase gain over remaining time in field.
G) 150 example phase precession curves with base higher than 1.3 (see panel J), each of one random color, showing peak probability theta phase corresponding to each remaining time in field
H) Local phase gain for each place field at each remaining time in field (*black dots*), and a curve showing k/(time to end of field) (*blue dashed line*) for k=log(1.4).
I) Multiplicative inverse of local phase gain for each place field at each remaining time in field (*black dots*), and a curve showing (time to end of field)/k for k=log(1.4) (*blue dashed line*).
J) Probability distribution of estimated k from linear fits of local phase gain vs remaining time in field for each place field. *Inset:* Probability distribution of correlation coefficient of local phase gain vs remaining time in field for each place field showing significant linearity of the relationship (***, Wilcoxon signed rank test, z=-20.81, p=3.775e-96). The peak slope corresponds to a peak probability logarithm base of 1.4.
K) Probability distribution of the ratio of absolute median error using a logarithmic model relative to that using circular-linear regression.
L) Probability distribution of angular error of a linear phase-time at each remaining time in field, showing systematic bias depending on remaining time in field.
M) Probability distribution of angular error of logarithmic phase-time model at each remaining time in field, showing elimination of systematic bias depending on remaining time in field.

Prediction 2: Theta sequences show non-uniform spacing within single cycles

Coding for the logarithm of time or distance in individual place cells does not guarantee that spike coordination amongst place cells also respects this relationship. This is because additional coordination beyond independent phase precession in overlapping cells is known to occur in the formation of theta sequences (Feng et al., 2015; Foster & Wilson, 2007). If the time-warp invariance conferred by logarithmic coding in single cells precessing through their fields is to be useful in a spatial sequence code, it must be inherited by the code for sequences of overlapping fields across cells within individual theta cycles. Therefore, we next looked for evidence of the preservation of logarithmic time within the separation of spike phases of overlapping fields in individual cycles. LTT predicts that spacing between spikes coding for consecutive place fields should be expanded at early theta phases and contracted at late theta phases, while a linear relationship with time would predict no such change (Figure 4A). An example session illustrating the analysis including 13 such place cell pairs is shown in Figure 4B, with all pairs showing a contraction in timing difference from early to late phase. Quantifying this expansion across all sessions including 377 sufficiently overlapping field pairs (see Methods) yielded a significant average pairwise contraction from early to late theta cycle (Figure 4C), paired observation signed rank test, $z = 8.314$, $p = 9.270 \times 10^{-17}$***). Thus, coordination of place cell spikes within theta cycles preserves a nonlinear phase code, consistent with theta sequences respecting the LTT of the field sequences they represent.

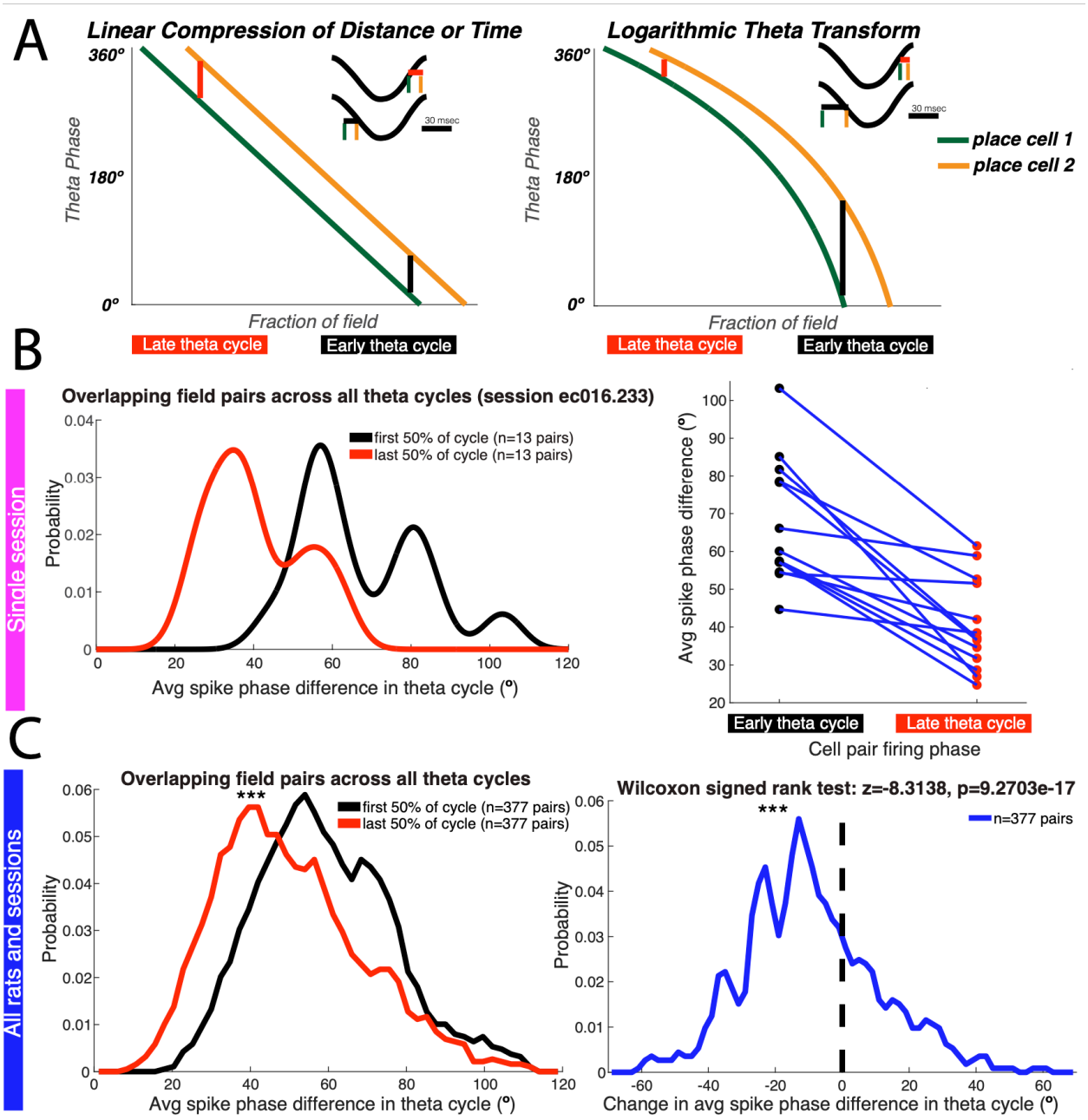

Figure 2-4. Testing logarithmic theta transform (LTT) prediction 2: Theta sequences display a logarithmic spike timing difference gradient, decreasing in phase separation from early to late within theta cycles.

A) Schematic showing how LTT in theta sequences predicts larger inter-cell spike intervals when they both occur late in a theta cycle than when they occur early in a theta cycle, while linear time or distance compression predicts no difference.

B) Example session including 13 overlapping place field pairs whose centers are no more half a field apart, and overall leftward shift in the distribution of spike phase difference (*left*). When examining these pairwise, all pairs show an increase in theta phase difference (blue) from early (black) to late (red) theta phase (*right*).
C) Distribution of the change in spike timing difference between all place field pairs (n=377 pairs) as they occur in early (black) vs late (red) theta phases, showing a population wide decrease in spike time difference moving to later phases (signed rank $z = -8.314$, $p = 9.270 \times 10^{-17}$***) as predicted by LTT in theta sequences.

Prediction 3: Time-warp (speed change) leads to selective phase shift in theta sequences without corresponding change in phase separation

As running speed corresponds to behavioral time warp for spatial field sequences, LTT has unique predictions for the relationship between behavioral field sequences and theta phase sequences at different speeds. If our proposed theory is accurate, speed increases should be transformed into uniform phase shifts in the theta phase code (see Figure 1B) for the following reasons. Running at different speeds causes the behavioral time intervals between place fields to stretch or shrink in time (Figure 5A). Different models for how space and time are encoded by theta phase then manifest different speed-phase signatures in response to this changing behavioral time interval (Figure 5B-D; see Methods Equations 2-4). These signatures can be recognized by quantifying phase separation, phase-time compression ratio, and mean phase at different running speeds. In particular, distance coding of any kind, particularly of linear compression or a logarithmic transformation, predicts no phase shift with running speed, as distance within field at any given position does not vary with speed. In contrast, time remaining in field at any given position is speed-dependent such that linear time compression predicts phase separation changes in proportion to speed, while a logarithmic time transformation predicts changes only in theta sequence phase offset.

In order to distinguish between these models being at work in hippocampal cells, we assessed the relationship between these theta sequence properties and running speed while controlling for position (see Methods) in place cell data. Examples of field sequences and the theta sequences representing them shows a mean phase shift towards earlier phases with increasing running speed without comparable change in phase separation (Figure 5E-G), consistent only with LTT (Figure 5D). To evaluate this effect statistically on the population level, data across all 831 distinct place field sequences represented by a total of 6680 theta sequences across laps were analyzed with respect to running speed (Figure 5H; see Methods). This showed no significant relationship between speed and phase separation (Figure 5H left; circular-linear regression; rho=0.07, p=0.82), a significant positive relationship between speed and phase-time compression ratio (Figure 5H middle; linear-linear regression; Pearson's correlation R=0.86, $p=3.90 \times 10^{-4}$***), and a significant negative relationship between speed and mean phase (Figure 5H right; circular-linear regression; rho=-0.79, p=0.00234**). These speed-phase signature results were again only consistent with the LTT theory (Figure 5D).

We next evaluated whether the predicted relationships between speed and theta sequence properties were present not only when combining data across field sequences but also on an individual sequence level, given that these are not necessarily consistent with each other (Parra-Barrero et al., 2021). Each field sequence showing sufficient speed variation across laps and its average theta sequence property

in low- and high-speed traversals are visualized as an individual point in a two-dimensional space to easily compare its value across the two speed categories (Figure 5I). In this space, average theta sequence phase separation occurs approximately equally above and below the x=y line amongst individual sequences, suggesting no systematic change in phase separation with increasing speed. In contrast, the point cloud representing theta sequence phase-time ratio presents systematically above the x=y line, and the point cloud of mean phases lies primarily below this line, supporting a widespread increase in phase-time ratio and widespread decrease in mean phase amongst field sequences. Quantitative analysis again showed no significant relationship between phase separation and speed (Figure 5I; bootstrap reshuffling test, p=0.4173), a significant positive relationship between phase-time compression and speed (Figure 5I; bootstrap reshuffling test, $p=1.622 \times 10^{-5}$***), and a significant negative relationship between mean phase and speed (Figure 5I; bootstrap reshuffling test, p=0.0091**). Variation in mean distance with running speed (bootstrap reshuffling test, p=0.4040) or in distance separation with running speed (bootstrap reshuffling test, p=0.4915) are effectively the same between these groups and could not explain the results (Supplementary Figure 8AB). Overall, this result of theta sequence property changes with speed variation is not consistent with linear distance compression or linear time compression, but is precisely what is predicted only by the LTT framework (Figure 5J).

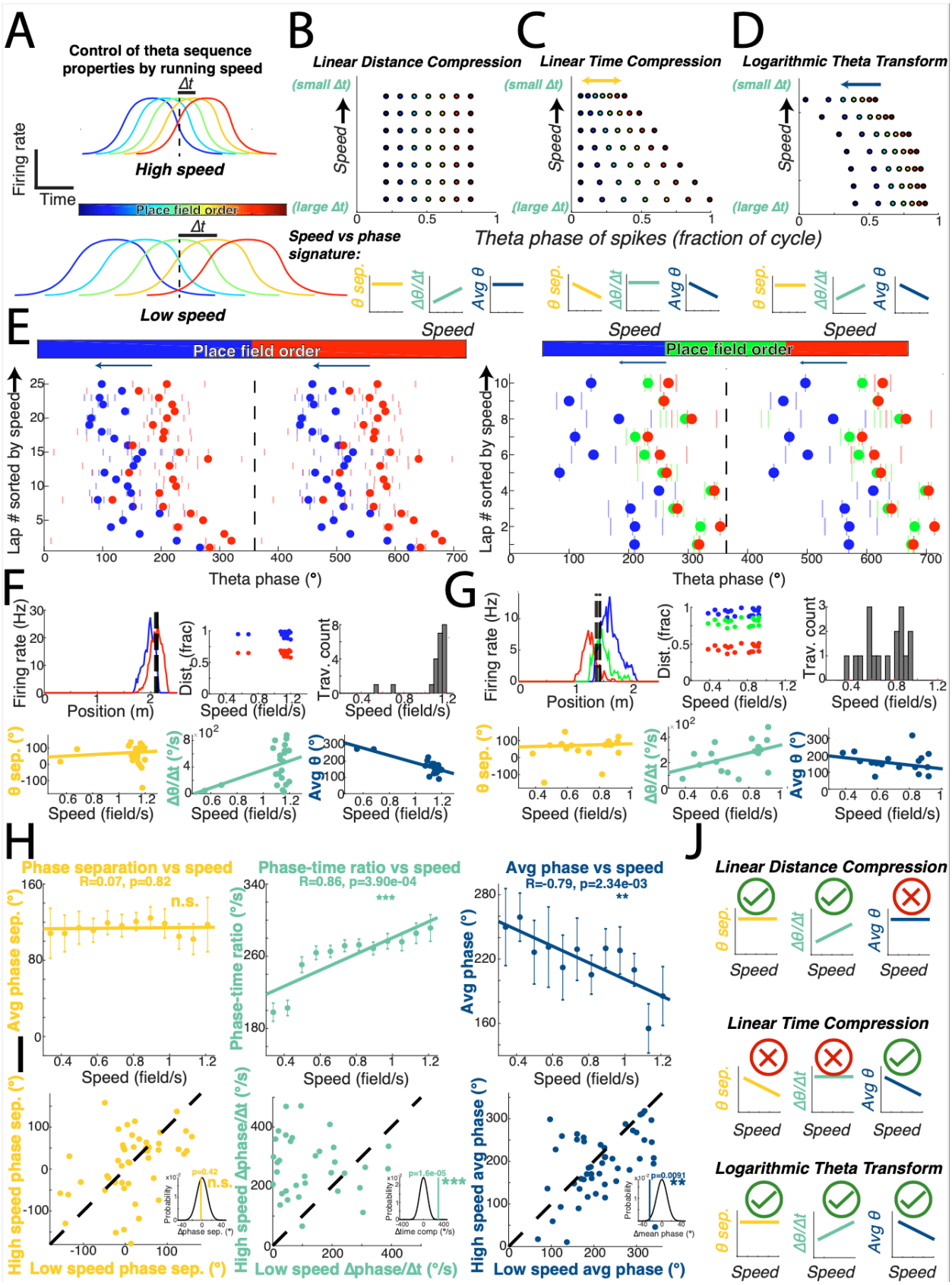
A
Control of theta sequence properties by running speed
Δt
Firing rate
Time
High speed
Place field order
Δt
Low speed
B
Linear Distance Compression
C
Linear Time Compression
D
Logarithmic Theta Transform
(small Δt)
(large Δt)
Speed
Theta phase of spikes (fraction of cycle)
Speed vs phase signature:
θ sep.
Δθ/Δt
Avg θ
E
Speed
Place field order
Lap # sorted by speed
Theta phase (°)
F
G
Firing rate (Hz)
Position (m)
Dist. (frac)
Trav. count
Speed (field/s)
θ sep. (°)
Δθ/Δt (°/s)
Avg θ (°)
H
Phase separation vs speed
R=0.07, p=0.82
n.s.
Phase-time ratio vs speed
R=0.86, p=3.90e-04
***
Avg phase vs speed
R=-0.79, p=2.34e-03
**
Avg phase sep. (°)
Phase-time ratio (°/s)
Avg phase (°)
I
High speed phase sep. (°)
Low speed phase sep. (°)
p=0.42
n.s.
High speed Δphase/Δt (°/s)
Low speed Δphase/Δt (°/s)
p=1.6e-05
***
High speed avg phase (°)
Low speed avg phase (°)
p=0.0091
**
Probability
J
Linear Distance Compression
Linear Time Compression
Logarithmic Theta Transform

Figure 2-5. Testing logarithmic theta transform (LTT) prediction 3: When running speed increases, theta sequences display no change in phase separation, increase in phase-time compression ratio, and decrease in mean phase.

A) Schematic illustrating a sequence of 4 place fields at low running speed and high running speeds, with order of visitation encoded in cool to warm colors.
B) Summary of predictions of the linear distance compression models for theta sequence properties in relation to running speed,(see also Methods Equation 2).
C) Summary of predictions of the linear time compression theta sequence properties in relation to running speed (see also Methods Equation 3).
D) Summary of predictions of LTT model for theta sequence properties in relation to running speed, (see also Methods Equation 4).
E) Example field sequences with place fields shown in color by order of visitation, from cool to warm colors. The theta sequences representing this field sequence in each lap is shown as a raster of all spikes from both fields, with each lap representing a row, sorted by increasing running speed from bottom to top. The mean phase of spikes for a traversal in a given lap is represented by a color-coded dot. A repetition of each theta cycle is displayed to show the circular nature of this data.
F) Example field sequence with place fields shown in color by order of visitation, from cool to warm colors. Dashed lines indicate the positions at which theta sequences were sampled. Distance within field as a fraction of the field width is shown with respect to running speed. The distribution of average running speeds within the field sequence is also shown across laps. A scatter plot of theta sequence properties against running speed with linear fits represents the speed-phase signature for this field sequence.
G) Example field sequence analogous to panel (F) with 3 participating cells.
H) The mean value of each property from 831 distinct place field sequences represented by a total of 6680 theta sequences with respect to speed. Error bars represent upper and lower limits of the circular mean computed by a one-sample test for mean angle, or ± standard error of the mean in the case of phase-time compression ratio. Circular-linear regression or linear-linear regression was used to statistically evaluate the relationship between the running speed and the population level theta sequence properties, respectively (n.s. = not significant, indicating $p>0.05$; *** indicates $p<0.001$; ** indicates $p<0.01$).
I) Field sequences with sufficient speed variation across laps were collected (n=49 different field sequences). Each field sequence is represented as a dot in the space relating its mean value in the low-speed group (x-coordinate) with its mean value in the high-speed group (y-coordinate) relative to the x=y line (dashed line). The mean difference of these properties between speed groups (inset, vertical line) being different from 0 was evaluated with bootstrap label reshuffling (black distribution).
J) Summary schematic illustrating which theta sequence property changes with speed variation in place field data are consistent with each phase coding model (green check = correct prediction, red “x” = incorrect prediction).

Given that novelty has been shown to bias the phase of spikes towards the peak of theta cycles through an acetylcholine-dependent mechanism (Douchamps et al., 2013), we note that the vast majority of sessions analyzed here were from linear tracks to which each rat was already familiar, with 75 out of 80 sessions being on the 10^{th} or greater performance of the task, 4 sessions in which the task had been performed at least 7 times, and only 1 session which constituted a novel exposure. Thus, changes in theta phase offset with running speed cannot be attributed to confounding changes in novelty. Another important consideration is the extent to which realistic accelerations and decelerations can break the assumptions about speed in the LTT framework. These assumptions include that the theta phase of place cell spikes preferentially follows time remaining regardless of speed changes within a spatial sequence to support a consistent time transform, which we verified here (Supplementary Figure 9A).

In particular, the relationships between theta phase, remaining time, and remaining distance were analyzed in the same way as in Figure 2, but now restricted only to traversals characterized by deceleration (-80 cm/s^2 to -10 cm/s^2), a constant speed (-5 cm/s^2 to 5 cm/s^2), or acceleration (10 cm/s^2 to 80 cm/s^2). The significant distance-conditional relationship between phase and remaining time persisted in all 3 conditions (Supplementary Figure 9A; Wilcoxon signed rank tests; deceleration: signed rank= 91, p=2.441e-4, constant speed: signed rank= 91, p=2.441e-4, acceleration: signed rank= 90, p=4.883e-4). However, time coding was particularly prominent in accelerating conditions, and distance coding more prominent in decelerating conditions (Supplementary Figure 9A), potentially forming a behavioral division between the

operation of the logarithmic time transform and the logarithmic distance transform that make up LTT.

Another assumption is that a linear time warp factor constitutes a good approximation of most presentations of a spatial sequence to hippocampal circuits, enough to be of practical use during realistic behavior. We test this in the present dataset by feeding in all field traversals of varying amounts of speed and acceleration/deceleration into an LTT simulation converting a field sequence into a theta sequence (Supplementary Figure 9BC). Results show that moving from the extremes of 80cm/s^2 to -80 cm/s^2 corresponds to increasing phase separation and decreasing phase offset both by about 30 degrees. This corresponds to about 10 milliseconds or less, an amount contained within even fast gamma cycles that help parse theta sequences, suggesting the speed changes in this dataset do not break the constant speed assumption for coding and decoding purposes. The simulations highlight how speed changes must be evaluated within the relatively small spatial range that determines the LTT, namely the range of ends of partially overlapping fields participating in the sequence. Speed is likely to be relatively constant in this small region for closely overlapping fields given natural limitations on both acceleration and deceleration during this time, including the limits of skeletal muscle force that allows for changing speed up or down. Still, an important future test of LTT will be to reassess its robustness to realistic amounts of field overlap and speed change within field sequences in ethologically relevant environments.

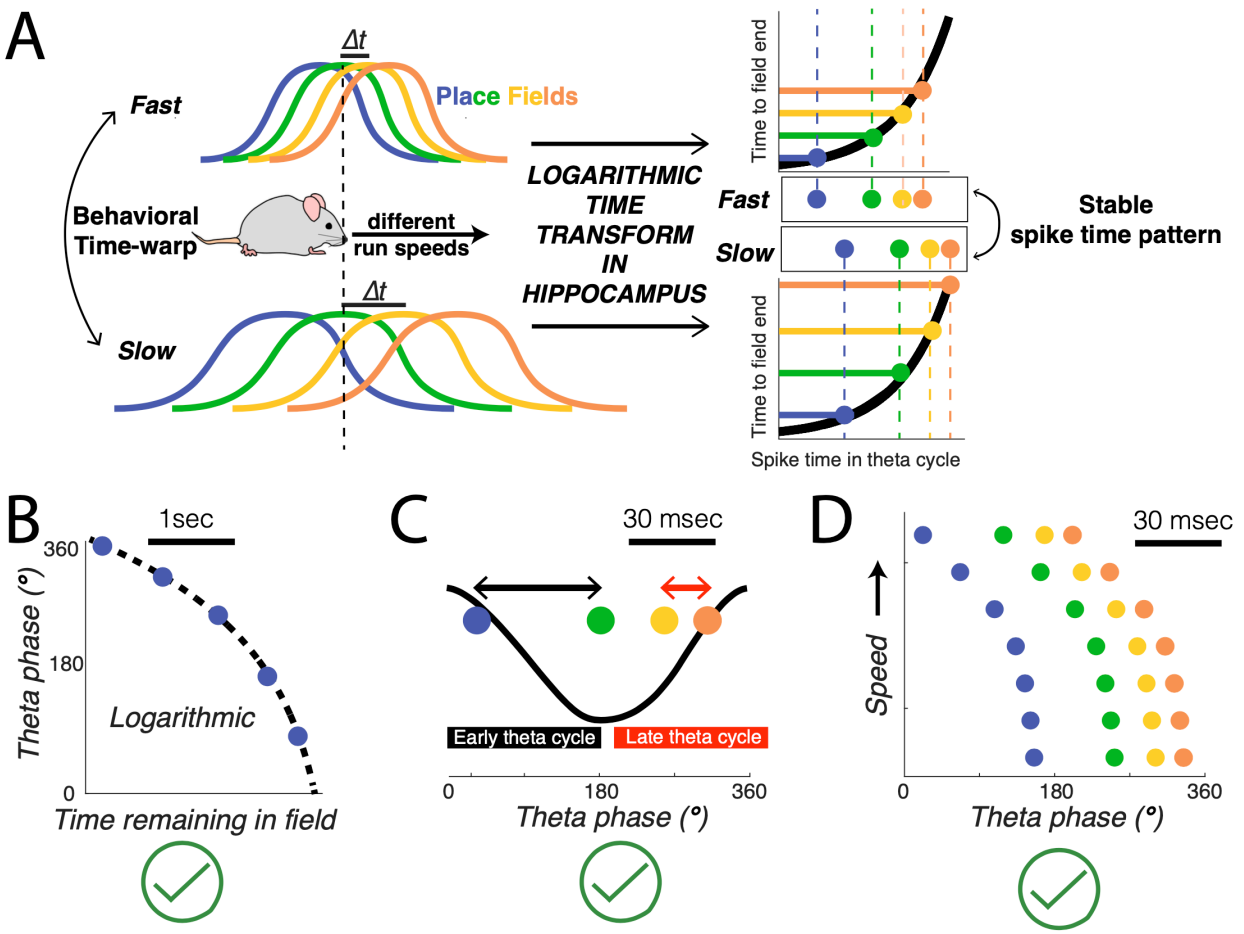

Figure 2-6. Summary of theoretical and empirical support for Logarithmic Theta Transform (LTT) producing speed-invariant code for field sequence in the hippocampus.

A) LTT posits that hippocampal theta phase precession has a nonlinear shape that allows phase to represent the time since field entry on a logarithmic scale (spike time in theta cycle), leading to equivalent downstream post-synaptic coincidence detection across a different running speeds.

B) Predicted Neural Dynamics 1: Theta phase has logarithmic relationship with time in individual place fields with quantitative specificity. Empirical data matches this prediction and shows that the hippocampus uses a temporal scaling factor of 1.4, identical to the spatial scaling governing the spacing between entorhinal grid modules.

C) Predicted Neural Dynamics 2: Theta sequences display a logarithmic spike timing difference gradient, decreasing in phase increment from early to late within theta cycles. Empirical data matches this prediction.

D) Predicted Neural Dynamics 3: As running speed increases, theta sequences display i) no change in phase separation (i.e. the spike timing pattern remains the same), ii) increase in temporal compression ratio (Δphase/Δtime), and iii) decrease in mean phase. Empirical data matches this prediction.

2.4 Discussion

Here we have shown that the theta phase code logarithmically represents time and distance in a place field, enabling the speed-invariant representation of place field sequences within theta cycles (Figure 6). This logarithmic theta transform (LTT) framework parsimoniously organizes known features and predicts novel features of the hippocampal neural code for episodic information, with implications for more general principles of sequence coding in the brain, as explored further below.

Implications for sequence coding

A useful perspective for understanding any given neural activity is to consider not only what behaviorally relevant information is coded by properties of this activity, but also what aspects of the activity can be decoded by downstream neural readers (Buzsáki, 2010; Hopfield, 1995; Johnson, 2000). Applying this reasoning to hippocampal sequence coding, the behaviorally dynamic sequences of place cell activity at different speeds (Maurer et al., 2012; Parra-Barrero et al., 2021) would not be well-decoded by a traditional perceptron-like readout and requires an alternate explanation. This is because synaptic weights conflate the relative pattern and salience of sequence elements, making these networks insensitive to changes in time-order and fragile to changes in time-warp (Hopfield, 1996; Hopfield & Brody, 2001).

In the LTT framework proposed and validated here for hippocampal theta sequences, theta phase coding functions to remove scalar changes in behavioral time using a

logarithmic scale. One of the defining features of space is its invariance to the speed of the observer, so we view this removal of the effect of speed on spike time patterns as an important step in constructing or supporting a spatial code. Through this transformation, a spatial field sequence traversed at a variety of speeds, or contemplated at different spatial scales (Gupta et al., 2012; Wikenheiser & Redish, 2015a), is encoded by an identical theta sequence pattern, allowing for an equivalent decoding of the relative spike time pattern by a post-synaptic neuron. Maintaining a speed-invariant spike time pattern not only facilitates the consistent functioning of downstream temporal summation, but also that of any neural processes that rely on timing such as spike-timing dependent plasticity, synaptic facilitation and depression, and the dynamics of voltage-gated intrinsic conductances. Importantly, this mechanism for mapping variable behavioral time onto stable neural time operates within individual theta cycles and should not be confused with the notion of log-normal distributions of neural firing rates in the brain (Buzsáki & Mizuseki, 2014). The log-normal distribution is the observation of skewed rates and other features across neural populations (Mizuseki & Buzsáki, 2013; Roxin et al., 2011) whereas LTT is a functional framework working at the level of single theta cycles to algorithmically explain how stable spike time patterns emerge in the hippocampus.

Of note, this strategy for achieving time-warp invariant sequence coding requires only a fiducial time representation accessible to all neurons involved, and not necessarily a highly repeatable or periodic one (Hopfield et al., 1998). The phase-based encoding and decoding of field sequences could operate on a cycle-by-cycle basis, such that even if

absolute delays vary slightly in terms of milliseconds across cycles, these changes are shared amongst encoding and decoding neurons to produce an identical response. The preference for theta phase separations rather than absolute time separations could be mechanistically enforced by the phase-specific interneuron class activities (Klausberger & Somogyi, 2008) following theta rhythm rather than absolute time, determining the size of effective windows for temporal summation based on the frequency of the local cycle. The fact that theta cycles can be used to estimate time beyond its approximate period (~120 ms) is independent of its ability to form the time-domain code of phase for timing less than a theta period. Timing can be defined even more generally as relative to widely-available behavioral events such as binaural sound arrival (Carr, 1993), sniffing (Deschênes et al., 2012), or whisking (Bush et al., 2016) events. Indeed, recent findings on hippocampal formation activity in bats during spatial navigation show no theta rhythm but do show spike synchrony and phase coding relative to large LFP fluctuations (Eliav et al., 2018), which as reported seems to retain the concave-down, “banana” shaped curvature that could also follow the logarithmic transformation pattern. This potentially supports the conservation and greater generalizability of this framework beyond hippocampal function to circuits with widely available, but not periodic, timing signals shared amongst neurons.

In addition to this critical function of maintaining stable neural timing, LTT also has several additional information processing advantages, including supporting time-warp invariant pattern compositionality (Tank & Hopfield, 1987). Applied to place field sequences, this means different sequences can be recognized separately and

combined at another step downstream if they have matching time-warp, effectively coding for sequences of sequences to allow spatial cognition involving longer paths than fit within single theta cycles. LTT also allows for separation of the coding of pattern scale and pattern salience, where the former can be coded in logarithmic time shift and the latter coded in synaptic weights and firing rate without mutual interference. Delay-based coding structures show greater tolerance in responding to partial information (Hopfield et al., 1998), another attractive feature for spatial navigation processing, which must integrate many sources of information without over-dependence on any single one, such as optic flow or self-motion estimates (Harvey et al., 2009; Poulter et al., 2018).

The LTT framework further suggests a new way to consider rate and time coding in the hippocampal formation, helping to unify the traditional viewpoints of spatial coding and episodic memory formation involving temporal sequences (Buzsáki & Moser, 2013). This combination can be achieved by assigning the rate-coded fields the function of tracking spatial nodes that can be presented at a range of temporal separations depending on running speed, whose relationships are then encoded into relative spike timings in a time-warp invariant way using LTT. Extending this reasoning, the rate-coded fields need not represent positions, but could represent nodes along any continuous dimension of motor or sensory space, such as sound wave frequency (Aronov et al., 2017), to create stable internal sequences despite external timing variability more generally. LTT in hippocampal circuits can thus serve as a fruitful scaffold to build further understanding of neural strategies for sequence coding.

Implications for the hippocampal neural code

An important parallel question is the physical instantiation of LTT in the hippocampus, which has thus far been considered phenomenologically here for its functional consequences, independent of the mechanisms producing it. Potential neural mechanisms for logarithmic time coding in the hippocampus include the temporal decay of post-synaptic potentials, the time dependence of subthreshold conductances, and short-term synaptic plasticity shaping phase precession, all of which are predicted to involve faster dynamics with each passing theta cycle. A more network-level mechanism is in the dynamic frequency of theta-coupled gamma rhythms that are known to orchestrate pyramidal cell spike times through local inhibitory circuits in the hippocampus (Bieri et al., 2014; Colgin, 2015). The switch from fast gamma to slow gamma could correlate with the logarithmic shape described here by coupling with place cell dynamics at different halves of a place field (Fernández-Ruiz et al., 2017). In particular, if phase precession across theta cycles is discretized by gamma cycles, the precession step-size would be small late in the theta cycle where fast gamma occurs, corresponding to slow phase precession, but large in the early theta cycle where slow gamma occurs with wider cycles and thus faster phase precession. Of note, the direction of theta cycle asymmetry (Belluscio et al., 2012) and the preferred phases of slow gamma and fast gamma (Bieri et al., 2014; Colgin, 2015; L. Zhang et al., 2019) fit well with the dynamics of the corresponding branches of logarithmic phase precession (Figure 3; Supplementary Figure 6). Using theta-coupled gamma rhythms to generate a consistent logarithmic transformation would require that gamma frequencies increase

with running speed in parallel with theta frequency increases with running speed. Indeed, this relationship between gamma frequency and running speed has been observed and is linear on a log-log scale (Ahmed & Mehta, 2012; Zheng et al., 2015), consistent with a logarithmic representation of behavioral time by gamma oscillations within theta cycles. This possible mechanism for LTT would put gamma frequency changes across theta cycles in a new light, not only forming separate information channels (Schomburg et al., 2014; Zheng et al., 2016), but also with the succession of frequencies itself being important to transform time into an internal logarithmic representation of time.

In addition to these constraints on local network dynamics, LTT makes predictions about the downstream neurons that detect theta sequences. The identity of these cells is under investigation, with promising candidates including those in the medial prefrontal cortex (Jones & Wilson, 2005), retrosplenial cortex via the subiculum (Nitzan et al., 2020), and ventral striatum (Meer & Redish, 2011) to allow decision-making, memory consolidation, and reward prediction, respectively, based on spatial sequence information. In this framework, such cells are predicted to possess integration mechanisms that operate on the timescale appropriate for the readout of theta sequences, and recent studies show that active dendritic delay lines are sensitive to sequences on this timescale in cell types throughout the brain (Branco et al., 2010; Ishikawa & Ikegaya, 2020).

Another attractive candidate for theta sequence decoders is the dendrites of place cells themselves, such that upcoming place fields are generated or stabilized through dendritic detection of theta sequences formed by preceding place cells during

navigation. Recent work showing that local CA1 circuits contribute to the spatial selectivity of place fields (Geiller et al., 2022; Zutshi et al., 2021) and that dendritic integration occurs within CA1 circuits during sharp-wave ripple sequence replay (Ishikawa & Ikegaya, 2020), particularly in association with spatial learning in a novel environment (Rolotti et al., 2022), strengthens the plausibility of this prediction. Furthermore, the backwards phase shift of CA3 theta sequences and dendritic depolarization relative to CA1 firing (Dragoi & Buzsáki, 2006; Mizuseki et al., 2009), the functional connectivity of CA3 pyramidal cells with the dendrites of CA1 pyramidal cells (Bittner et al., 2015), and the approximately symmetric bell shape of firing rate within place fields is consistent with the generation of place fields through partial-full-partial detection of sequential activity amongst preceding fields during navigation. This predicts that sequential activation of consecutive dendritic regions in CA1 pyramidal cells would be visible with subcellular calcium imaging during place field generation, similar to that observed during sharp-wave ripples (Ishikawa & Ikegaya, 2020). The preferential response of dendritic detection mechanisms in these decoders to the nonlinearly shaped theta sequences shown here, accelerating in phase from past to future within a theta cycle (Figure 4), is another prediction made by the LTT framework. This could be tested using sequential activation of dendritic regions with controlled spatiotemporal profiles using holographic two-photon optogenetics (Adesnik & Abdeladim, 2021).

As far as the shape of theta sequences themselves, we have shown that spikes from the same pair of fields present at different phase separations, depending on when in the theta cycle the spikes occur as predicted by LTT. The amount of space these phase

separations represent depends on the field width of the considered fields, but the consistent monotonic relationship between theta phase and relative phase separation (Figure 3; Supplementary Figure 7) suggests that the phase-to-place slope within theta sequences increases into the represented future for a given theta cycle. This phase-place resolution for upcoming positions also depends on available landmarks, acceleration, and the navigational planning of the rodent as shown by Gupta et al. (Gupta et al., 2012), but we show it also has a consistent relationship with theta phase itself in this dataset. Reexamining this relationship in tasks with more landmarks, speed variation, and navigational choices similar to those in Gupta et al. (Gupta et al., 2012) would help reveal how much LTT can shape theta sequences in the context of these changing navigational variables.

Our results lastly point toward the importance of a quantitative temporal scale factor of approximately 1.4, matching the spatial scale factor governing grid module spacing changes (Barry et al., 2007; Stensola et al., 2012). Theoretical studies of entorhinal function investigating the reason for this constant grid module ratio point toward a maximum efficiency “base-b” representation of space using noisy neurons to be in the range 1.4-1.7 (Wei et al., 2015) or no more than 1.5 (Stemmler et al., 2015). We suggest similar principles may apply to the efficient representation of time within place fields by theta phase given this quantitative agreement of the base used for representation. The matching scale factor used for logarithmic compression may also reflect the mechanistic connection between entorhinal input and hippocampal phase

precession (Fernández-Ruiz et al., 2017; Schlesiger et al., 2015), and may thus also point to similar principles of speed-invariance in spike timing patterns amongst grid cells. The fact that grid module scale changes with respect to the ratio but not the absolute difference in width (Barry et al., 2007; Stensola et al., 2012) is reminiscent of Weber's law that perception is proportional to relative changes rather than absolute changes in a stimulus. Weber's law is achieved in mathematical form by having perception be logarithmic with stimulus intensity (Portugal & Svaiter, 2011), and our work shows that the shape of phase precession in the hippocampus may support this very transformation for spatiotemporal information, with several associated predictions supported empirically here. This quantitative convergence to logarithmic coding can inspire productive investigation into the mechanisms and computational principles governing episodic memory processing in entorhinal-hippocampal circuits and potentially other brain circuits that must deal with variably timed sequences.

Overall, this work proposes and finds empirical support for a logarithmic latency code being implemented by hippocampal phase precession to form theta sequences that stably represent distances between fields, regardless of the variable time that elapses between them at different running speeds. This scale-to-offset transforming function of phase precession can supplement the traditional path integration framework that depends on a potentially noisy (Zilli & Hasselmo, 2010) and often saturating running speed signal (Hinman et al., 2016) to estimate distance, ensuring in the neural code the speed-invariance that is a defining feature of distance itself. The question of how to reconcile distance coding at different speeds also manifested in theta sequences being

proportional in length to running speed despite phase precession seemingly coding for a fixed distance regardless of running speed (Gupta et al., 2012; Maurer et al., 2012). This apparent paradox on the theta sequence population level was clarified by recent analysis showing that the apparent speed dependence of theta sequence trajectory lengths can be explained by the speed-dependence of place field width, with phase still stably coding for distance across laps (Parra-Barrero et al., 2021). To a similar end, we show that time sensitivity in the theta phase for distance also exists within individual fields particularly during acceleration (Supplementary Figure 9), and a distance-coding function for theta sequence that is invariant to speed can nevertheless arise using a logarithmic representation of spatiotemporal variables within theta cycles as achieved by the non-linear shape of phase precession.

It should be noted that previous work has used datasets involving tens of fields to initially assess the nonlinear shape of phase precession, finding that two normal distributions optimally describe the phase precession cloud, speculating either two separate mechanisms controlling phase precession in the two halves of a place field or an accelerating phase precession across a field, even in circular mazes where position-induced speed asymmetries were less likely to occur (Yamaguchi et al., 2001). Similarly, a dataset involving 100s of place fields found more phase variability was found in the 2nd half of a place field (Dragoi & Buzsáki, 2006), supporting a significant difference between first and second halves of the phase precession curve and arguing against a uniform slope or linear phase precession curve, instead suggesting a banana-shaped phase precession curve. Here we have analyzed data across more than 1000

place fields in support of a more quantitative framework in which this shape implements a logarithmic transformation from spatial navigation across time into theta phase, creating a scale-invariant code for space in the relative phase of place cell spikes.

2.5 Materials and Methods

Data subjects

All analyzed data comes from the linear maze, bilateral silicone probe recording sessions from hippocampal CA1 of 3 Long-Evans rats, including head-mounted LED data to track position and velocity simultaneous with electrophysiological recordings (Grosmark & Buzsáki, 2016). These are from the hc-3 dataset made publicly available by the Buzsaki lab on the Collaborative Research in Computational Neuroscience website (CRCNS.org). This dataset and associated descriptions can be obtained here:

Mizuseki, K., Sirota, A., Pastalkova, E., Diba, K., Buzsáki, G. (2013)
Multiple single unit recordings from different rat hippocampal and entorhinal regions while the animals were performing multiple behavioral tasks. CRCNS.org.
http://dx.doi.org/10.6080/K09G5JRZ

Only sessions involving CA1 place cells on linear maze tasks were extracted using the following sql command, yielding 80 sessions performed by rats ec013, ec14, and ec016:

```
'"SELECT distinct s.topdir, s.session, e.animal, s.duration ' ...
    'FROM cell c, session s, epos e, file f ' ...
    'WHERE c.topdir=s.topdir AND c.topdir=e.topdir AND s.session=f.session ' ...
    'AND c.region="CA1" '...
```

'AND (s.behavior = "linear" OR s.behavior = "linearOne" OR s.behavior = "linearTwo") '...

'ORDER BY s.duration desc;"

Data analysis

All analysis was performed using the MATLAB2017b software and the Great Lakes Computing Cluster at the University of Michigan. The following quantities were determined using these methods:

Theta phase

Theta phase of each spike was defined with respect to each cycle of the filtered LFP recorded from the reference channel in each session closest to the pyramidal cell layer of hippocampal CA1 as specified in the hc-3 meta-data. In particular, after peaks and troughs in the 6-12 Hz filtered LFP were initially identified, the maximum of the 6-40 Hz filtered LFP between the neighboring troughs of each peak was taken to define the more precise cycle boundaries (Ghosh et al., 2020). This is to account for the known asymmetry within theta cycles (Belluscio et al., 2012) and associated fast dynamics that are filtered out by the initial low-pass filter. After assigning each spike to a theta cycle defined this way, its theta phase was stored as the time from the beginning of that cycle to the spike time, divided by the duration of the cycle, multiplied by 360 degrees.

Place cells and fields

Place cells were initially identified using the same procedure as previously published (Grosmark & Buzsáki, 2016), including binning all spikes into 2 cm bins, smoothing with a 5 cm Gaussian kernel, and dividing this by the total time spend at each position to obtain firing rate for each position and direction of travel in each session. This also included removing cells with peak average firing rate of less than 1 Hz amongst these spatial bins, regardless of the shape of these fields. This was to consider all cells with enough place-specific spikes to allow quantitative evaluation of phase precession.

Strongly phase precessing cells and the spatial and temporal boundaries of phase precession for each field were chosen as the position and times at which theta phase coupling began and ended. In particular, including spikes accumulated across each whole session, positions at which theta phase was not significantly different from 0 were automatically detected by a one-sample test for mean direction by *circ_mtest* of the MATLAB CircStat toolbox (Berens, 2009). These boundaries were then adjusted by visual inspection to eliminate noisy detections. This semi-automatic boundary specification was important because rate-based boundary detection of place fields does not enclose the true boundaries of theta phase coupling (Souza & Tort, 2017) and thus phase precession dynamics as is of primary interest here. This process yielded 1227 different place fields used in all subsequent analyses unless otherwise stated.

Time remaining in field

The time remaining in field for any given spike is measured as the number of theta cycles that occur in between the spike and the time at which the field was exited. The

time at which a field was exited was determined as the next time at which the position time series, smoothed with a moving average using a 0.5 second window, crossed the field end position with positive speed. Speed was determined using the MATLAB function *movingslope* applied to the smoothed position time series over a 0.25 second window with a 1st order polynomial model. The total duration of each field was determined by collecting the maximum number of theta cycles remaining in field from each lap, disregarding those below 4 theta cycles and those from laps in which the animal's smoothed speed drops below 5 cm/s to avoid outlier-based distortion, and storing the 95th percentile of these values. When comparing across fields, the time in field associated with each spike was normalized by dividing by this total field duration.

Theta phase vs Time remaining in field relationship

Only spikes where the animal displayed a speed of at least 5 cm/s were included for distance-time coding comparison analysis (Figure 2A-C). Acceleration was calculated using the *movingslope* to estimate the time derivative of speed, using a 2nd order polynomial fit in a local window of 2 seconds. The conditional phase gain of distance and time were computed as the slope of the circular-linear fit to each curve. When comparing distance and time variables related to each spike, distance was discretized per theta cycle to resemble how time is measured in number of theta cycles, assigning each spike the average position the rat is in over the course of its corresponding theta cycle. To assess the error of linear models (Figure 3), the MATLAB function *angdiff* was used to calculate the circular difference between the phase predicted by the linear model at the spike's time in field, and the actual phase at that time in the field.

Linear-circular regression slope and correlation coefficient were acquired using the function *kempter_lincirc* as previously published for analysis of phase precession slope (Climer et al., 2013; Kempter et al., 2012). The code was modified to restrict the search space of circular-linear regression slopes between -3 and 3 when the linear variable was in normalized units to prevent the overfitting that often occurs with steep slopes that allow wrapping around the circular range. When circular-linear regression is used for comparing maximum probability phase values to time remaining in field, peak phase was computed as the phase corresponding to the peak of Gaussian kernel estimate of distribution obtained using CircStat function *circ_ksdensity.* Phase gain vs time was calculated using *movingslope*, with parameters set to estimate derivatives based on a 2^{nd} order polynomial fit in a local window of 0.2 of the total field duration or 3 theta cycles, whichever is larger. Heat maps show either circular mean phase (CircStat function *circ_mean*), joint probability distribution, or joint probability distribution given the x value, which is the joint probability with each column divided by the total probability of that column. These are smoothed with a 2D Gaussian kernel with a standard deviation of 1.26 bins instantiated over a square of width 7 bins, with the number of bins dividing the range in each dimension being 30 unless otherwise indicated.

Logarithm of time remaining in field

Wherever logarithm is mentioned, unless otherwise specified, we refer to the shifted and scaled version $(\log_b(x) + k)/k$ for x domain between 0 and 1 and with k=7 (Lisman &

Jensen, 2013) so that the output is also expressive in the range 0 and 1, or in the range 0 and 360 degrees when referring to phase within theta cycles. When identifying parameters of the logarithm, the units of cycle fraction between 0 and 1 rather than degrees are used for the output and units of fraction of field are used for the input. Quantification of the relationship between theta phase and the logarithm of time remaining in field are then the same as between theta phase and time remaining in field as above. When assessing phase gain across time, this was compared to the theoretical derivative of the logarithm which is given by the equation,

$$\frac{d}{dt}\log_b t = \frac{1}{t}\left(\frac{1}{\ln b}\right) \quad (1)$$

Determining base of logarithm

The base of the logarithm and the slope of the linear relationship between the inverse of time and time-derivative of the logarithm are also associated by equation (1). The proportionality constant of this relationship specifies the base of the logarithm (Figure 3) and can be estimated using linear statistics. Accordingly, for each field with at least 100 spikes, all theta cycles corresponding to a given remaining time in the field were grouped and the circular mean phase corresponding to each unique remaining time was computed. To compute the time-derivative of the relationship between mean phase and remaining time, the aforementioned function *movingslope* was used with 1st order model and a window size of 1/3rd of the field duration or 3 theta cycles, whichever is larger. To avoid spurious slopes associated with circular wraparound, the mean phase vs remaining time curve was circularly shifted in 1 degree increments until the number of

phase jumps greater than 180 degrees between consecutive cycles was minimized. The relationship between the inverse of the resulting temporal phase gain vs remaining time was assessed in the middle 60% of the field (to avoid edge effects) using the MATLAB function *robustfit* with default parameters to return a best linear fit slope reflecting the amount of curvature in the phase precession curve. Fields with 3 or less points to make this linear fit were excluded. The resulting slope was converted into a best-fit logarithm base by interpolated table-lookup of the same slope associated with numerically generated logarithmic curves of a range of bases. With each field having its associated best fit logarithm base, the logarithmic fit was completed by searching all possible offsets of a logarithm with the corresponding base in 1 degree and one-hundredth of a field duration increments for the one producing minimal mean circular error relative to the mean phase precession curve. The performance of the resulting logarithmic model was compared to that of a circular-linear regression model by computing the absolute value of the circular difference between the mean phase and predicted phase according to each model, at each cycle corresponding to a given remaining time in field. The median absolute error across the field was taken as a measure of performance of each model so that a logarithmic vs linear fit could be compared across the population of fields (Figure 3). Supplementary Figure 6 illustrates what the curvature corresponding to a similar range of logarithm bases looks like and its implications for the temporal resolution and dynamic range of the resulting coding scheme using theta phase bins. In particular, a base of 1.4 allows coding using a minimal separation of about 10 milliseconds, which could be physiologically distinguished by fast gamma oscillations (Bieri et al., 2014; Colgin, 2015). On the other

hand, a base of 1.2 allows only incomplete coding using 5 out of 7 bins, and a base of 2-3 implies timing separations on the timescale of an individual action potential and only half of the phase output domain or less for coding (Supplementary Figure 6).

Theta phase difference across cells

To compare coordination of theta phase across overlapping place fields in the last half as compared to the first half of theta cycles (Figure 4), we analyzed all pairs of place fields whose overlap facilitated such a scenario. This analysis requires focusing on place cell pairs that are overlapping and also whose field centers are spatially close enough such that their spike time representations both fit within the last half of theta cycles initially, and both transition into the first half of theta cycles later. Operationally this was defined to occur for place fields whose centers were no more than half the width of the smaller field apart. These pairs are likely to be represented by co-firing within the same half of a theta cycle, allowing differences between the first and last half of theta cycles to be assessed. Spike phase differences were calculated for every theta cycle in which both cells fire spikes that occur in the same order as the order of their respective field centers. These differences were calculated using the MATLAB function *angdiff*, and the resulting phase differences were separated by whether both spikes in the difference occurred in the first half or last half. These late and early groups were compared with a pairwise nonparametric test for a significant difference across all 377 field pairs tested.

Theta sequence property vs running speed theory

Equations:

The following equations show how the speed-phase signatures are predicted from each model during speed changes in which theta phase is coding for distance, linear time, or the logarithm of time, respectively.

Linear distance compression:

$$\theta_{dist}(t) = kd$$
$$\theta_{dist}\left(\frac{t}{s}\right) = kd \quad (2)$$
$$\boldsymbol{\theta_{dist}\left(\frac{t}{s}\right) = \theta_{dist}(t)}$$

Linear time compression:

$$\theta_{linear}(t) = kt$$
$$\theta_{linear}\left(\frac{t}{s}\right) = k\left(\frac{t}{s}\right)$$
$$\theta_{linear}\left(\frac{t}{s}\right) = \left(\frac{(kt)}{s}\right) \quad (3)$$
$$\boldsymbol{\theta_{linear}\left(\frac{t}{s}\right) = \frac{\theta_{linear}(t)}{s}}$$

Logarithmic time transform:

$$\theta_{log}(t) = \log(kt)$$

$$\theta_{log}\left(\frac{t}{s}\right) = \log\left(k\left(\frac{t}{s}\right)\right)$$

$$\theta_{log}\left(\frac{t}{s}\right) = \log(kt) - \log(s) \quad (4)$$

$$\boldsymbol{\theta_{log}\left(\frac{t}{s}\right) = \theta_{log}(t) - \log(s)}$$

, where $\boldsymbol{\theta_{model}}(t)$ gives the theta phase associated with time *t* as predicted by the corresponding model, *t* is the amount of time remaining until reaching the end of the field, *k* is a proportionality constant converting between behavioral time or distance and theta phase, *d* is the distance remaining to the end of the field, and *s* is a time-warp factor proportional to the animal's running speed. For a linear distance compression model, the phase is determined by distance independent of time, implying no changes in phase separation or mean phase with an increase in running speed but a proportional increase in phase-time compression ratio to maintain the distance code (Figure 5B; Equation 2). We note that these predictions for the effect of speed on theta sequence properties are identical for other transformations of distance into theta phase, such as a logarithmic distance transformation, and therefore explicitly analyze the linear distance compression case as a representative of distance-phase coding here. For a linear time compression model, increases in running speed effectively cause time compression that become equally manifest in theta phase separation and mean theta phase, with phase and time in constant proportion such that phase-time compression ratio does not change with speed (Figure 5C; Equation 3). For a logarithmic theta transform model,

increases in running speed cause a negative shift in phase offset without affecting theta phase separation, but with a similar increase in phase-time compression ratio as in linear distance compression, allowing it to maintain constant phase differences despite changes in time separation (Figure 5D; Equation 4). Phase offset is estimated using mean phase as a model-free surrogate measure.

Theta sequence properties vs behavior

Theta sequences were identified by first collecting all theta cycles in which at least two place cells in a given session fired spikes. The corresponding theta sequence for each such theta cycle was taken to be the sequence of representative mean phases (*circ_mean*) of the spikes from each cell within the cycle. Only sequences of place fields in which the narrowest field was no less than 75% of the width of the widest field in the sequence were considered for analysis so that place fields were of similar size and percentage of field traversed was a meaningful quantity for comparison across fields. The distance within each field as a fraction of the field's respective width and the time remaining until the animal reached each field's end, relative to the longest typical duration amongst the fields, were also collected for each member in a given theta sequence. Typical duration for each field was defined as the peak of a Gaussian kernel estimate (MATLAB function *ksdensity)* of the distribution of field durations across laps. To control for position within a field sequence across laps, a representative position for each field sequence was defined as the peak of a Gaussian kernel estimate of the distribution of positions at which the same field sequence was detected, and only theta

sequences within 1/12th of an average field width of this representative position were considered for further analysis (dashed lines in Figure 5FG).

To help control for variation in distance separation amongst fields in addition to mean position, only sequences with an average distance separation within 15%-85% of the average field width in the sequence were considered for further analysis. Running speed was also assigned to each theta sequence as the average speed within the associated traversal from the earliest field start position to the latest field end position. Phase separation within each theta sequence was defined as the circular mean of consecutive circular differences (MATLAB function *angdiff*) amongst the representative phases of each participating field taken in the order of their respective field centers. Phase-time compression ratio for each theta sequence was defined as the absolute value of the average of such consecutive circular differences in phase, each divided by the difference in percentage time duration remaining to each field's respective end position as defined above. The mean phase of a theta sequence was taken to be the circular mean of the representative mean phases from each participating field.

To compare the phase separation within theta sequences against behavioral variables including distance between fields, running speed, acceleration, and progression within field, each behavioral variable was divided into 16 equally spaced bins in their respectively specified ranges (Supplementary Figure 6). The mean phase separation as described above was averaged within each bin for which the 3rd specified variable was

also in its color coded range and displayed +/- standard error of the mean for bins containing at least 10 field sequences.

Combined population data was analyzed by taking the mean value of each property corresponding to each of 12 speed bins between a minimum and maximum speed, with circular variability quantified using the upper and lower limits of the one-sample test for mean angle (*circ_mtest* of CircStats package) or with standard error of the mean for phase-time ratio (Figure 5H). Speed was normalized to allow comparison across field sequences with different characteristic widths by dividing the speed originally in meters per second by the average width of fields participating in a theta sequence, yielding speed units of field widths per second (written as fields/sec). Linear regression was used to assess the relationship between the running speed and the population level theta sequence properties. Individual field sequences with sufficient speed variation across laps were identified as those having at least one low speed traversal with speed less than 0.55 fields/sec and one high speed traversal with speed greater than 1.05 fields/sec (approximately ± 1 standard deviation from the mean speed across all field sequences). The difference between phase separation, phase-time compression ratio, and mean phase in these two groups of traversals for each individual field sequence was obtained, and the center of these distributions being different from 0 was statistically evaluated to assess the effect of speed and its direction (Figure 4I). The average distance in field and average separation in distance within each field sequence was also evaluated for the same group to assess whether the controlled differences in distance could nevertheless explain the results (Figure 4I).

LTT simulations with empirical movement trajectories

To simulate the predictions of the LTT framework for realistic movements including accelerations and decelerations within the traversal of a field sequence, all trajectories through field sequences in the dataset were first collected as 21,608 position time series, each with its starting time and position subtracted out. Four fields implementing LTT were simulated as starting phase precession at 360 degrees, 2 seconds (~15 theta cycles) prior to reaching its respective end using the same definition as above for defining field exit in data analysis, lasting for 2 seconds. The first field ended at 1 m and each subsequent field ending was offset by 10 cm relative its partially overlapping neighbor (see Supplementary Figure 8B). The theta sequence was obtained as the sequence of 4 phases exhibited by the 4 fields at the readout position of 0.8 m. The average speed and acceleration of each trajectory was determined using the same process as described above for data analysis and the predictions of LTT for theta sequence offset and mean separation were collected corresponding to the trajectories of various speeds and accelerations (Supplementary Figure 8BC).

Statistics

For testing whether correlation coefficients and slopes of phase vs phase gain relationships are significantly different from zero, and for paired sample difference data, we use the two-sided nonparametric Wilcoxon signed rank test. For statistical comparison of population medians such as conditional phase gain of distance in field and time in field and the median spike time difference between early and late theta

cycle spike pair groups, we employ the two-sided nonparametric Wilcoxon rank-sum test. To statistically test whether theta sequence properties (Figure 5) and behavioral parameters (Supplementary Figure 8) are different between high and low speed groups, we performed a bootstrap reshuffling test by shuffling the speed group label across all speed-property points to create 500,000 bootstrapped surrogate population pairs from which the corresponding differences were recomputed. This procedure captures the distribution of property differences between the groups that can be explained by random chance. The probability of observing differences by chance was computed as the area under this distribution more extreme than the difference computed for the original pair of speed groups. Significance was determined relative to a significance threshold of $p=0.05$.

2.6 Acknowledgements

2.7 Author Contributions

Conceptualization, T.T.J.; Methodology, T.T.J, O.J.A.; Investigation, T.T.J; Software, T.T.J, O.J.A.; Formal Analysis, T.T.J.; Visualization, T.T.J., Writing – Original Draft, T.T.J ; Writing – Review and Editing, T.T.J, O.J.A.; Funding Acquisition, O.J.A., T.T.J; Supervision, O.J.A.

2.8 Supplemental Figures and Tables

A

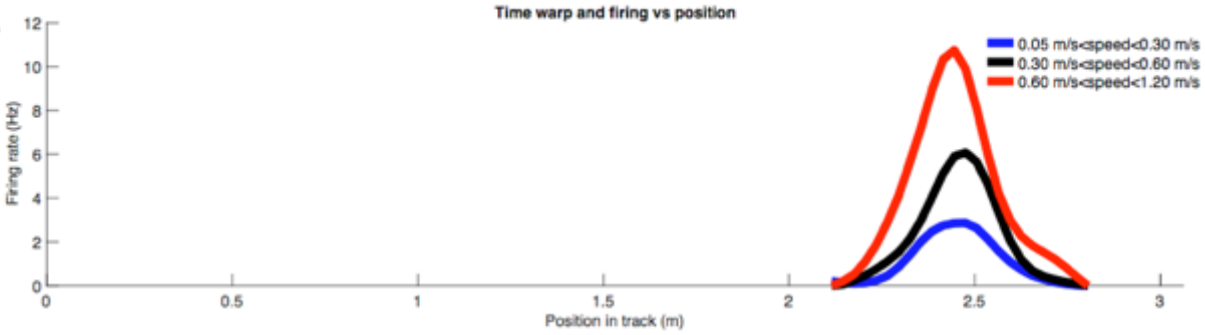
Time warp and firing vs position
0.05 m/s<speed<0.30 m/s
0.30 m/s<speed<0.60 m/s
0.60 m/s<speed<1.20 m/s
Firing rate (Hz)
Position in track (m)

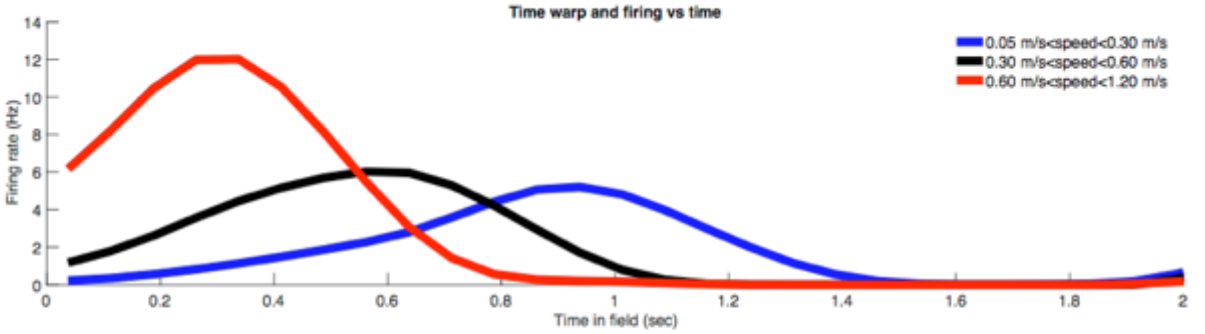
Time warp and firing vs time
0.05 m/s<speed<0.30 m/s
0.30 m/s<speed<0.60 m/s
0.60 m/s<speed<1.20 m/s
Firing rate (Hz)
Time in field (sec)

B

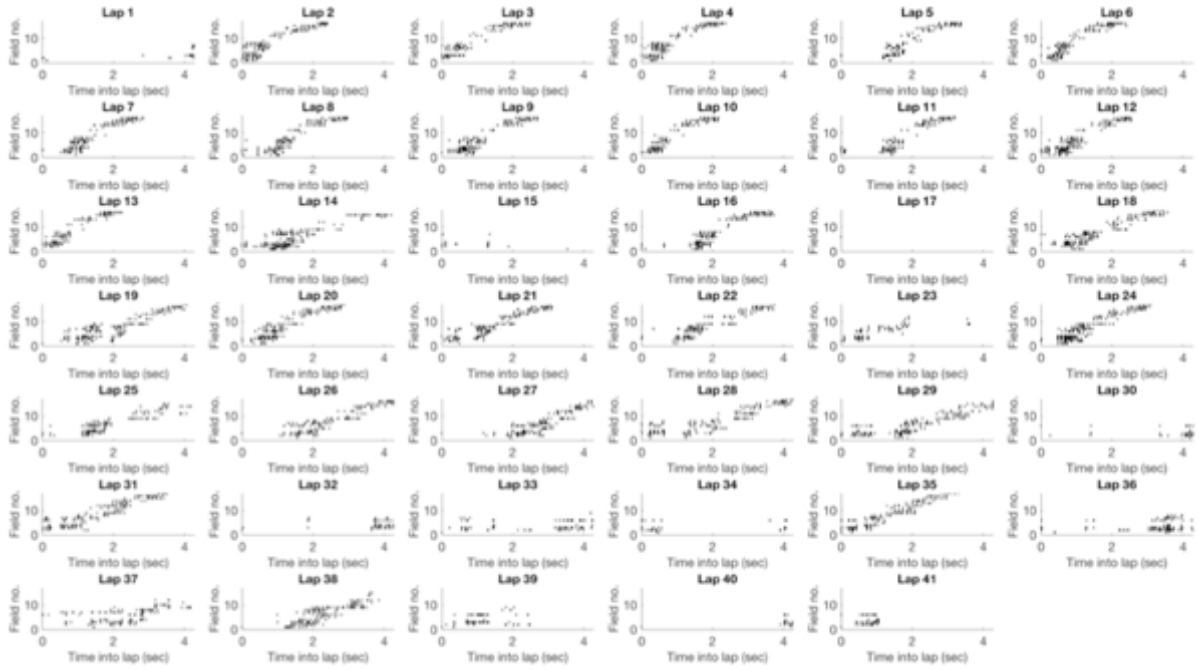
Lap 1
Lap 2
Lap 3
Lap 4
Lap 5
Lap 6
Lap 7
Lap 8
Lap 9
Lap 10
Lap 11
Lap 12
Lap 13
Lap 14
Lap 15
Lap 16
Lap 17
Lap 18
Lap 19
Lap 20
Lap 21
Lap 22
Lap 23
Lap 24
Lap 25
Lap 26
Lap 27
Lap 28
Lap 29
Lap 30
Lap 31
Lap 32
Lap 33
Lap 34
Lap 35
Lap 36
Lap 37
Lap 38
Lap 39
Lap 40
Lap 41
Field no.
Time into lap (sec)

Supplementary Figure 2-1. Firing rate level response to time-warp amongst place cells.

A) Demonstrations of time-warp via speed changes in the firing rate response of single place cell over position (upper) and time (lower).
B) Demonstration of time-warp of spike time raster plots via speed changes across laps within single session.

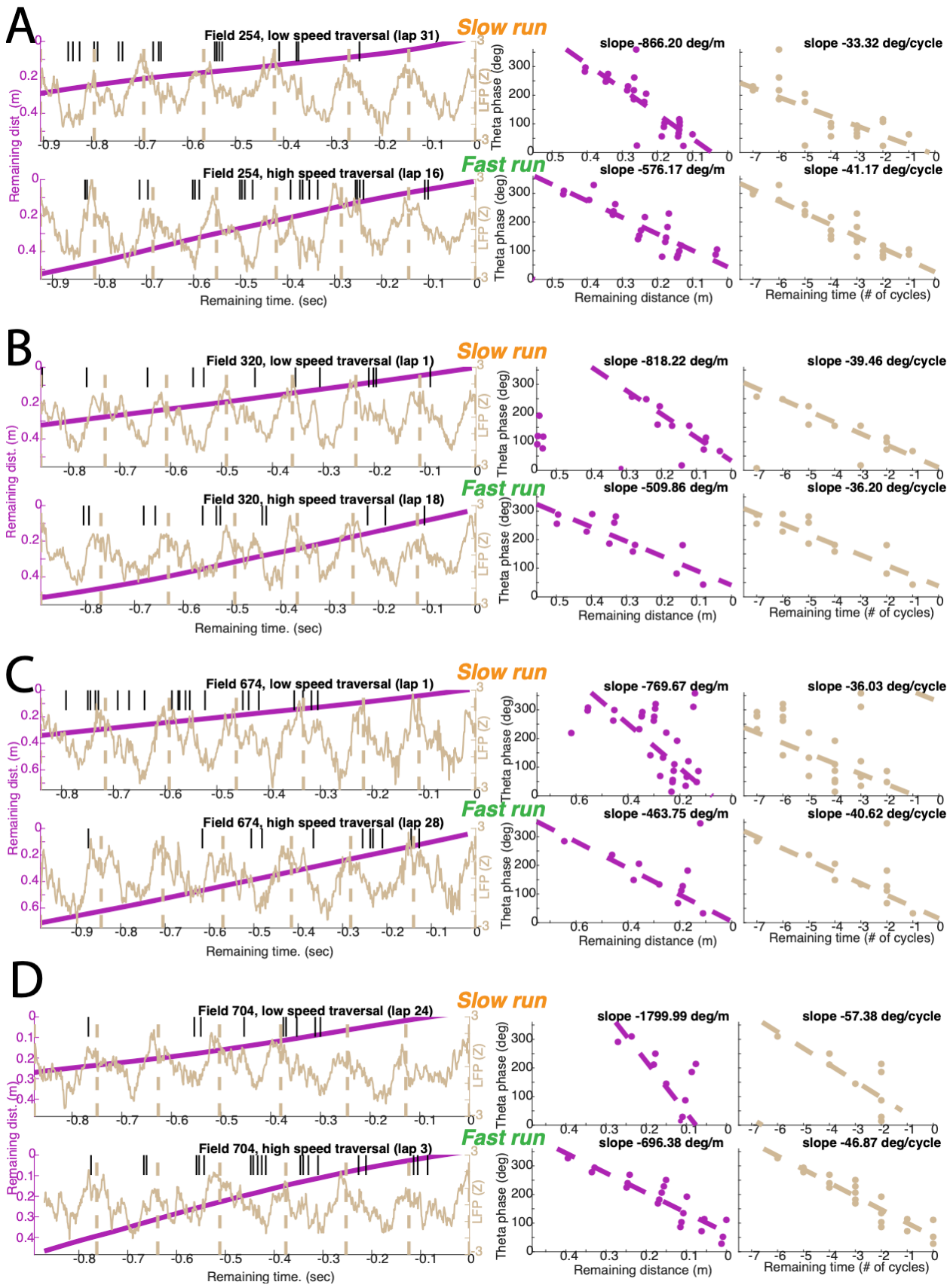
A
Field 254, low speed traversal (lap 31)
Slow run
slope -866.20 deg/m
slope -33.32 deg/cycle
Field 254, high speed traversal (lap 16)
Fast run
slope -576.17 deg/m
slope -41.17 deg/cycle
Remaining dist. (m)
LFP (Z)
Theta phase (deg)
Remaining time. (sec)
Remaining distance (m)
Remaining time (# of cycles)
B
Field 320, low speed traversal (lap 1)
slope -818.22 deg/m
slope -39.46 deg/cycle
Field 320, high speed traversal (lap 18)
slope -509.86 deg/m
slope -36.20 deg/cycle
C
Field 674, low speed traversal (lap 1)
slope -769.67 deg/m
slope -36.03 deg/cycle
Field 674, high speed traversal (lap 28)
slope -463.75 deg/m
slope -40.62 deg/cycle
D
Field 704, low speed traversal (lap 24)
slope -1799.99 deg/m
slope -57.38 deg/cycle
Field 704, high speed traversal (lap 3)
slope -696.38 deg/m
slope -46.87 deg/cycle

Supplementary Figure 2-2. Testing logarithmic theta transform (LTT) prediction 1 (continued): Theta phase correlates strongly with remaining time in field within individual fields.

A-D) Raw data from one example field during a lap with slow running (upper row) or fast running (lower row) but with the same remaining time (7 theta cycles) to the end of the field. Simultaneously shown are position (purple), theta oscillations (beige), and spike times (black) across time over the single traversal. Right panels corresponding to slow running lap (upper) and fast running lap (lower) show the theta phase of spikes plotted against remaining distance and remaining time.

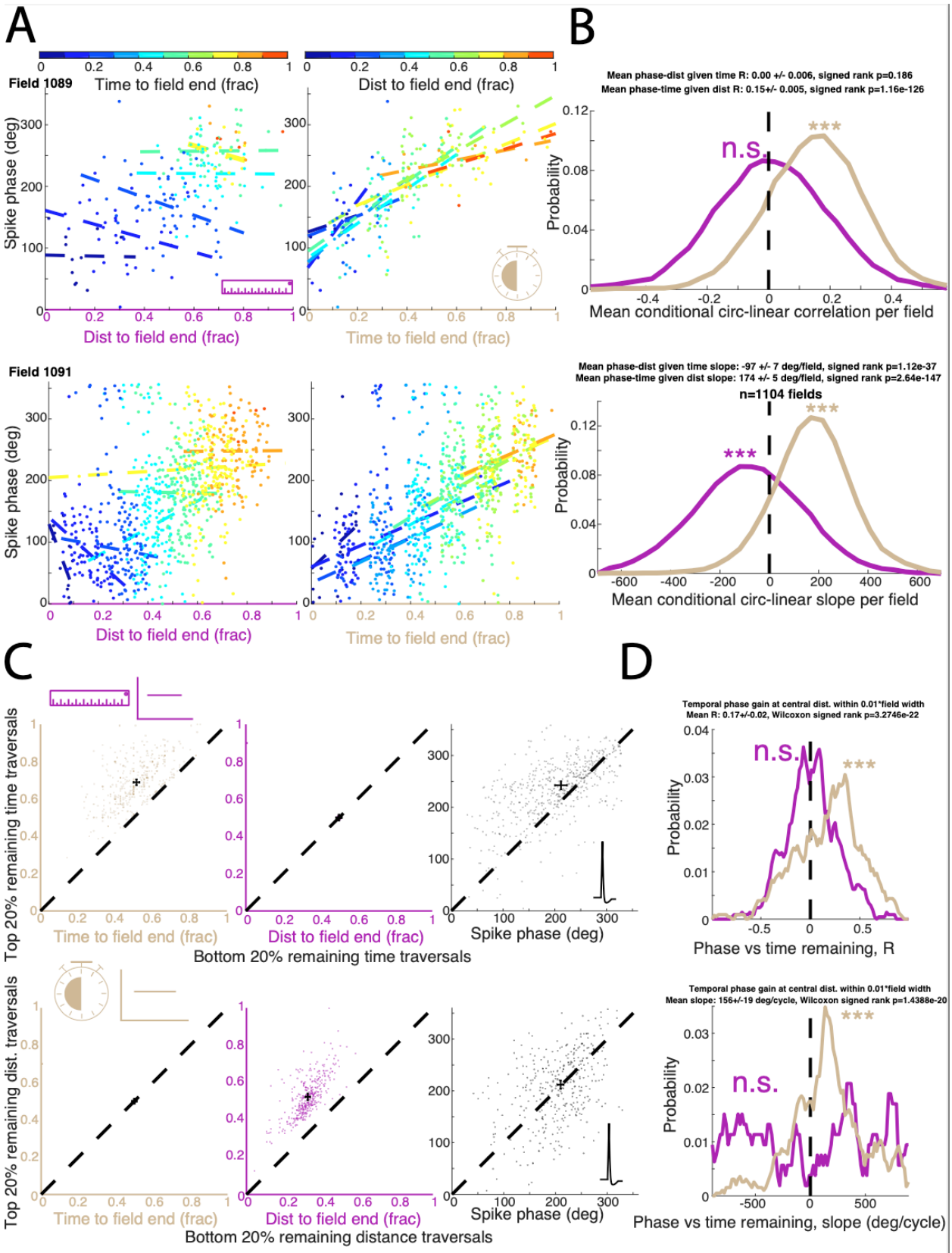
A
B
Field 1089
Time to field end (frac)
Dist to field end (frac)
Spike phase (deg)
Dist to field end (frac)
Time to field end (frac)
Mean phase-dist given time R: 0.00 +/- 0.006, signed rank p=0.186
Mean phase-time given dist R: 0.15+/- 0.005, signed rank p=1.16e-126
n.s.
***
Probability
Mean conditional circ-linear correlation per field
Field 1091
Mean phase-dist given time slope: -97 +/- 7 deg/field, signed rank p=1.12e-37
Mean phase-time given dist slope: 174 +/- 5 deg/field, signed rank p=2.64e-147
n=1104 fields
Mean conditional circ-linear slope per field
C
D
Top 20% remaining time traversals
Bottom 20% remaining time traversals
Spike phase (deg)
Temporal phase gain at central dist. within 0.01*field width
Mean R: 0.17+/-0.02, Wilcoxon signed rank p=3.2746e-22
Phase vs time remaining, R
Top 20% remaining dist. traversals
Bottom 20% remaining distance traversals
Temporal phase gain at central dist. within 0.01*field width
Mean slope: 156+/-19 deg/cycle, Wilcoxon signed rank p=1.4388e-20
Phase vs time remaining, slope (deg/cycle)

Supplementary Figure 2-3. Testing logarithmic theta transform (LTT) prediction 1 (continued):

Theta phase correlates strongly with remaining time in field when controlling for distance.

A) Example data from 2 place fields (top, bottom) showing the relationship between (left) theta phase and distance remaining in field when controlling for remaining time in field (analyzing only spikes occurring within 1% of the field duration), and that between (right) theta phase and time remaining in field when controlling for remaining distance (analyzing only spikes occurring within 1% of the field width). Dashed lines indicate the result of circular-linear regression. Random jitter is added to the remaining time to allow better visualization of otherwise overlapping data points.

B) (*top*) Distribution of average circular-linear regression correlation coefficients across population of fields between spike theta phase and remaining distance or time when controlling for the other. (*bottom*)) Distribution of average circular-linear regression slopes across population of fields between spike theta phase and remaining distance or time when controlling for the other.

C) (*top*) Each field with at least 6 data points in the controlled condition (spikes occurring within 1% of the field width) is represented as a dot in the space relating its mean value of remaining time (left), remaining distance (middle), and theta phase (right) in the low-remaining time group (x-coordinate) with its mean value in the high-remaining time group (y-coordinate) relative to the x=y line (dashed line). (*bottom*) Same as above except restricted to spikes occurring within 1% of field duration.

D) (*top*) Distribution of average circular-linear regression correlation coefficients across population of fields between spike theta phase and time restricted to spikes occurring within 1% of the field width. (*bottom*)) Distribution of average circular-linear regression slopes across population of fields between spike theta phase and time restricted to spikes occurring within 1% of the field width.

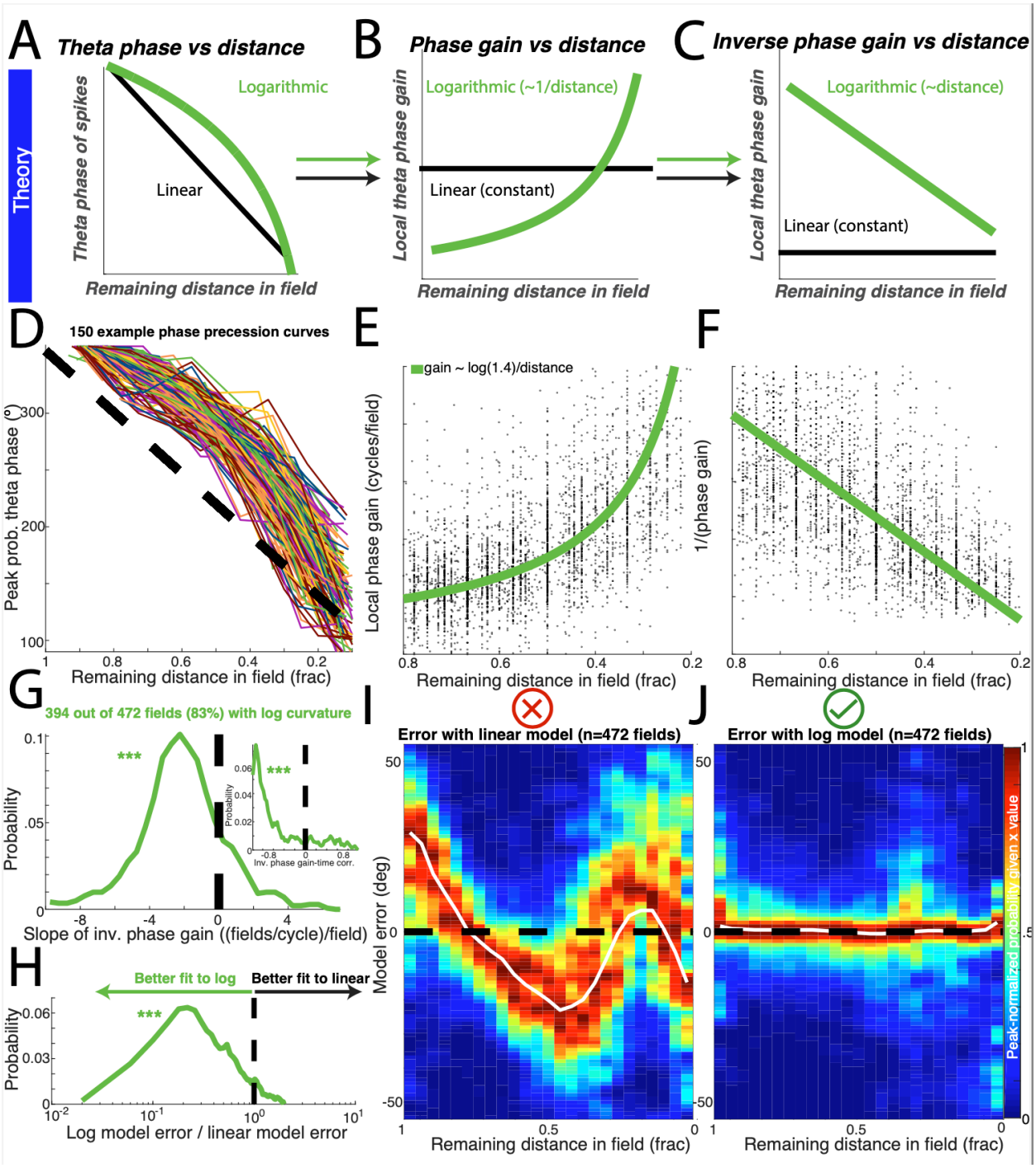

Supplementary Figure 2-4. Testing logarithmic theta transform (LTT) prediction 1 (continued): Theta phase has logarithmic relationship with theta-discretized distance remaining in place fields with quantitative specificity.

The following analysis is for all spikes from place fields with at least 100 spikes across all laps and at least 5 cycles in the central 60% of the field to estimate curvature (n=472 fields).

A) Schematic comparing predictions of LTT (*green*) and linear time compression (*black*) for the evolution of theta phase over remaining time in field.
B) Schematic comparing predictions of LTT (*green*) and linear time compression (*black*) for the evolution of theta phase gain over remaining time in field.
C) Schematic comparing predictions of LTT (*green*) and linear time compression (*black*) for the evolution of the multiplicative inverse of phase gain over remaining time in field.
D) 150 example phase precession curves with base higher than 1.3 (see panel G), each of one random color, showing peak probability theta phase corresponding to each remaining time in field
E) Local phase gain for each place field at each remaining time in field (*black dots*), and a curve showing k/(distance to end of field) (*green dashed line*) for k=log(1.4).
F) Multiplicative inverse of local phase gain for each place field at each remaining time in field (*black dots*), and a curve showing (distance to end of field)/k for k=log(1.4) (*green dashed line*).
G) Probability distribution of estimated k from linear fits of local phase gain vs remaining time in field for each place field. *Inset:* Probability distribution of correlation coefficient of local phase gain vs remaining distance in field for each place field showing significant linearity of the relationship (***, Wilcoxon signed rank test, p=1.634e-53). The peak slope corresponds to a peak probability logarithm base of 1.4.
H) Probability distribution of the ratio of absolute median error using a logarithmic model relative to that using circular-linear regression (***, Wilcoxon signed rank test, p=7.520e-34).
I) Probability distribution of angular error of a linear phase-distance at each remaining distance in field, showing systematic bias depending on remaining distance in field.
J) Probability distribution of angular error of logarithmic phase-distance model at each remaining distance in field, showing elimination of systematic bias depending on remaining distance in field.

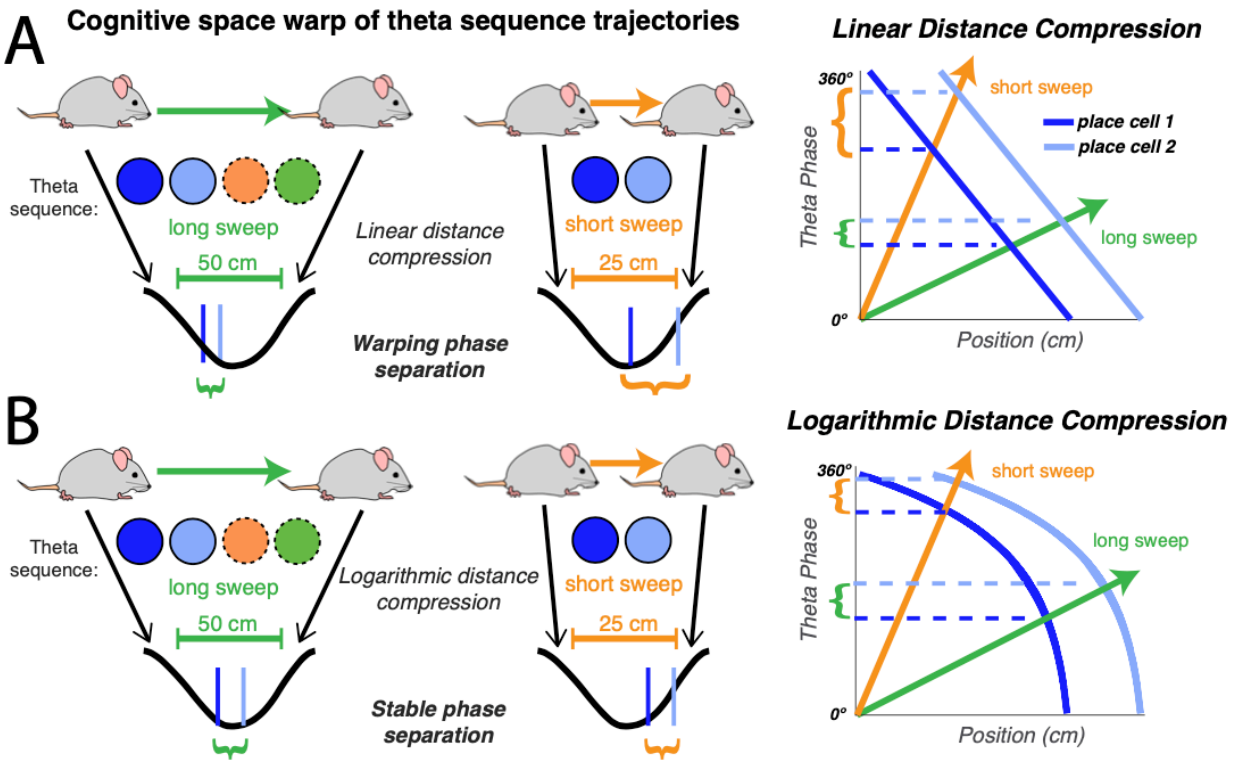

Supplementary Figure 2-5. The cognitive space-warp problem for warping of spike time patterns at different theta sequence trajectory lengths can be solved using the logarithmic theta transform (LTT) with respect to distance.

A) **(***left panel*) Illustration of a theta sequence involving 4 (long sweep, left) or 2 (short sweep, right) place fields depending on the cognitively determined spatial scale of the theta sequence trajectory. According to the theta phase coding model in which distance is compressed linearly into sequences on the theta cycle timescale (*right panel*), the same pair of fields has a variable amount of phase separation within the sequence depending on the space warp of the overall trajectory.

B) *Proposed implementation of space-warp invariant sequence coding using logarithmic distance compression. (left panel)* The effects of a logarithmic transformation of distance for the same theta sequences as in (A), during a long sweep (left) or short sweep (right). While the long sweep occurs over about 50 cm and 4 fields, the short sweep covers about 25 cm and 2 fields. Nevertheless, the distance between them becomes logarithmically compressed into a theta cycle (*right* panel) via the logarithmic theta transform. The two sweeps of differing lengths are mapped to the same phase separation only if the transformation is logarithmic.

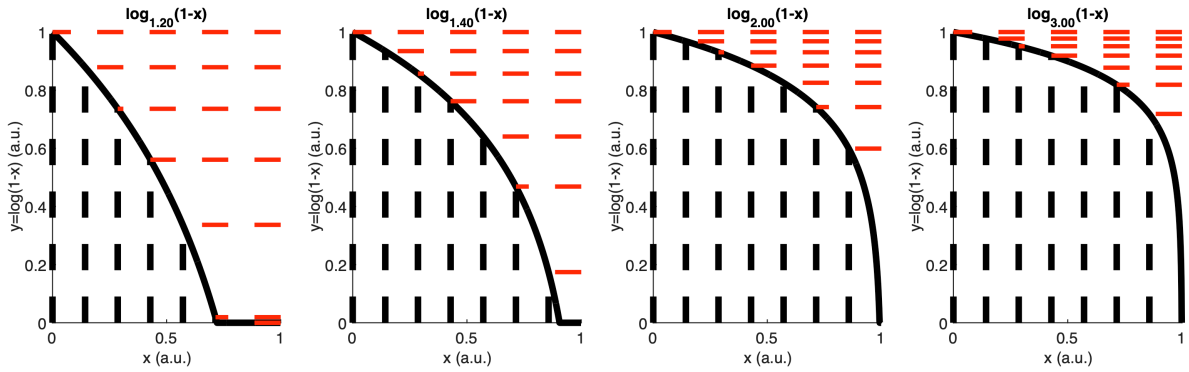

Supplementary Figure 2-6. Illustration of how logarithm base controls curvature and its coding properties.

The same equal-width bins in the x-domain, corresponding to elapsed time in this application, become mapped to differently spaced bins in the y domain, corresponding to theta phase bins here, depending on the base of the logarithm with a higher base corresponding to a greater concave curvature. Note that the base of 1.4, which represents the empirical mean base of phase precession in hippocampal place field, also corresponds to a minimum theta phase bin width of 0.084≈30 degrees≈10 msec. This approximately fits with the period of the fast gamma oscillations (~100 Hz) that group spike timing of pyramidal cells late within theta cycles. The maximal theta phase bin width of 0.3≈108 degrees≈36 msec approximately fits with the period of slow gamma oscillations (~30 Hz) that group spike timings early within theta cycles.

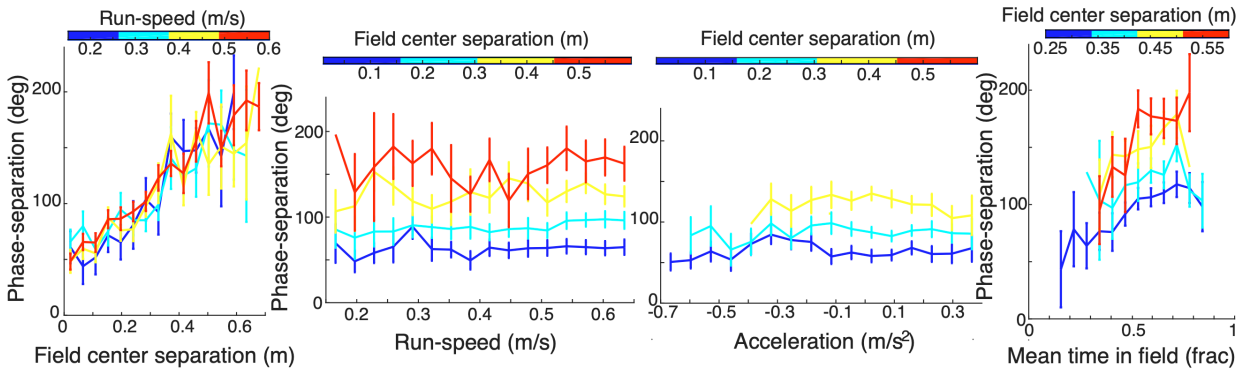

Supplementary Figure 2-7. Testing logarithmic theta transform (LTT) prediction 2: Theta sequences display a logarithmic spike timing difference gradient, decreasing in phase separation from early to late within theta cycles.

Mean phase separation within each theta sequence (n=831) was averaged within each bin for which the 3rd specified variable (field center separation, running speed, acceleration, and mean time in field) was also in its color coded range and displayed +/- standard error of the mean for bins containing at least 10 field sequences.

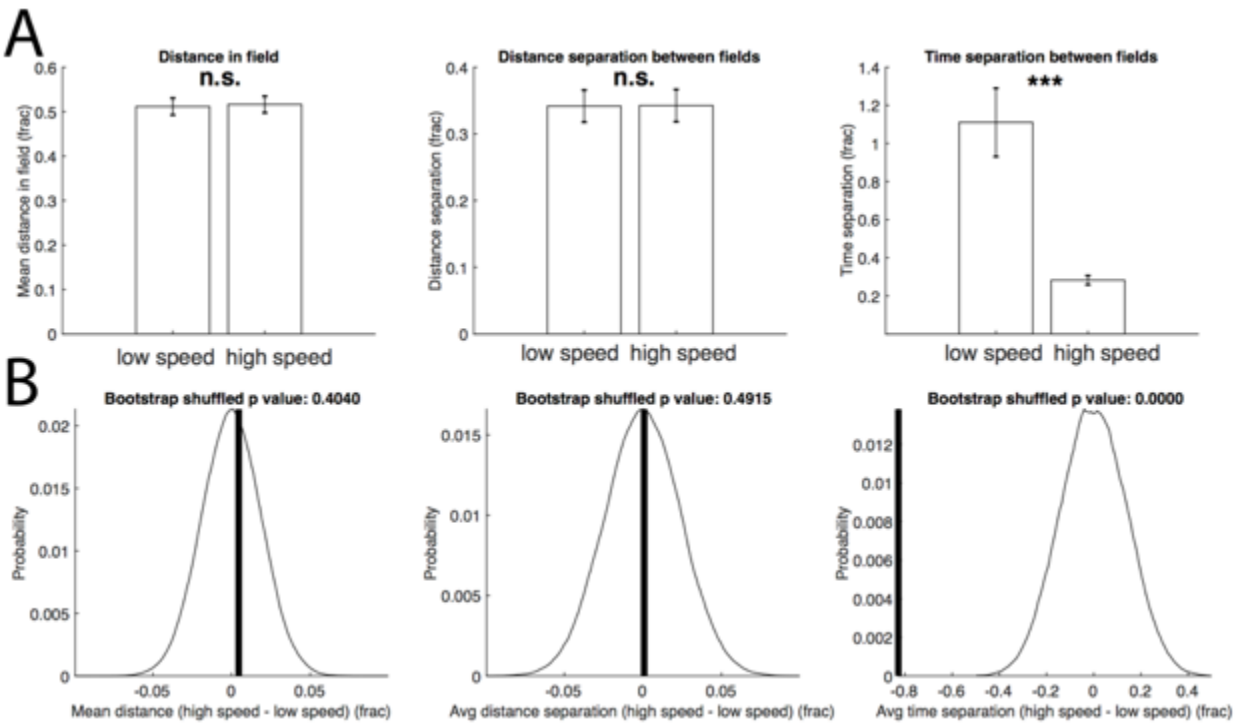

Supplementary Figure 2-8. Testing logarithmic theta transform (LTT) prediction 3 (continued): Distance within and between fields are well-controlled across speed groups, while time between fields is allowed to vary.

A) The average distance in field, average separation in distance, and average separation in time within each field sequence was evaluated for the low and high speed groups to assess whether the differences in distance are controlled while permitting differences in time separation with speed. Bar graphs show mean ± standard error of these metrics in low and high speed groups (n.s. = not significant, indicating $p>0.05$; *** indicates $p<0.001$; ** indicates $p<0.01$).

B) Probability distribution of surrogate differences when high and low speed labels are reshuffled amongst all data points N=500,000 times. The p-value is the probability of observing a difference equal to or more extreme than the observed difference, taken as the area under the curve corresponding to these values.

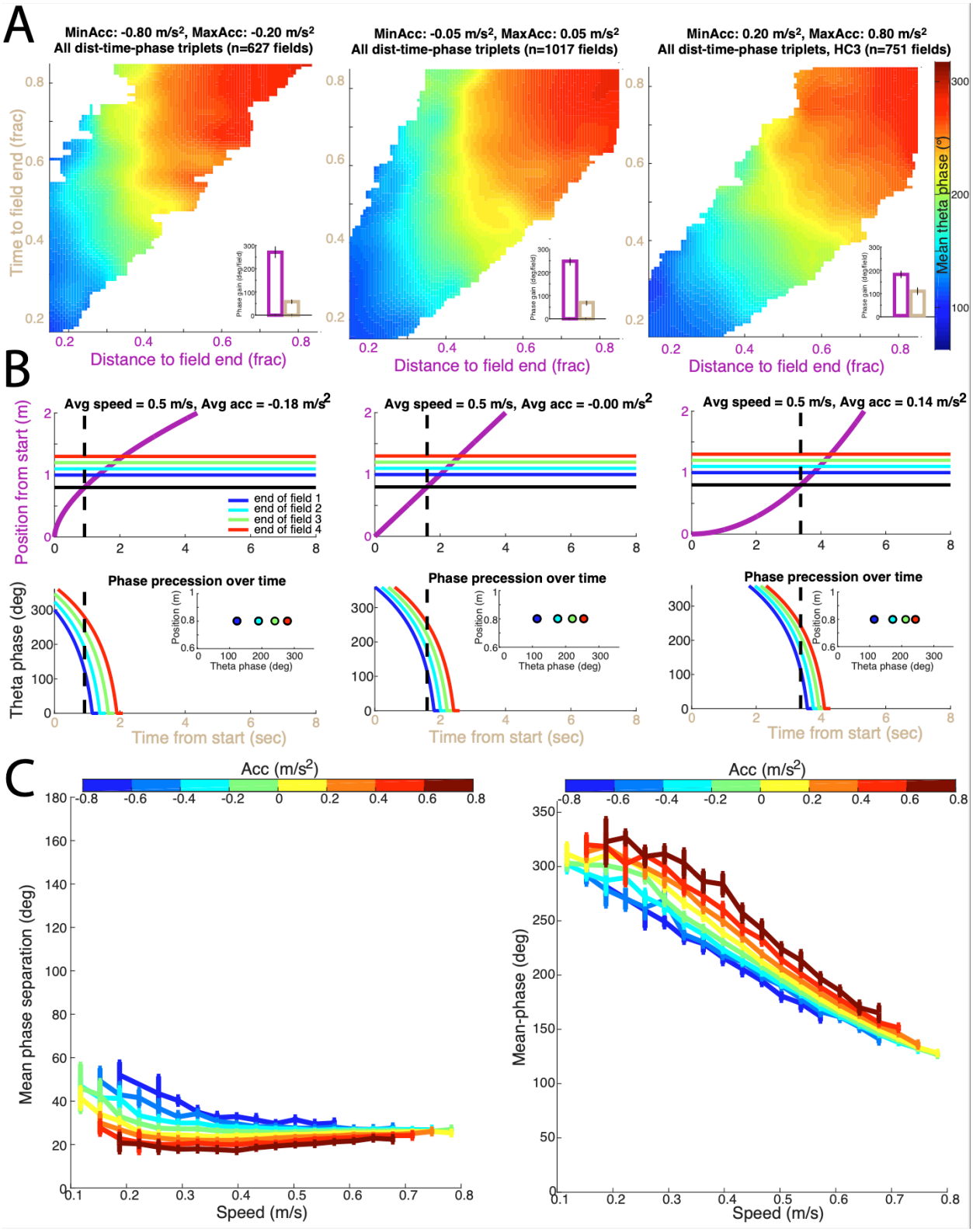
A
MinAcc: -0.80 m/s², MaxAcc: -0.20 m/s²
All dist-time-phase triplets (n=627 fields)
MinAcc: -0.05 m/s², MaxAcc: 0.05 m/s²
All dist-time-phase triplets (n=1017 fields)
MinAcc: 0.20 m/s², MaxAcc: 0.80 m/s²
All dist-time-phase triplets, HC3 (n=751 fields)
Time to field end (frac)
Distance to field end (frac)
Phase gain (deg/field)
Mean theta phase (°)
B
Avg speed = 0.5 m/s, Avg acc = -0.18 m/s²
Avg speed = 0.5 m/s, Avg acc = -0.00 m/s²
Avg speed = 0.5 m/s, Avg acc = 0.14 m/s²
Position from start (m)
end of field 1
end of field 2
end of field 3
end of field 4
Phase precession over time
Theta phase (deg)
Position (m)
Time from start (sec)
C
Acc (m/s²)
Mean phase separation (deg)
Mean-phase (deg)
Speed (m/s)

Supplementary Figure 2-9. Effect of realistic accelerations and decelerations on LTT predictions, empirical phase precession, and empirical theta sequence properties.

A) Reanalysis of phase precession surface (see Figure 2) restricted to traversals of deceleration (left), constant speed (middle), or acceleration (right) showing similar result of control of theta phase by time in addition to distance, particularly in the accelerating traversal group.
B) Theta sequence properties at a given position (dashed line) resulting from LTT model simulated for 4 overlapping place fields at high deceleration (left), constant speed (middle), or high acceleration (right), showing mild deformation of spacing and offset.
C) Simulation of theta sequence properties produced by LTT using all empirical traversals binned by amount of deceleration/acceleration. Shows decreasing phase offset and increasing phase separation with deceleration but within a relatively restricted range. Each mean is showed with error bars representing standard error of the mean.

Stand-alone Supplementary Figures

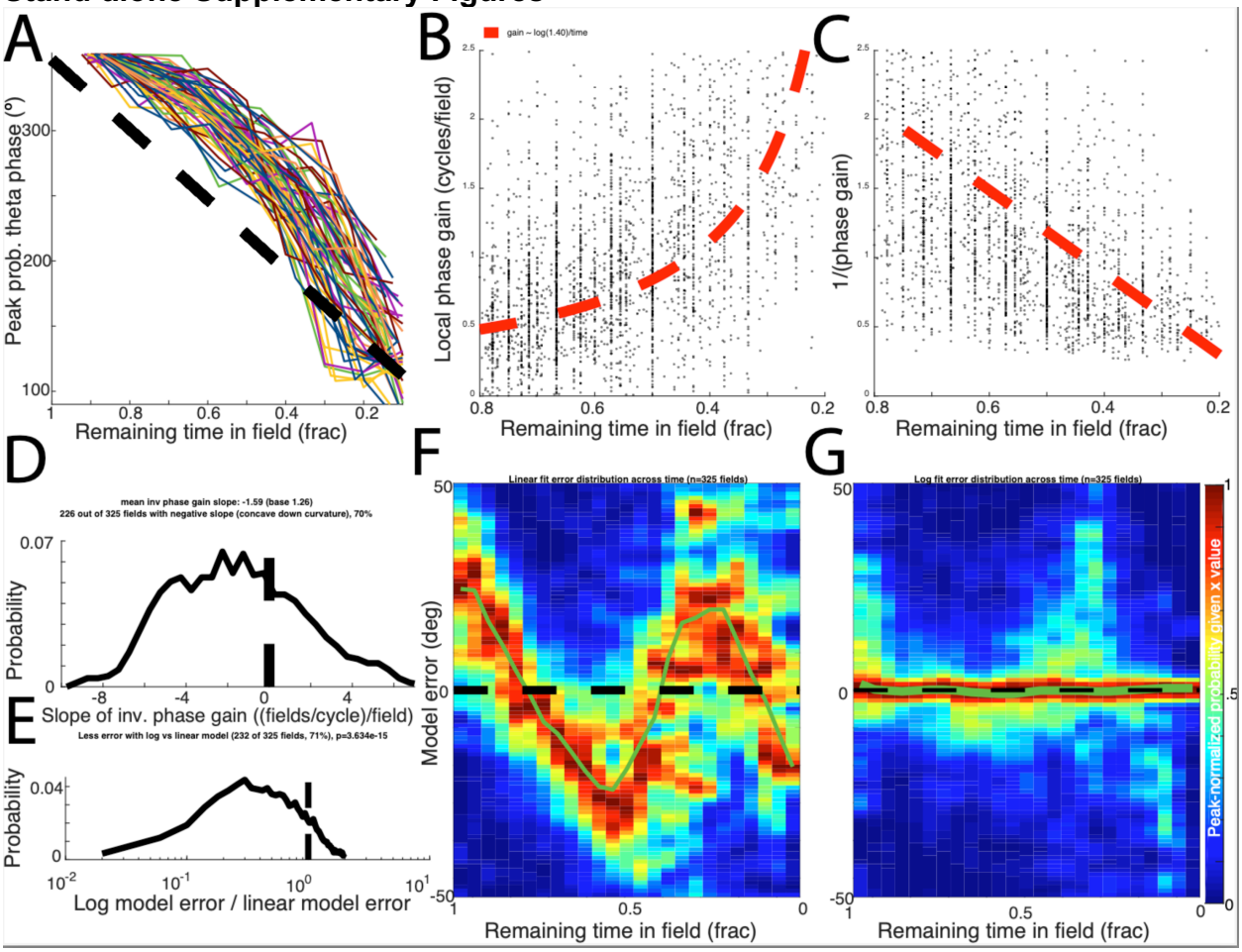

Supplementary Figure 2-10. Testing logarithmic theta transform (LTT) prediction 1 (continued): Theta phase has logarithmic relationship with continuous time (total theta phase) remaining in place fields with quantitative specificity.

The following analysis is for all spikes from place fields with at least 100 spikes across all laps and at least 5 cycles in the central 60% of the field to estimate curvature (n=325 fields).

A) Example phase precession curves with base higher than 1.3 (see panel G), each of one random color, showing peak probability theta phase corresponding to each remaining time in field
B) Local phase gain for each place field at each remaining time in field (*black dots*), and a curve showing k/(time to end of field) (*green dashed line*) for k=log(1.4).
C) Multiplicative inverse of local phase gain for each place field at each remaining time in field (*black dots*), and a curve showing (time to end of field)/k for k=log(1.4) (*green dashed line*).
D) Probability distribution of estimated k from linear fits of local phase gain vs remaining time in field for each place field. The peak slope corresponds to a peak probability logarithm base of 1.3.
E) Probability distribution of the ratio of absolute median error using a logarithmic model relative to that using circular-linear regression (***, Wilcoxon signed rank test, p=3.634e-15).
F) Probability distribution of angular error of a linear phase-time at each remaining time in field, showing systematic bias depending on remaining time in field.
G) Probability distribution of angular error of logarithmic phase-time model at each remaining time in field, showing elimination of systematic bias depending on remaining time in field.

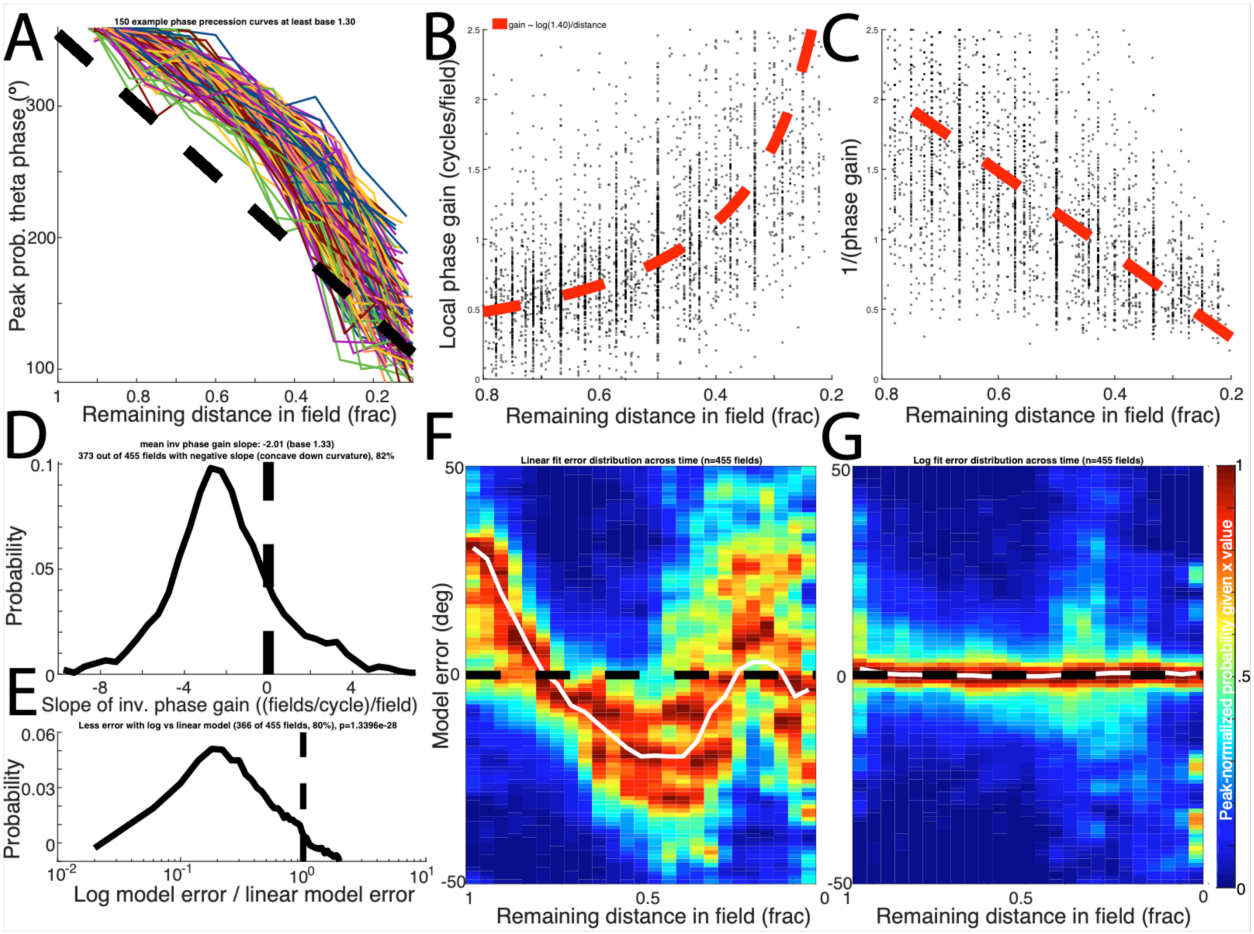

Supplementary Figure 2-11. Testing logarithmic theta transform (LTT) prediction 1 (continued): Theta phase has logarithmic relationship with continuous distance remaining in place fields with quantitative specificity.

The following analysis is for all spikes from place fields with at least 100 spikes across all laps and at least 5 cycles in the central 60% of the field to estimate curvature (n=373 fields).

A) 150 example phase precession curves with base higher than 1.3 (see panel G), each of one random color, showing peak probability theta phase corresponding to each remaining time in field
B) Local phase gain for each place field at each remaining time in field (*black dots*), and a curve showing k/(distance to end of field) (*green dashed line*) for k=log(1.4).
C) Multiplicative inverse of local phase gain for each place field at each remaining time in field (*black dots*), and a curve showing (distance to end of field)/k for k=log(1.4) (*green dashed line*).
D) Probability distribution of estimated k from linear fits of local phase gain vs remaining time in field for each place field. The peak slope corresponds to a peak probability logarithm base of 1.3.
E) Probability distribution of the ratio of absolute median error using a logarithmic model relative to that using circular-linear regression (***, Wilcoxon signed rank test, p=1.3396e-28).
F) Probability distribution of angular error of a linear phase-distance at each remaining distance in field, showing systematic bias depending on remaining distance in field.
G) Probability distribution of angular error of logarithmic phase-distance model at each remaining distance in field, showing elimination of systematic bias depending on remaining distance in field.

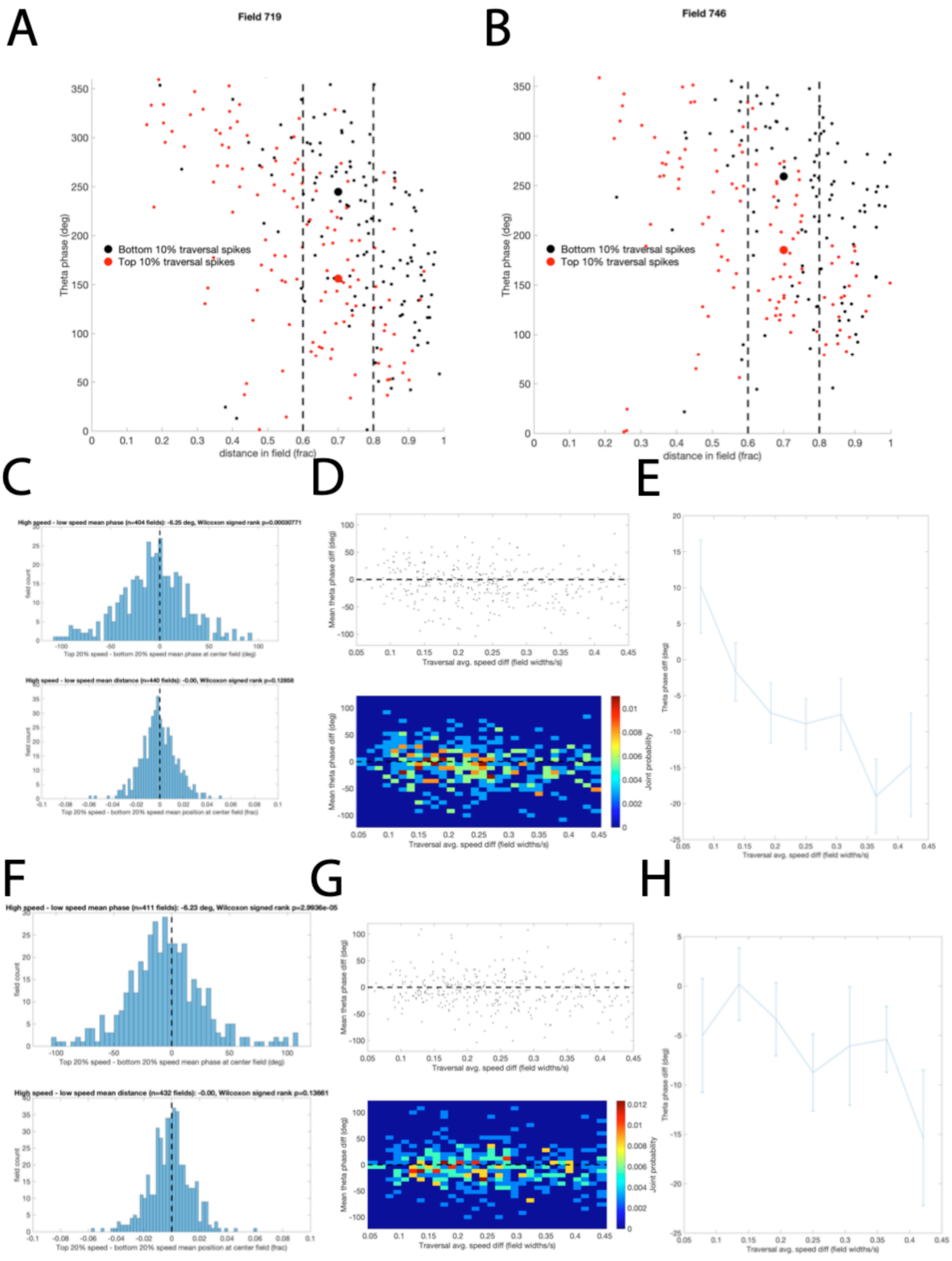
A
Field 719
Theta phase (deg)
distance in field (frac)
Bottom 10% traversal spikes
Top 10% traversal spikes
B
Field 746
Theta phase (deg)
distance in field (frac)
Bottom 10% traversal spikes
Top 10% traversal spikes
C
High speed - low speed mean phase (n=404 fields): -6.25 deg, Wilcoxon signed rank p=0.00030771
field count
Top 20% speed - bottom 20% speed mean phase at center field (deg)
High speed - low speed mean distance (n=440 fields): -0.00, Wilcoxon signed rank p=0.12858
field count
Top 20% speed - bottom 20% speed mean position at center field (frac)
D
Mean theta phase diff (deg)
Traversal avg. speed diff (field widths/s)
Mean theta phase diff (deg)
Traversal avg. speed diff (field widths/s)
Joint probability
E
Theta phase diff (deg)
Traversal avg. speed diff (field widths/s)
F
High speed - low speed mean phase (n=411 fields): -6.23 deg, Wilcoxon signed rank p=2.9936e-05
field count
Top 20% speed - bottom 20% speed mean phase at center field (deg)
High speed - low speed mean distance (n=432 fields): -0.00, Wilcoxon signed rank p=0.13661
field count
Top 20% speed - bottom 20% speed mean position at center field (frac)
G
Mean theta phase diff (deg)
Traversal avg. speed diff (field widths/s)
Mean theta phase diff (deg)
Traversal avg. speed diff (field widths/s)
Joint probability
H
Theta phase diff (deg)
Traversal avg. speed diff (field widths/s)

Supplementary Figure 2-12. Testing logarithmic theta transform (LTT) prediction 1 (continued):

Theta phase at given distance becomes lower at higher running speeds in individual fields.

A) Example data from place field showing the relationship between theta phase and distance remaining in field from traversals with average speed in the bottom 10% of traversal average speeds for the field (black) and the same for traversals in the top 10% (red). Dashed lines indicate example boundaries of position over which circular mean phase was commuted for each group (large dots).
B) Example data analogous to (A) for another representative place field.
C) (*top*) Distribution of the difference in average circular mean phase in position bounds shown in A and B (0.7+/- 0.1 fraction of distance within field) between high speed and low speed traversal group, showing a significant reduction in phase (Wilcoxon signed rank p=0.00031). (*bottom*) Distribution of difference in average distance in field within position bounds shown in A and B (0.7+/- 0.1 fraction of distance within field) between high speed and low speed traversal group, show no significant difference in average position (Wilcoxon signed rank p=0.1286), precluding a distance confound as explaining the reduction in phase.
D) Beyond a reduction in mean phase at a given distance (0.7+/- 0.1 fraction of distance within field) with running speed for each field, fields with a larger difference in running speed in the top and bottom 10% of traversals should also show a larger difference in mean phase if phase is time-sensitive, i.e. the running speed difference should be correlated with mean phase difference at a given position. The top panel shows a point (black dot) for each field indicating its mean phase difference (y-ccordinate) and mean speed difference (x-coordinate) between the two speed groups, normalized by the typical (peak probability) traversal speed characteristic to each field. Bottom panel shows the same data as a heatmap of joint probability in this space. Both show a negative correlation between phase difference and speed difference at the given position, consistent with phase-time sensitivity.
E) Bin-averaged phase difference +/- SEM within 7 equally spaced speed difference bins, showing negative relationship between phase difference and speed difference, consistent with phase-time sensitivity within individual fields.
F) Analagous to (C) with fixed distance of 0.6+/- 0.1 fraction of distance within field
G) Analagous to (D) with fixed distance of 0.6+/- 0.1 fraction of distance within field
H) Analagous to (E) with fixed distance of 0.6+/- 0.1 fraction of distance within field

CHAPTER 3: Two Modes of Inhibitory Shutdown Distinctly Amplify Seizures In Humans

3.1 Abstract

Inhibitory neurons are critical for normal brain function but dysregulated in disorders such as epilepsy. At least two theories exist for how inhibition may acutely decrease during a seizure: hyperpolarization of fast-spiking (FS) inhibitory neurons by other inhibitory neurons, or depolarization block (DB) of FS neurons resulting in an inability to fire action potentials. Firing rate alone is unable to disambiguate these alternatives. Here, we show that human FS neurons can stop firing due to both hyperpolarization and DB within the same seizure. However, only DB of FS cells is associated with dramatic increases in local seizure amplitude, unobstructed traveling waves, and transient increases in excitatory neuronal firing. This result is independent of seizure etiology or focus. Computational models of DB reproduce the *in vivo* human biophysics. These methods enable intracellular decoding using only extracellular recordings in humans and explain the otherwise ambiguous inhibitory neuronal control of human seizures.

3.2 Introduction

Epilepsy is a debilitating disease affecting some 50 million people worldwide (de Polavieja, 2005; Thurman et al., 2011). Epileptic seizures are thought to result from an imbalance between excitatory and inhibitory neuronal activity (Žiburkus et al., 2013). However, electrographically similar seizures on the macroscopic scale can be driven by mechanistically distinct processes on the cellular and cell-type population scale (Farrell et al., 2019). Thus, the relative roles of local inhibitory and excitatory networks in driving seizure progression must be elucidated to guide the development of novel treatments for intractable epilepsies and our understanding of their associated seizures. Due to the tremendous technical challenges of recording from individual human neurons and the relative sparsity of inhibitory neurons, the activity of well isolated inhibitory interneurons during seizures is only rarely examined (Elahian et al., 2018; Weiss et al., 2016).

There are several theories, based on slice and whole animal experiments, proposing both insufficient (Chagnac-Amitai & Connors, 1989; Gutnick et al., 1982; Karlócai et al., 2014; McCormick et al., 1985; Pavlov & Walker, 2013; Prince & Connors, 1984; Schwartzkroin & Prince, 1980; Trevelyan & Schevon, 2013; Ziburkus et al., 2006) and excessive (Avoli & de Curtis, 2011; Cope et al., 2009; Lévesque et al., 2016; Neumann et al., 2017; Sessolo et al., 2015) inhibition as possible facilitators of epileptic activity, with at least two hypotheses for how inhibition may acutely decrease during a seizure: (1) hyperpolarization of fast-spiking (FS) inhibitory neurons by other inhibitory neurons (Buckmaster et al., 2000; Khoshkhoo et al., 2017; Miri et al., 2018; Xu et al., 2013), or (2) excessive depolarization of FS neurons that precludes subsequent action potentials

due to blockade of voltage-dependent sodium channels (Cammarota et al., 2013; Karlócai et al., 2014; Ziburkus et al., 2006). Resolving these two theories necessitates whole cell recordings (Petersen, 2017), but it is practically impossible to record the intracellular membrane potential of neurons during human seizures *in vivo.* In this study, we address these challenges by combining (1) large-scale extracellular recordings of human neocortical inhibitory and excitatory neurons during focal seizures with secondary generalization and (2) a novel method of decoding membrane potential trajectory from extracellular action potentials. We show the remarkable ability of active fast-spiking inhibitory neurons to block epileptic traveling waves in human neocortex, and reveal the dynamical control of human seizures by the subthreshold trajectory of inhibitory neurons.

My contribution to this collaborative work included conducting all formal analysis and visualization of all main and supplementary data as figures, other than Figure 3-3 made by O.J.A. I also conceptualized the methodology used here to assess unit waveform sortability dynamically across time as a modification to the previous methods assuming stationarity. Discussions between myself and O.J.A constituted conceptualization of our method of inferring subthreshold dynamics from extracellular waveform shape during seizure progression. I also contributed to writing, reviewing, and editing the manuscript, particularly drafting and editing the results and methods descriptions relevant to each analysis, as well as relevant sections of the introduction and discussion. This chapter has also been deposited as a medRxiv preprint (https://doi.org/10.1101/2020.10.09.20204206).

3.3 Results

Patients were implanted with intracranial grid electrodes as part of the clinical process of identifying the precise site of origin of their drug-resistant focal epilepsy (see Materials and Methods). A 4x4 mm NeuroPort microarray (Blackrock Microsystems) was also placed in a region of the neocortex that was expected to be in the resection site (Figure 1a; Extended Data Fig. 1a). Histology of the resected tissue confirmed that the electrodes consistently targeted layers 2/3 of the neocortex (Extended Data Fig. 1b). We used these arrays to simultaneously record the activity of dozens of individual neocortical neurons during both ictal and interictal activity. We then classified the neurons as either fast-spiking (FS) inhibitory interneurons or regular-spiking (RS) excitatory cells using well-established criteria (Cardin et al., 2009; Nowak et al., 2003), including action potential shape (Extended Data Fig. 1c-f). FS cells correspond to the class of parvalbumin-expressing interneurons and represent the largest source of inhibition in the neocortex(Rudy et al., 2011). The resulting information thus allowed us to differentiate between putative inhibitory and excitatory unit activity patterns during seizure progression in humans.

A total of 37 FS cells and 539 RS cells were recorded across 4 patients with NeuroPort arrays implanted in the temporal neocortex (see Supplementary Methods for details about each patient). As secondarily generalized seizures first reached the arrays, both FS and RS cells increased their rate of action potentials (Figs. 1, 2, and Extended Data Figs. 2-4). This finding is consistent with what is known about the feedforward

recruitment of both inhibition and excitation (Cammarota et al., 2013; Connors et al., 2001). At the population level, the FS firing rate was significantly higher than RS cells (100,000 bootstrap iterations of label-shuffled peak rate differences; $p=0.036$). Within 40 seconds of seizure onset, the mean FS firing rate fell rapidly to 0-2 Hz at the same time as local field potential intensity increased dramatically to its highest levels (Figs. 1, 2, and Extended Data Figs. 2-4). Consistently, among the best isolated FS units during the seizure (isolation quality discussed in more detail below and see Methods), 10 out of 15 had at least one nearby RS cell that exhibited the peak of its overall activity several seconds after the dramatic fall in local FS activity and accompanying elevation in local field potential intensity (Figs. 1, 2, and Extended Data Figs. 2-4). Thus, at the population level, FS cells show a cessation of activity near the middle of secondarily generalized seizures accompanied by a dramatic increase in the amplitude of seizure activity. This FS cessation is followed by a transient increase in RS cell firing, presumably because these RS cells are now less inhibited due to the loss of FS firing. The RS population rate eventually also fell to an average of 0-3 Hz but with a delay of several seconds following FS cells. At the population level, FS cells (N=37) exhibited significantly earlier cessation times than RS cells (N=539) (Fig. 2g-j, FS cell average cessation occurred 4.6 seconds earlier than RS average cessation; 100,000 bootstrap iterations of label-shuffled time differences; $p<0.0001$).

We next compared activity patterns among individual FS cells. Many individual FS cells did not start firing until ~10 seconds into the seizure, often starting to fire robustly only after the RS rate had already increased (Figs. 1, 2, and Extended Data Figs. 2-4). As

seen with the population means (Fig. 2g), each individual FS cell dramatically reduced its firing roughly half-way through the seizure (Figs. 1, 2, and Extended Data Figs. 2-4). However, even simultaneously recorded FS cells during a single seizure did not necessarily cease firing at the same time, just as they did not start firing at the same time. Figure 1 shows the activity of two simultaneously recorded FS cells that were separated by a distance of 2.04 mm. FS Cell 1 (Fig. 1a) approached cessation ~35 seconds into the seizure, and at ~35 seconds, the amplitude of the LFP next to FS Cell 1 increased dramatically, as did the firing rate of nearby RS cells. FS Cell 2 (Fig. 1b) approached cessation ~24 seconds into the seizure, and the LFP amplitude next to FS Cell 2 also increased at ~24 seconds, along with the firing rate of nearby RS cells. Furthermore, when sorting all simultaneously recorded channels during a seizure by the timing of transition to the large amplitude spike-and-wave event phase, a raster plot of all spikes with units sorted in the same order produced a similar sequence of mid-seizure firing time cessations (Fig. 1c&d). Thus, FS cell cessation is correlated with a dramatic increase in the very local intensity of seizures.

Given changing waveform shapes and noise characteristics during seizures(Merricks et al., 2015), an important methodological question arises of how separable clusters in waveform feature space are from each other and from noise to allow valid unit assignments during this period. To quantitatively assess this isolation quality of feature space clusters over the course of seizures, we employed a modified version of the L_{ratio} metric of cluster separation introduced and validated by Schmitzer-Torbert et al. (2005)[58] (see Methods). Cluster divisions with L_{ratio} less than 0.1 are considered to have

a significantly low level of false negative contamination, indicating that drops in firing rate are not caused by over-assigning candidate spikes to noise or other clusters due to changing waveform shapes in these divisions. We consider units whose average contamination level across seizure divisions (dynamic L_{ratio}) is less than 0.1 to be a best-isolated subset[58]. Figure 2 shows an example of an FS unit whose waveform shape could be well isolated from noise across the entire seizure despite showing a monotonic decrease in spike amplitude (Fig. 2a-c). The isolation quality of this unit throughout the seizure is demonstrated visually by 2D voltage histograms of these waveforms (Fig. 2d) and is quantitatively captured by its dynamic L_{ratio} being far below threshold in all seizure divisions in which it was active (Fig. 2b). This isolation quality was similarly sustainable throughout the seizure for many RS units (e.g. Extended Data Fig. 5), although at a lower proportion than FS units, with 48.6% of FS units meeting this criterion but only 19.8% of RS units. This pattern sustained throughout seizures, with the proportion of well-isolated FS units remaining between 30% and 48% across all 8 seizure divisions and that of RS units remaining between 13% and 19% (Extended Data Fig. 6). The apparent difference in sortability by cell type may be because the frequency content of noise is such that random threshold crossings are more similar in shape and amplitude to the wider waveforms of RS units than to the sharper waveforms of FS units. This suggests that FS cell spikes are inherently more distinguishable from noise in human neocortical recordings even during seizures. We considered the best-isolated subset of units following this quantitative criterion in parallel with all-inclusive analyses of firing rate dynamics in various time divisions of seizures with similar results. In particular, similar temporal profiles by cell type were observed throughout seizures when

considering all units or only best-sorted units with an average $L_{ratio} < 0.1$ across all divisions for Patient C (Fig. 2e&f), as well as when comparing average firing rate time courses by cell type across all patients (Fig. 2g&h). Furthermore, the observed time difference between mean RS activity cessation timing and mean FS activity cessation timing remained significantly larger than that expected by random cell-type label reshuffling when considering all units ($p<0.0001$; Fig. 2i), as well as only best-isolated units with maximum $L_{ratio} < 0.1$ ($p<0.005$; Fig. 2j). Thus, FS cell cessation occurs several seconds before RS cell cessation across the population as well as for the very best isolated units.

The firing profile of individual FS cells and the accompanying changes in the seizure LFP amplitude were remarkably consistent across all secondary generalized focal seizures examined, independent of etiology or focus (Figs. 1, 2, and Extended Data Figs. 2-4). In patients with an etiology of mesial temporal sclerosis, where the seizure started focally in the hippocampus or surrounding medial temporal regions, FS cells in the temporal neocortex consistently stopped firing after the seizure secondarily generalized and spread to the neocortex, leading to accompanying increases in seizure LFP amplitude (Fig. 1a&b). Similarly, in a patient with an etiology of neocortical dysplasia (Patient C) where the seizure originated in the temporal neocortex, several cm from the implanted electrode array, FS cells near the array stopped firing within the first 40 seconds of the seizure spreading to that location (Fig. 2a&b). Again, this coincided with a transition to even larger amplitude spike-wave LFP events.

The variability in FS cessation times raises the question of how seizure waves travel across the neocortex: is there a wave that slowly moves across the cortex(Schevon et al., 2012) or a series of faster waves that are perhaps altered by the local activity of FS cells (Chagnac-Amitai & Connors, 1989; Connors et al., 2001; Sabolek et al., 2012)? We found fast traveling LFP waves in all patients that swept across the 4x4 mm microelectrode array within 40 ms, at a speed of ~0.1 m/s, consistent with estimates from slice and computational studies (Chervin et al., 1988; Connors et al., 2001; Golomb & Amitai, 1997). There was a dramatic effect of individual FS cell activity: when an FS cell was still firing, it was able to impede and alter epileptic traveling waves (Fig. 3a; Supplementary Video 1), preventing the wave from increasing the seizure's LFP amplitude in the vicinity of the FS cell. Once the FS cell activity ceased, traveling waves swept through the entire array, successfully recruiting the area around the now-silent FS cell (Figure 3b; Supplementary Video 1). Indeed, once all FS cells had switched off, the path of epileptic traveling waves became far more regular and stereotyped. Thus, human FS inhibitory cells possess a remarkable capability to obstruct and alter the path of epileptic traveling waves. This again points to the importance of FS activity in controlling local neuronal activity and LFP dynamics during local seizure propagation but leaves open the question of what is causing them to stop firing during the seizure.

There are two ways in which FS cells can stop firing during a seizure: 1) they could be hyperpolarized by inhibition from other inhibitory neurons (Xu et al., 2013), also known as the disinhibition hypothesis (Buckmaster et al., 2000); or 2) they could enter depolarization block and thus become incapable of firing additional action potentials,

despite receiving strong excitatory synaptic input (Cammarota et al., 2013; Karlócai et al., 2014; Ziburkus et al., 2006). These two scenarios produce very different predictions for how the action potential (AP) amplitude of an FS cell should change during a seizure. In the case of hyperpolarization, the AP amplitude should increase as the firing rate is decreasing. In the case of depolarization block, AP amplitude should decrease before the cell stops firing while its firing rate is also decreasing. To monitor the relative contributions of hyperpolarization and excessive depolarization throughout the seizure in each recorded unit, we therefore devised a novel method that decodes the membrane potential regime of neurons from extracellular spike amplitude data by computing the sign of the correlation between AP amplitude and firing rate in each second of the seizure (Fig. 4a-c; see Methods). Some units first paused their firing due to transient inhibition from other cells, as suggested by strongly negative correlations between AP amplitude and firing rate as firing rate initially decreased (Fig. 4b&h; Extended Data Figs. 7&8). This period corresponded precisely to the time period of increased firing in neighboring FS units (Fig. 4d&j). However, these apparently hyperpolarized units resumed their firing after this pause. Cessation of firing subsequently occurred presumably due to massive depolarization of their membrane potential, as demonstrated by strongly positive correlations of AP amplitude and firing rate as these units stopped firing spikes (Fig. 4b&h). The regimes of negative correlation correspond to a dynamic inhibitory control of local firing rates during the seizure, followed by a regime of positive correlation with decreasing AP amplitudes during the final descent in firing rate, a pattern consistent with what is seen during depolarization block.

This pattern was also seen on the population level in spiking event-triggered averages of the time course of our predicted membrane potential measure (Fig. 4e). Aligning inferred membrane potential time courses around the time of firing rate pauses (dropping below 30% of peak rate) revealed a large negative deflection for FS cells, indicative of these units being inhibited via hyperpolarization to reduce firing rate at this time (Fig. 4e; n=12; $R_{mean,pause}$=-0.44±0.19 [sem]; less than 0 with $p<10^{-7}$ by bootstrap mean resampling test, n_{sample}=10, $N_{bootstrap}$=50,000). Furthermore, the inferred membrane potential amongst the FS cell population showed that this shift was also widespread (Fig. 4f), with 9 out of 12 (75%) FS units pausing during the negative, hyperpolarized regime during this rate-based event. Aligning inferred membrane potential time courses around the later time of firing rate cessation in units (defined by rate falling below 30% of peak rate for the final time) revealed a large positive deflection for FS cells, indicative of these units entering a regime depolarization block (Fig. 4e; n=26; $R_{mean,cess}$=+0.45±0.12 [sem]; greater than 0 with $p<10^{-7}$ by bootstrap mean resampling test, n_{sample}=20, $N_{bootstrap}$=50,000). Again, the inferred membrane potential amongst the FS cell population showed that this shift was also widespread across units (Fig. 4f), with 20 out of 26 (77%) FS units landing in the positive, over-excited regime. When comparing these values only in units that showed both a pause and cessation to control of heterogeneity amongst different units, the inferred membrane potential was still significantly higher as the unit ceased firing compared to as the unit paused its firing (right-sided Wilcoxon signed rank test; n=12, p=0.0049). Finally, these firing rate descents in FS cell activity were associated with distinct changes in LFP amplitude

despite being of the same magnitude (at 30% of peak firing rate) as shown by event-triggered averages in LFP amplitude (Fig. 4e). FS cessation was associated with a larger LFP amplitude than that associated with pausing even amongst cells exhibiting both events (right-sided Wilcoxon signed rank test; n=12, $p<10^{-4}$). Similar results were obtained indicative of significant and widespread overexcitation underlying the cessation of activity in RS units, with 225 out of 331 (68%) RS units with sufficient rate at the time of cessation exhibiting a positive value (Extended Data Fig. 7e; n=331; $R_{mean,cess}$=0.30±0.03 [sem]; greater than 0 with $p<10^{-7}$ by bootstrap mean resampling test, n_{sample}=20, $N_{bootstrap}$=50,000). However, amongst RS cells exhibiting a pause in activity, membrane potential appeared much more heterogenous despite controlling for firing rate at this time, appearing in a bimodal distribution amongst both inhibition and depolarization block that was not significantly different from 0 (Extended Data Fig. 7e&f; n=130; $R_{mean,cess}$=-0.08±0.06 [sem]; greater than 0 with p=0.3782, n_{sample}=10, $N_{bootstrap}$=50,000). This may be because RS cells receive a greater diversity of input magnitudes during seizure progression than do FS cells but succumb to the same, more uniform mechanism underlying depolarization block at firing rate cessation and seizure transition, which we hypothesize is due to increasing potassium concentrations in the extracellular environment shared by all of these cells.

This sequence of significant hyperpolarization in FS cells followed by large and widespread overexcitation in all cells suggests a consistent membrane potential-based mechanism by which local cortical circuits fight but ultimately succumb to seizure progression. The dynamics in firing rate and action potential amplitude that characterize

this mechanism were accurately reproduced in a computational model of the cell membrane incorporating voltage-dependent sodium and potassium conductances (Hodgkin-Huxley formalism) with stochastic background synaptic input. The model reproduced all of the observed mutual dynamics between action potential rate and amplitude during inhibitory (hyperpolarizing) pauses versus depolarization-induced cessation (Fig. 5), confirming the plausibility of this mechanistic sequence driving unit activity patterns during seizure progression.

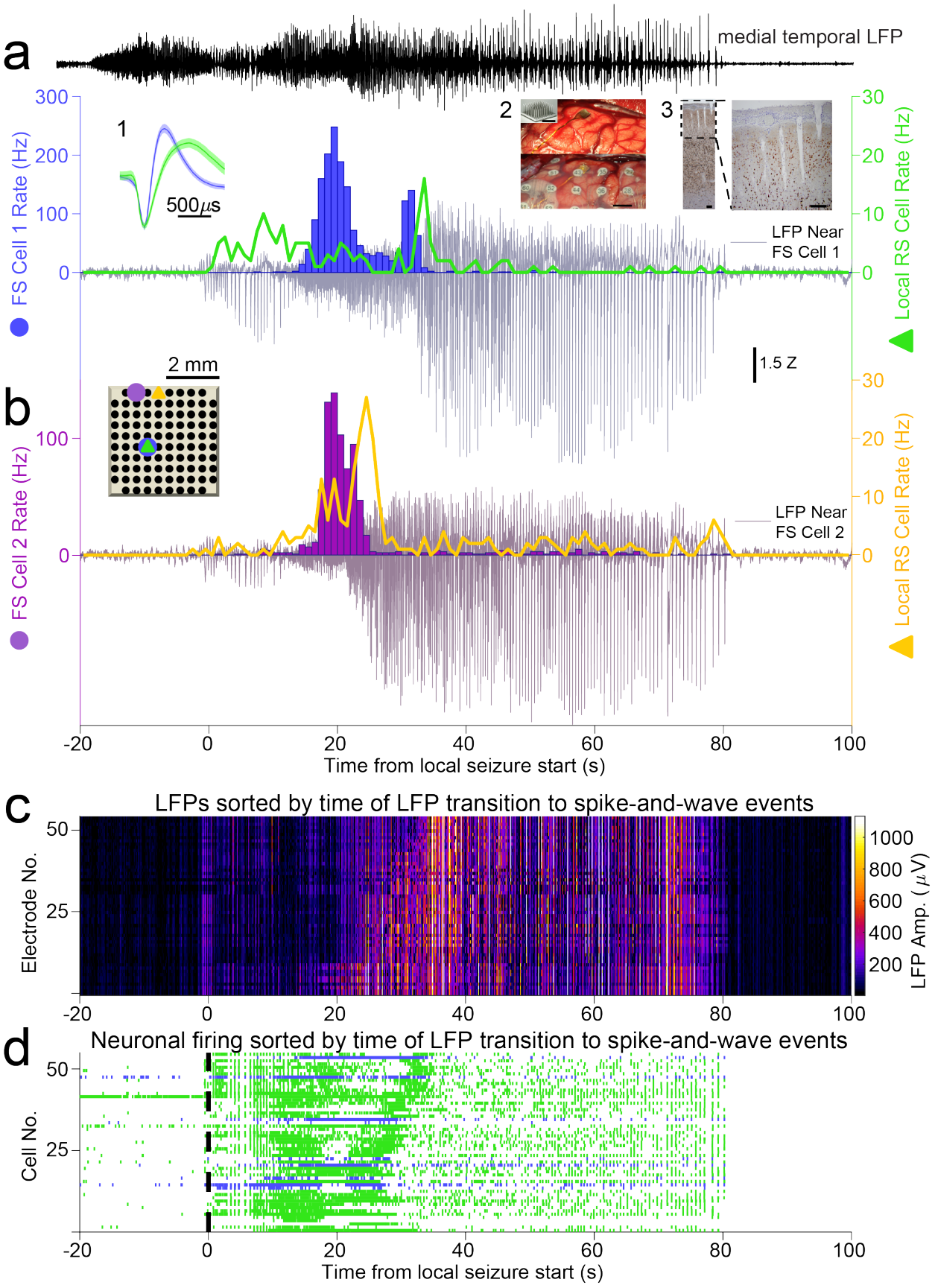
a
medial temporal LFP
1
500μs
2
3
FS Cell 1 Rate (Hz)
Local RS Cell Rate (Hz)
LFP Near FS Cell 1
1.5 Z
b
2 mm
FS Cell 2 Rate (Hz)
Local RS Cell Rate (Hz)
LFP Near FS Cell 2
Time from local seizure start (s)
c
LFPs sorted by time of LFP transition to spike-and-wave events
Electrode No.
LFP Amp. (μV)
d
Neuronal firing sorted by time of LFP transition to spike-and-wave events
Cell No.
Time from local seizure start (s)

Figure 3-1: Human neocortical inhibitory and excitatory neurons have different temporal profiles relative to secondarily generalized focal seizure progression on local electrodes

a. ***Upper.*** Electrocorticogram trace (ECoG, black) from contact closest to source of focal seizure in hippocampus of Patient A. Note its time of initiation at T = -20 seconds, substantially preceding the start of the seizure in neocortex. ***Lower.*** The firing rate of a single FS cell (blue), the firing rate of a single RS cell recorded from the same electrode (green) and the local field potential (LFP, gray, recorded from the same electrode as the FS cell) during a seizure recorded from Patient A. Note the decrease in LFP amplitude as the FS cell starts firing, followed by a dramatic increase in LFP seizure amplitude after the FS cell decreases its rate at T=35 seconds. RS cell quickly increases its firing rate as the seizure first spreads to the NeuroPort array (T=0 seconds), then decreases in rate slightly as the FS cell switches on, and finally settles into a lower firing rate regime during the large spike-and-wave events that dominates the remainder of the seizure after FS cell cessation. Inset shows the mean normalized extracellular action potential waveforms (with 99% confidence intervals in lighter shading) of FS Cell 1 (blue) and the neighboring RS cell (green). Inset 1: the mean normalized extracellular action potential waveforms (with 99% confidence intervals in lighter shading) of FS Cell 1 (blue) and the neighboring RS cell (green). Inset 2: The implanted microelectrode array (Top) with overlaid clinical grid electrodes (Bottom); Scale bar: 1 cm. Top left corner shows the array before implantation. Scale bar: 200 μm. Inset 3: Histology of resected tissue showing the NeuN-stained neurons in the full neocortical column and electrode tracts and an enlarged image (Right) showing that the array targeted layer 3 of the neocortex. Scale bars: 400 μm.

b. The inset shows a schematic of the array and the location of two simultaneously recorded FS cells separated by ~2 mm: FS Cell 1 (blue, firing rate shown in Fig. **1c**) and FS Cell 2 (purple). FS Cell 2 approached cessation at T=24 seconds, well before FS Cell 1. The LFP (grayish-purple) recorded at the same location as FS Cell 2 dramatically increases at the same time as FS Cell 2 decreases firing, well before the increase seen in the LFP recorded next to FS Cell 1. These suggest the activity of FS cells during human seizures is strongly correlated to the local intensity of seizure waves. FS Cell 2 activity cessation again precedes a sharp increase in local RS cell activity (gold), further suggesting an important role of FS cells in controlling local activity during seizure progression.

c. Heatmap shows local LFP amplitude (absolute value) over time on each electrode in NeuroPort array exhibiting classifiable units as each row, sorted by time of start of spike-and-wave event and with brighter colors indicating larger amplitudes. Note the increasing delay to start of spike-and-wave event suggesting different dynamics to seizure spread across the array over the timecourse of approximately 20 seconds.

d. Raster plot showing spike times of all cells on NeuroPort array in Patient A that could be classified into FS (blue) or RS (green) categories with rows sorted by the same order as in (C). Note the increasing delay to reduction in spike density corresponding to LFP transition to spike-and-wave events suggesting control of local seizure progression by local cellular spiking activity.

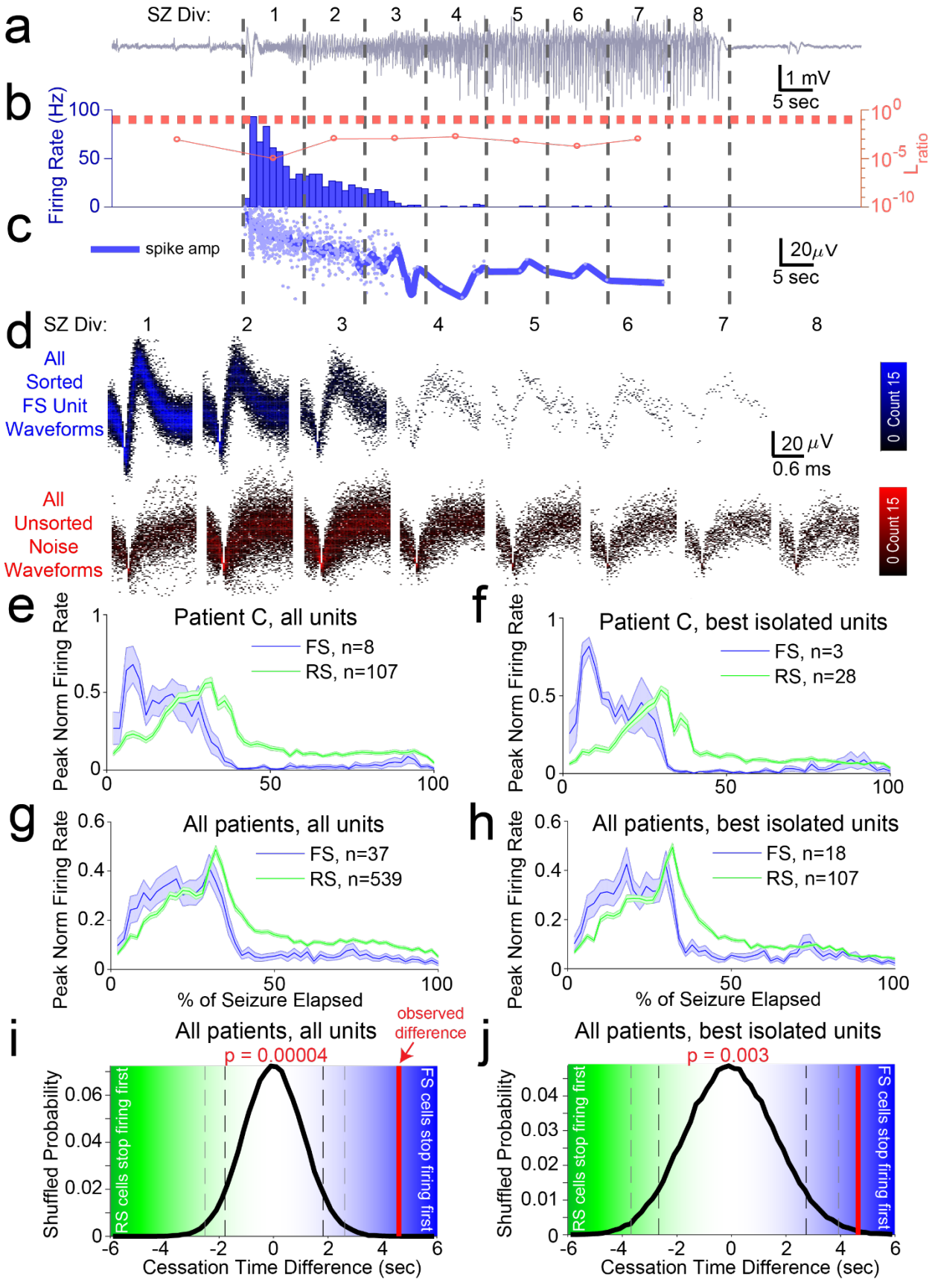
a
SZ Div: 1 2 3 4 5 6 7 8
1 mV
5 sec
b
Firing Rate (Hz)
100
50
0
10^{0}
10^{-5}
10^{-10}
L_{ratio}
c
spike amp
20μV
5 sec
d
SZ Div: 1 2 3 4 5 6 7 8
All Sorted FS Unit Waveforms
20 μV
0.6 ms
0 Count 15
All Unsorted Noise Waveforms
0 Count 15
e
Patient C, all units
FS, n=8
RS, n=107
Peak Norm Firing Rate
f
Patient C, best isolated units
FS, n=3
RS, n=28
Peak Norm Firing Rate
g
All patients, all units
FS, n=37
RS, n=539
Peak Norm Firing Rate
% of Seizure Elapsed
h
All patients, best isolated units
FS, n=18
RS, n=107
Peak Norm Firing Rate
% of Seizure Elapsed
i
All patients, all units
observed difference
p = 0.00004
RS cells stop firing first
FS cells stop firing first
Shuffled Probability
Cessation Time Difference (sec)
j
All patients, best isolated units
p = 0.003
RS cells stop firing first
FS cells stop firing first
Shuffled Probability
Cessation Time Difference (sec)

Figure 3-2: Analyzing unit subpopulations by isolation quality demonstrates consistent cell-type specific activity profiles and cessation order despite changing unit amplitude and noise structure.

a. LFP in Patient C indicating seizure as split into 8 equal time divisions for analysis of unit isolation quality across duration of seizure.

b. Bar graph shows firing rate in 1 second bins of best-isolated example FS unit (blue) in Patient C. Dotted red line indicates threshold used to determine best-isolated units using the dynamic L_{ratio} measure (see Methods) in each time division of seizure. Line plot indicates dynamic L_{ratio} in each division (red) and shows large separation of example FS unit from noise in feature space used for clustering throughout the seizure (note log scale).

c. Line plot showing average spike amplitude (dark blue) and individual spike amplitudes (light blue) of example FS unit over course of seizure in Patient C. Note that even as amplitude decreases the unit remains well-isolated from noise as quantified by dynamic L_{ratio} across seizure.

d. Time-voltage histogram of all threshold crossings assigned to this example FS unit (blue, *Upper)* and to noise (red, *Lower*) in eight divisions of seizure in Patient C. Shows unit waveforms are visually distinguishable from threshold crossings assigned as noise across seizure.

e. Average firing rate traces across seizures for each cell type group in Patient C, with y-axis normalized to firing rate peak and x-axis normalized to total seizure duration before averaging. Note right-shifted rate profile of RS units over course of seizure as compared to FS units.

f. Average firing rate traces across seizures for each cell type group using only best-isolated units (see Methods) in Patient C, with y-axis normalized to firing rate peak and x-axis normalized to total seizure duration before averaging. Note right-shifted rate profile of best-isolated RS units over course of seizure as compared to best-isolated FS units.

g. Average firing rate traces across seizures for each cell type group across all patients, with y-axis normalized to firing rate peak and x-axis normalized to total seizure duration before averaging. Note right-shifted rate profile of RS units over course of seizure as compared to FS units.

h. Average firing rate traces across seizures for each cell type group using only best-isolated units (see Methods) across all patients, with y-axis normalized to firing rate peak and x-axis normalized to total seizure duration before averaging. Note right-shifted rate profile of best-isolated RS-classified units over course of seizure as compared to best-isolated FS-classified units.

i. Observed time difference (solid red line) between mean RS activity cessation timing (n=399) and mean FS activity cessation timing (n=37) in relation to probability distribution of this timing difference across random label reshufflings of unit cell type labels ($N_{shuffles}$=100,000; solid black line). P-value indicates probability of observing a value equal to or more extreme than the observed value simply by random assignment of cell type to each unit. Values on the right half correspond to a positive difference between RS and FS cessation, with larger values associated with increasing certainty that FS cells stop firing before RS cells. Values on the left half correspond to a negative difference between RS and FS cessation times, with larger values associated with increasing certainty that RS cells stop firing before FS cells.

j. Observed time difference (solid red line) between mean best-isolated RS activity cessation timing (n=83; Lratio < 0.1 during middle 3 seizure divisions) and mean best-isolated FS activity cessation timing (n=17; Lratio < 0.1 during middle 3 seizure divisions) in relation to probability distribution of this timing difference across random label reshufflings of unit cell type labels ($N_{shuffles}$=100,000; solid black line). P-value indicates probability of observing a value equal to or more extreme than the observed value simply by random assignment of cell type to each unit.

Values on the right half correspond to a positive difference between best-isolated RS and best-isolated FS cessation times, with larger values associated with increasing certainty that best-isolated FS cells stop firing before best-isolated RS cells. Values on the left half correspond to a negative difference between best-isolated RS and best-isolated FS cessation, with larger values associated with increasing certainty that best-isolated RS cells stop firing before best-isolated FS cells.

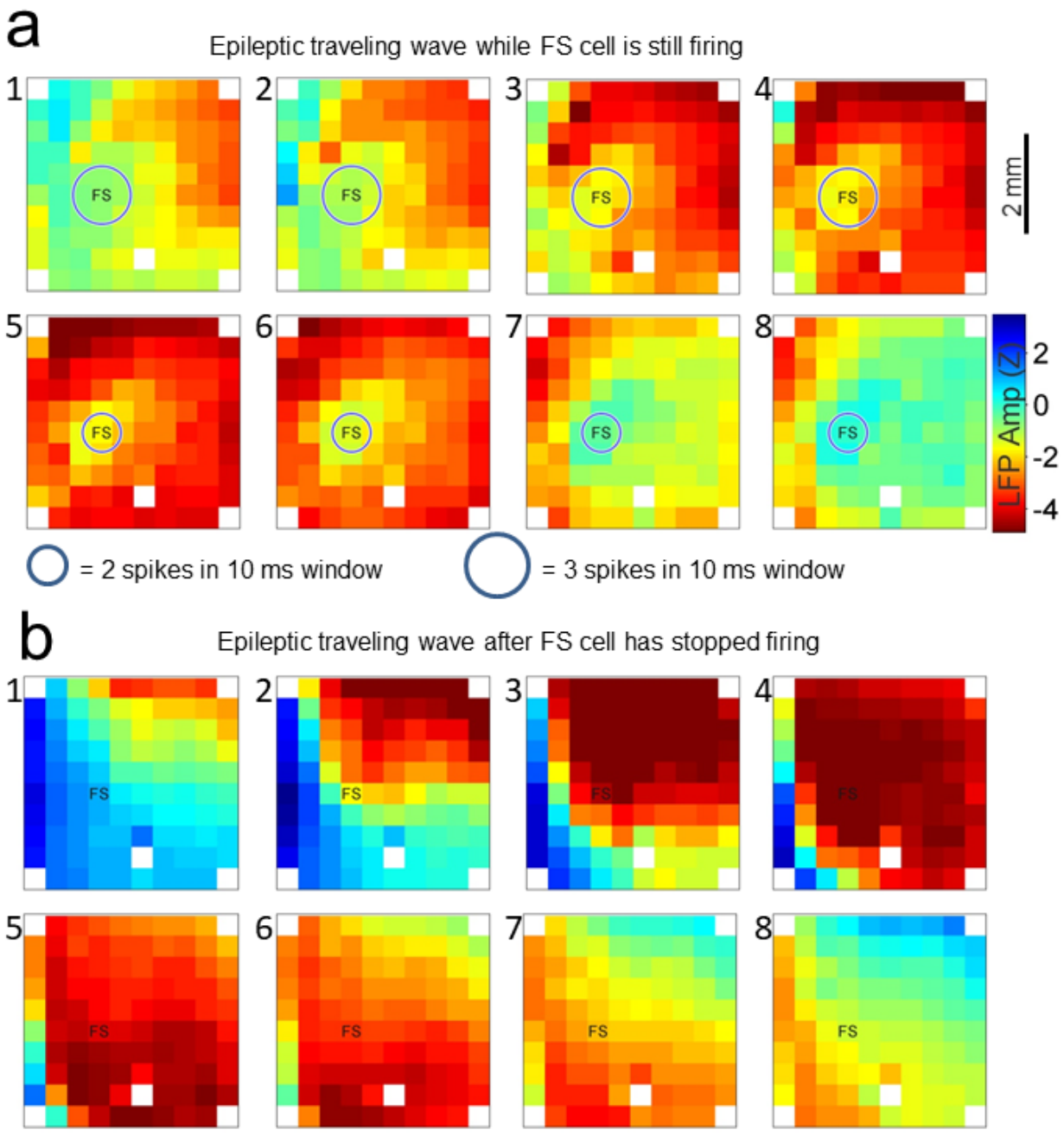

Figure 3-3: Fast-spiking inhibitory neurons, when still firing, impede the spread of epileptic

traveling waves.

a. An example of a traveling wave recorded 30 seconds after the start of a seizure in Patient A. The FS cell located at the position marked “FS” was firing at high rates at this time. The 8 snapshots (1-8) are taken over a 35 ms interval as the traveling LFP wave starts in the top-right corner of the array and travels across the array. The traveling wave does not fully invade the region of neocortex containing the active FS cell, resulting in lower amplitude LFPs around the FS cell. In each subfigure, each square denotes a single LFP sensor, and white squares indicate omitted sensors.

b. An example of a traveling wave recorded 49 seconds after the start of the same seizure. In the absence of FS cell firing, the epileptic traveling wave moves unimpeded through the array, fully invading the region around the marked FS cell and resulting in larger amplitude LFPs at all locations.

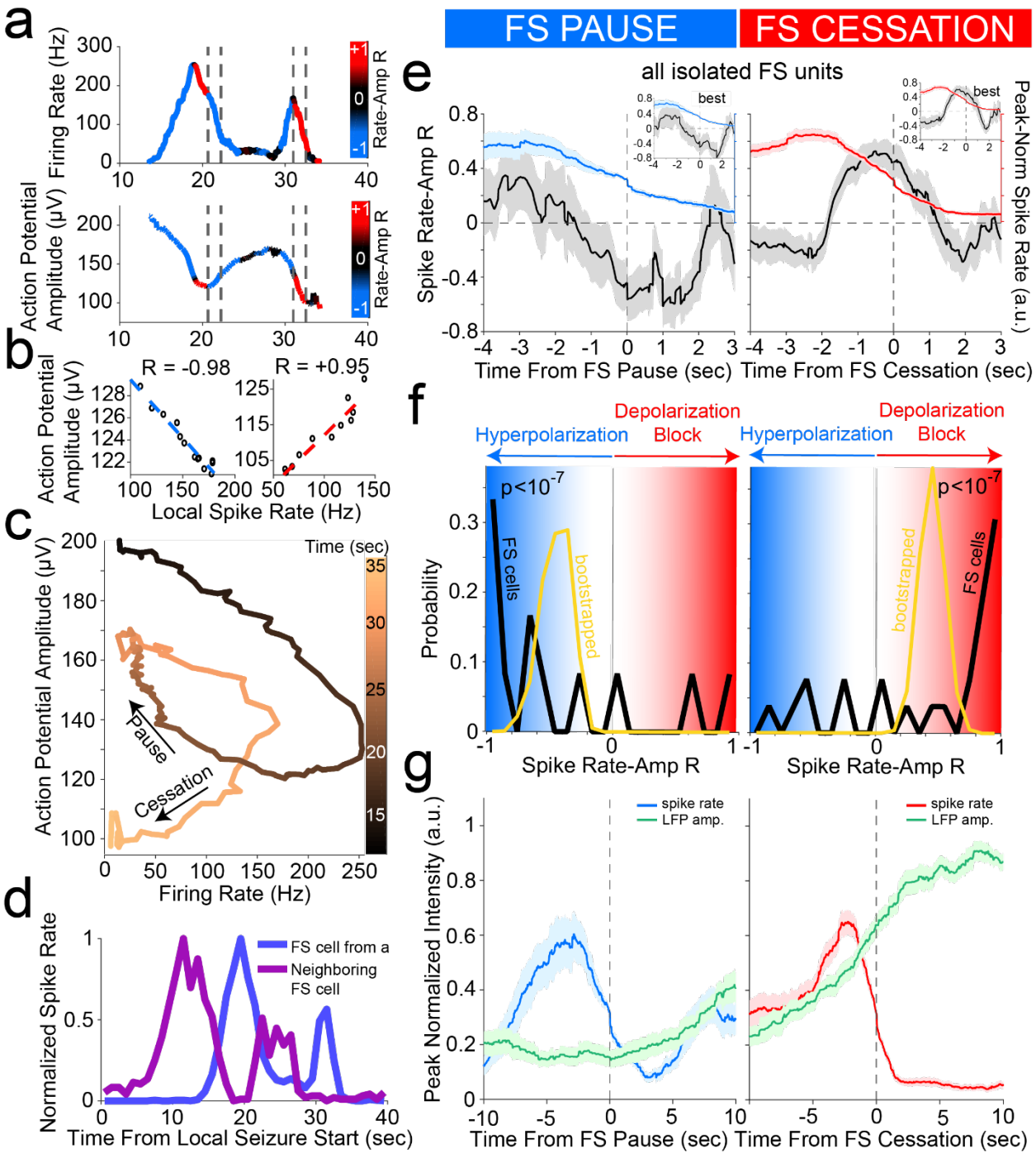

Figure 3-4. Cessation of individual FS unit activity is consistently associated with inferred membrane potential signatures of depolarization block, despite prior hyperpolarized pauses

a. Firing rate *(upper)* and trough-to-peak spike amplitude (*lower*) of example FS unit in Patient A, color-coded by the local correlation between spike rate and amplitude (in 1 second time bins) as an extracellular proxy for membrane potential trajectory and subthreshold input history. Dotted lines indicate starts and ends of two time periods of firing rate suppression characterized by

different membrane potential signatures further characterized in (B), namely a negative correlation regime corresponding to inhibition followed by a positive correlation regime corresponding to over-excitation ending in firing rate cessation putatively though depolarization block.

b. Example of negative correlation (*left*) between local spike rate and amplitude in first time period indicated by dotted lines in (A) and example of positive correlation (*right*) between local spike rate and amplitude in second time period indicated by dotted lines in (A). Least squares linear fit indicated in dotted lines following color scheme in (A) with Pearson's correlation coefficient indicated above each plot.

c. Trajectory of unit activity over time during seizure in local spike rate vs spike amplitude space, with increasing time indicated by increasingly lighter copper color. The first time period of firing rate reduction in dotted lines in (A) is indicated with an arrow as "Pause" and the second time period of firing rate reduction in dotted lines in (A) is indicated with an arrow as "Cessation."

d. Firing rate of unit from (A) with neighboring FS unit firing rate overlaid, giving further evidence that first period of firing rate suppression corresponds to inhibition from local FS units while second period of firing rate suppression does not correspond to inhibition from local FS units.

e. Unit cessation-triggered population average of the time course of novel membrane potential regime measure, i.e. the correlation coefficient relating spiking amplitude and rate in a local time window, around the two significant descents in firing rate (below 30% of peak rate) that occur in sequence during seizure. These are designated as pause (*left panel*) and cessation (*right panel*). Left panel shows population average firing rate (blue) and inferred membrane potential regime (black) aligned according to the time of pause in each unit, for all FS units displaying a pause (n=14), with inset showing average for best-isolated FS units displaying a pause (n=10). Right panel shows population average firing rate (red) and inferred membrane potential regime (black) aligned according to the cessation time of each unit, for all FS units (n=37), with inset showing average for best-isolated FS units (n=24).

f. Probability distribution of membrane potential regime measure (spike rate-amplitude correlation; black line) at the time of pause (*left panel*) for FS unit pausing subpopulation (n=14) with sample mean distribution (gold line; resampling size n=10, $N_{bootstrap}$=50,000) showing the mean correlation to be significantly below zero, i.e. in the hyperpolarized membrane potential regime (blue). In combination with its declining firing rate, this is indicative of widespread inhibition across this subpopulation at the time of pause. The population distribution of inferred membrane potential regime is also shown at the time of cessation (*right panel*) for the full FS unit population (n=37) with sample mean distribution (gold line; resampling size n=10, $N_{bootstrap}$=50,000) showing the mean correlation to be significantly above zero, i.e. in the highly depolarized membrane potential regime (red). This is indicative of widespread depolarization block occurring across FS population at the time of cessation.

g. Unit cessation-triggered population average of the time course of same-electrode LFP amplitude around unit activity pause (*left panel*) and cessation (*right panel*). In particular, left panel shows population average firing rate (blue) and LFP amplitude (black) aligned according to the time of pause in each unit, for all FS units displaying a pause (n=14). Right panel shows population average firing rate (red) and LFP amplitude (black) aligned according to the time of cessation in each unit, for all FS units (n=37), indicative of larger LFP increase associated with second FS firing rate descent (cessation) than with first (pause) despite comparable local firing rates in the two conditions.

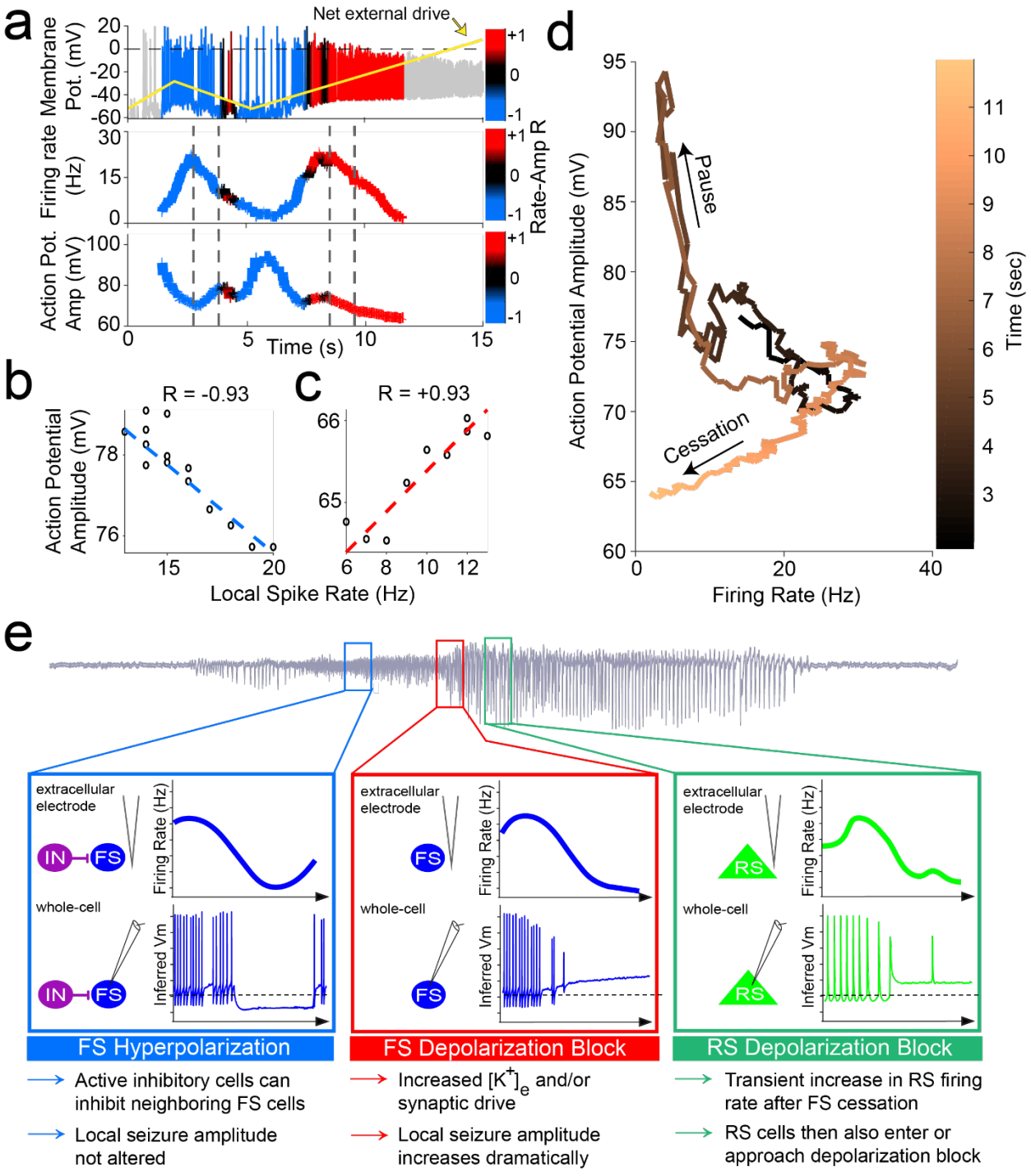

Figure 3-5. Mechanistic model of unit dynamics across seizure progression: inhibition followed by over-excitation in conductance-based neuron model reproduces key features of extracellular unit behavior during seizures.

a. Simulated membrane potential in conductance-based spiking model color-coded by the local correlation between spike rate and amplitude and with net excitatory input indicated by gold line *(upper panel)*. Shows what is hypothesized to be happening within cortical cells during seizure progression as inferred from extracellular spike shape and rate dynamics. Firing rate *(middle panel)* and trough-to-peak spike amplitude (*lower panel*) of the same model, color-coded by the local correlation between spike rate and amplitude as an extracellular proxy for membrane potential and subthreshold input history. Dotted lines indicate starts and ends of two time periods of firing rate suppression characterized by different membrane potential signatures further characterized in (b) and (c).

b. Example of negative correlation between local spike rate and amplitude during firing pause in (a), corresponding to activity shutdown via inhibition. Least squares linear fit indicated in dotted lines following color scheme in (a) with Pearson's correlation coefficient indicated above plot.

c. Example of positive correlation between local spike rate and amplitude during firing cessation, corresponding to activity shutdown via over-excitation. Least squares linear fit indicated in dotted lines following color scheme in (a) with Pearson's correlation coefficient indicated above plot.

d. Trajectory of unit activity over time during seizure in local spike rate vs spike amplitude space, with increasing time indicated by increasingly lighter copper color. The first time period of firing rate reduction in (a) is indicated with an arrow as "Pause" and the second time period of firing rate reduction is indicated with an arrow as "Cessation."'

e. Summary of observed dynamics in cell-type specific firing rate and inferred membrane potential trajectories.
Blue box: Following seizure onset, some FS cells can stop firing for brief periods (as observed on extracellular electrodes, upper panel). This pause in firing is coupled with signs of hyperpolarization in the inferred membrane potential (lower panel).
Red box: As the seizure starts to transition to a dramatically higher amplitude FS cells stop firing (as observed on extracellular electrodes, upper panel). This cessation is coupled with signs of excessive depolarization in the inferred membrane potential (lower panel; resting membrane potential indicated as dashed line). This is likely due to elevated extracellular potassium ion concentrations by this point of the seizure or increased synaptic drive.
Green box: The subsequent stage of high amplitude spike-and-wave rhythms corresponds to a transient increase and then decrease of firing rate amongst RS cells (as observed on extracellular electrodes, upper panel). This decrease in firing rate is coupled with signs of excessive depolarization in the inferred membrane potential (lower panel).

3.4 Discussion

We have shown that both FS and RS cells are strongly activated during the initial spread of secondarily generalized seizures. The immediate increase in RS rate at seizure onset, in particular, clearly indicates spread of the seizure, and not a failed seizure in what has been called an ictal penumbra, where no initial increases in RS rate appear(Schevon et al., 2012). Importantly, we have shown that both FS and RS cells can sometimes pause their activity due to hyperpolarization (likely due to inhibition-mediated hyperpolarization from other nearby inhibitory neurons) but stop firing midway through secondarily generalized seizures due to depolarization block. This result is independent of seizure etiology (cortical dysplasia vs. mesial temporal sclerosis) or site of origin (hippocampus vs. neocortex). This suggests that there is an almost complete lack of FS-mediated inhibition towards the end of a human seizure, in contrast to some animal models without loss of inhibition (Neumann et al., 2017). FS cells are active near the beginning and middle of the seizure, in contrast to computational models placing the loss of inhibitory restraint at seizure onset (Liou et al., 2020). Strikingly, this absence of FS inhibitory activity is accompanied by large increases in the amplitude of the seizure's LFP and unimpeded fast traveling waves, as well as a short-lasting increase in RS firing. Thus, these results suggest a more complicated set of dynamics than a monotonic increase or decrease of inhibition and provide further insight into the associated biophysical mechanisms.

The main difference between RS and FS cell firing during the seizures observed here was the significantly earlier cessation of spiking by FS cells, which is consistent with previous results from *in vitro* models of seizure-like events showing increased propensity of FS cells to enter depolarization block compared to pyramidal cells (Cammarota et al., 2013; Karlócai et al., 2014; Ziburkus et al., 2006). The reason for this difference in propensity to enter depolarization block has not been established, but these results suggest this difference could represent a primary source of imbalance between excitatory and inhibitory cell activities that allows seizures to propagate and transition to a large amplitude phase in human neocortex. One hypothesis accounting for this difference is that of the differential expression of voltage-gated potassium channel units in FS as opposed to RS cells (Lien & Jonas, 2003; Martina et al., 1998; Rudy & McBain, 2001) in combination with the elevated extracellular potassium ion levels known to occur in the context of seizures (Fröhlich et al., 2008; Somjen, 2004). However, there are several intrinsic and network-based properties that are known to differ between FS cells and pyramidal cells and could contribute to this difference, such as intrinsic excitability and the relative strength of feedforward drive (Cruikshank et al., 2007; Kawaguchi, 1995; Markram et al., 2004; Pouille & Scanziani, 2004). The results here suggest that properties responsible for increasing the propensity of FS cells to enter depolarization block relative to RS cells are also those that allow the propagation and exacerbation of seizures in human neocortex. Beyond seizure progression, it is also possible that the lack of FS activity sets in motion a critical network-level transition that leads to seizure termination (Beverlin et al., 2012; Fröhlich et al., 2010; Kramer et al.,

2012). This transition may include the activation of inhibitory cell types other than FS cells (Cammarota et al., 2013).

In summary, FS cells are the largest source of inhibition in the neocortex, and human FS cells approach cessation less than halfway through a seizure, most likely due to depolarization block. This is associated with a dramatic increase of the seizure's local field potential amplitude and a transition to clear spike-and-wave events at a frequency of ~3 Hz. Rhythmic spike-and-wave discharges, when they occur in the motor cortex, are responsible for the rhythmic ~3 Hz movements seen during the clonic phase of tonic-clonic seizures (Blumenfeld, 2005). Importantly, this suggests a novel, FS-dependent, mechanistic explanation for the two behaviorally defined phases of secondarily generalized tonic-clonic seizures: the high-FS-rate, low-LFP-amplitude phase of the seizure corresponds to the tonic phase, whereas the post-FS-cessation phase with periodic spike-wave bursts corresponds to a longer lasting clonic phase. Thus, in addition to existing approaches (Berényi et al., 2012; Krook-Magnuson et al., 2013; Paz et al., 2013; Sukhotinsky et al., 2013; Wykes et al., 2012), novel therapies that prevent FS cells from entering depolarization block may prevent - or at least limit the severity of - seizures, representing a novel and potentially powerful avenue for treating seizures with many different etiologies.

3.5 Materials and Methods

3.5.1 Patients & Clinical/Research Electrode Placement

Approval for all experiments was granted by the Institutional Review Boards of Massachusetts General Hospital / Brigham & Women's Hospital and Rhode Island Hospital. The decision to implant intracranial electrodes in an epilepsy patient as well the positioning of those electrodes in a patient was made solely on clinical factors by clinical staff. The explicit goal of this study was to examine the single neuron correlates of tonic-clonic seizures (Fröhlich et al., 2008) with focal onsets (also referred to as focal seizures with secondary generalization), one of the most common kind of epilepsies (Annegers, 2001). These focal seizures have a localized onset zone, either in the mesial temporal lobe or neocortex, but secondarily generalize, spreading to both hemispheres and almost always leading to impaired consciousness. Here, we studied data from 4 patients (Patients A,B,C,D) with clear focal seizures with secondary generalization, with each of these clinical seizures showing clear spike-and-wave patterns. Two additional patients with temporal-lobe epilepsy were implanted with NeuroPort Arrays but not studied here because one of them did not have any seizures while implanted (Patient E), and the NeuroPort Array in the other patient did not sample any typical spike-and-wave seizures (Patient F). A total of 10 secondarily generalized seizures with spike-and-wave discharges from the 4 patients were analyzed (3 each from Patients A and D; 2 each from Patients B and C). A detailed clinical description of each of these 4 patients follows:

Patient A. Patient A was a left-handed man in his 30s at the time of his surgery. He had suffered from pharmacologically intractable partial complex seizures for almost two decades. His seizures lasted 1-2 minutes and were characterized by a sudden onset of

slurred and nonsensical speech. This was followed by a staring spell, lack of responsiveness, and head turning to the right. He also displayed automatisms and posturing that involved his right arm and hand more than his left. MRI suggested left (dominant) temporal polymicrogyria. He underwent placement of grids and strips for ~2 weeks to delineate the seizure focus with respect to this area of abnormal sulcation. A 4x4 mm NeuroPort array with 1.5 mm long contacts was placed in the left superior temporal gyrus. Seizures were found to emanate from the mesial temporal structures, but during secondary generalization, the seizures spread to the location of the array in the superior temporal gyrus and beyond. The patient underwent a left temporal lobectomy, and histology confirmed that the microarray targeted layer 3. Pathology was consistent with mesial temporal sclerosis.

Patient B. Patient B was a right-handed man in his 40s at the time of his surgery, with a history of medically refractory epilepsy. His seizures lasted 1-2 minutes. Clinically, the seizures started with arousal and bilateral arm and leg extension. This was followed by leftward head deviation, left arm flexion, and generalized tonic-clonic activity. He underwent placement of grids, strips, and depths in his right hemisphere. A 4x4 mm NeuroPort array (with 1.5 mm deep contacts) was placed in the right middle temporal gyrus. During secondary generalization, the seizures spread to the location of the NeuroPort array in the middle temporal gyrus and beyond. The patient underwent a right temporal lobectomy. Histology on the resected tissue confirmed that the microarray targeted layer 3.

Patient C. Patient C was a left-handed woman in her 20s at the time of her surgery. She started to have complex partial seizures at least 10 years prior to surgery. These seizures included an aura of nausea and a 'tunneling' sensation, then a flattening of affect, slowed responsiveness, automatisms, and associated amnesia. Such seizures occurred 3-4 times per month and were persistent despite being on a three-drug anticonvulsant regimen. MRI revealed an extensive nodular gray matter heterotopia in the right hemisphere. Video-EEG monitoring had found right hemispheric onset seizures, and fMRI had shown normal left sided language activation patterns and normal motor activation patterns. Wada testing confirmed left hemispheric language dominance and suggested her left hemisphere could adequately support memory function subsequent to a right temporal lobectomy. Based on these data, she was implanted with a combination of subdural grid and strip electrodes over the right hemisphere and 3 depth electrodes into the right temporal lobe. The NeuroPort array (with 1.5 mm deep contacts) was placed in the right middle temporal gyrus. Her seizures lasted between 1-2.5 minutes. These showed very consistent patterns of seizure onset and propagation on ECoG; all began in the right middle and upper gyri of the posterior temporal cortex. Low amplitude and fast activity were recorded from these grid sites at the onset, followed by a buildup of 11-13 Hz activities from these leads which then spread anteriorly and inferiorly along the grid. Rhythmic spike-wave discharges were also detected soon after seizure onset spreading to several locations, including the location of the NeuroPort array in the right middle temporal gyrus. The patient underwent an extensive right temporal resection with extension posteriorly toward the right temporo-occipital junction but sparing of much of the mesial temporal

structures (including the hippocampus). Histology confirmed that the array targeted layers 2/3. Pathology revealed subtle neuronal dysgenesis and focal superficial gliosis and encephalomalacia in the posterior temporal neocortex, including the recorded seizure-onset zone. Anterior temporal cortex showed mild gliosis.

Patient D. Patient D was a right-handed man in his 20s whose seizures began when he was a teenager. His seizures were characterized by a blank stare and oral automatisms accompanied by stiffening and posturing of the right hand. His MRI was unremarkable, but his semiology and phase I EEG recordings suggested a left temporal seizure onset. Consequently, he was implanted with several strip electrodes covering the left frontal and temporal regions. The NeuroPort array (1.0 mm deep contacts) was placed in the middle temporal gyrus about 1–2 cm posterior to the temporal tip. All of the seizures had similar clinical and electrographic signatures with a left gaze preference at onset followed by tonic and then clonic movements of the right arm. Electrographically, the seizures began with a generalized burst of sharp waves followed by sharp wave complexes that were maximal in mesial temporal leads. The participant underwent a left temporal lobectomy. Histological examination of the tissue revealed mild dysplastic changes in the lateral temporal neocortex and gliosis and moderate neuronal loss in regions CA4 and CA3 of the hippocampus.

3.5.2 NeuroPort Recordings, Data Collection & Analysis

A Neuroport array (manufactured by Blackrock Microsystems) is a 10x10 grid of electrodes with an inter-electrode spacing of 400 um, giving a total size of 4x4 mm. The

depth of the electrodes used in this study was either 1.5 mm (Patients A,B,C) or 1.0 mm (Patient D). 96 of the 100 electrodes were used to record the activity of individual neurons as well as the local field potential (LFP). The 0.3-7500 Hz wideband analog signal from each electrode was referenced to a distant intracranial reference wire and sampled at 30 kHz. The LFP shown in Figs. 1, 2, and Extended Data Fig. 1 were z-scored, but not filtered any further. Traveling wave analysis, videos (Supplementary Video 1), and images (Fig. 3) made use of these z-scored, unfiltered LFP signals. For single unit analysis, the broadband signal was high-pass filtered above 250 Hz using a 6-pole Bessel filter and then manually spike-sorted using Plexon Offline Sorter. We then classified the neurons as either fast-spiking (FS) inhibitory interneurons or regular-spiking (RS) excitatory cells using well-established criteria(Cardin et al., 2009; Nowak et al., 2003), including action potential shape. Cessation of firing during a seizure was defined as the bin after which the firing rate never exceeded 30% of the unit's peak rate. For action-potential (AP) amplitude analysis (Fig. 4a), the AP amplitude was defined as the trough-to-peak amplitude of each individual extracellular action potential.

3.5.3 Cluster isolation quality assessment: Dynamic L_{Ratio}

To assess the isolation quality of feature space clusters over the course of seizures, we employed a modified version of the L_{ratio} metric of cluster separation introduced and validated by Schmitzer-Torbert et al. (2005)[58]. This involved first calculating the Mahalanobis distance of every spike to a given cluster's center in a 4D feature space consisting of trough-to-peak amplitude, trough-to-peak width, principal component 1, and principal component 2. The Mahalanobis distance normalizes the Euclidean

distance by the variance of a given cluster along its major dimensions to correct for correlations amongst features. Schmitzer-Torbert et al. (2005)[58] showed strong error rate correlation with ground truth extracellular spikes by assuming a multi-dimensional Gaussian distribution for a given cluster and taking the amount of contamination by false negative assignments to be the sum of probabilities of each un-clustered spike of a given Mahalanobis distance to belong to that Gaussian, which was robust to the particular feature space used. These probabilities are given by the inverse of the cumulative distribution function of a chi-squared distribution with degrees of freedom equal to the number of features in the features space, the sum of which is called L. Because clusters in this space moved over the course of the seizure in a non-monotonic pattern here, we calculated Mahalanobis distances to a surrogate cluster for multiple subsets of the whole cluster at 8 equal divisions over the course of the seizure and 3 divisions of the 10 minute period that occurred two minutes after the end of the seizure. A composite cluster across initial divisions was used to provide a liberal estimate of the space that a given cluster might occupy despite early waveform shape changes. This composite reference cluster included all available spikes before the seizure along with those in the first two divisions of the seizure, which were generally well-sortable. We calculated the sum of false negative assignment probabilities under a Gaussian model for this reference cluster, the value L, for each seizure and post-seizure division. We then dynamically normalized L by the number of spikes assigned to the cluster in each time division to estimate contamination rates relative to the number of spikes assigned during that division, which we refer to as the dynamic L_{ratio}.

3.5.4 Membrane potential trajectory analysis

We exploited the biophysical relationship between depolarization, voltage-gated Na+ channel inactivation, and spike waveform shape (de Polavieja, 2005) to infer the direction of membrane potential changes underlying the changes in firing rate exhibited by single units recorded extracellularly in patients across time. This was done for a given unit by first computing the local spike rate and average trough-to-peak waveform amplitude in moving time windows of width 1 second unless otherwise specified, moving with a step size of 0.1 seconds. Then a linear regression was performed at each point in this series across a moving time window of 3 seconds, producing a time series of correlation coefficients for bins with an average spike rate of at least 5 Hz. Strong negative correlations were taken as evidence of firing rate changes associated with membrane potential changes near resting membrane potential, while strong positive correlations were taken as evidence of membrane potential changes closer to firing threshold, near the regime of depolarization block (Bikson et al., 2003).

3.5.5 Computational model

Computer simulations of transmembrane voltage dynamics consistent with the extracellular observations here were made in MATLAB R2017b to explore plausible underlying biophysical mechanisms. A 4-dimensional ordinary differential equation model of a patch of neural membrane following the Hodgkin-Huxley formalism of passive (g_L=0.033 mS/cm^2, E_L=-60 mV, $I_L=g_L(V-E_L)$) and voltage-dependent spiking Na+ (g_{Na}=60.0 mS/cm^2, E_{Na}=+58 mV, $I_{Na}=g_{Na}m^3h(V-E_{Na})$) and K+ ($g_K$=5 mS/cm^2, E_K=-85

mV, $I_K=g_K n^4(V-E_K)$) conductances was solved using Euler integration with a timestep of 0.005 msec. First order kinetics of gating variables *m*, *h*, and *n* were modeled as in previously established models of this form (Hoffman et al., 1997). Slowly changing net synaptic input and extracellular ion gradient changes were considered to constitute a net external drive modeled as an injected inward current. This current follows a temporal form hypothesized to drive human neocortical neurons during secondarily generalized seizures based on the dynamic membrane potential decoding analysis performed here. Fast synaptic inputs were modeled as conductances with a maximum conductance $g_{syn}=0.15$ mS/cm^2 and an exponential decay time course of 5 milliseconds gated by input spike times generated by a Poisson process with a linearly increasing rate parameter from 0.001 to 0.2 Hz representing increasing input firing rates across seizure. Analysis of the resulting spike trains was completed in the same manner as dynamic membrane potential trajectory decoding was performed for the observed extracellular data.

3.5.6 Statistical analyses

In performing hypothesis testing on various metrics describing activity amongst FS and RS units including peak firing rate difference, mean cessation time difference, and mean correlation between spike firing rate and action potential amplitude at time of cessation, we employed bootstrap-based methods to quantify the uncertainty in these metrics. For peak firing rate and cessation time differences this involved combining all relevant unit measurements into a single population, randomly reshuffling RS and FS labels amongst this population, and recomputing the relevant difference metrics $N_{bootstrap}$ times as

indicated to generate a distribution of the metric for random unit classifications. The probability of a Type-I (false positive) error, the p-value, was then reported as the area under the distribution corresponding to values more extreme than the observed value for the original data. For testing the positivity of the mean correlation between spike firing rate and action potential amplitude at time of cessation, this involved first removing correlation coefficients in the time series corresponding to a linear regressions involving spike rates of less than 5 Hz. Then the coefficients at each unit's detected cessation time were resampled with replacement in 20 unit subpopulations 50,000 times (unless otherwise specified) and averaged to generate a bootstrapped sample mean distribution characterizing the variability in this mean relative to zero. The probability of a Type-I (false positive) error that the observed mean coefficient was greater than zero by chance, the p-value, was then reported as the area under the distribution corresponding to values equal to or less than zero. To nonparametrically test the significance of differences in paired measures at cessation and pause times within single units, we employed the right-sided Wilcoxon signed rank test (RMatlab2017b).

3.6 Acknowledgements

We would like to thank the patient volunteers. This work was supported by the American Epilepsy Society Junior Investigator Research Award, CURE Epilepsy Taking Flight Award, NINDS F32-NS083208 and University of Michigan Startup Funds (OJA), NIH R01-NS062092 (SSC) and NSF graduate student fellowships (TTJ & EKWB).

3.8 Supplemental Figures and Tables

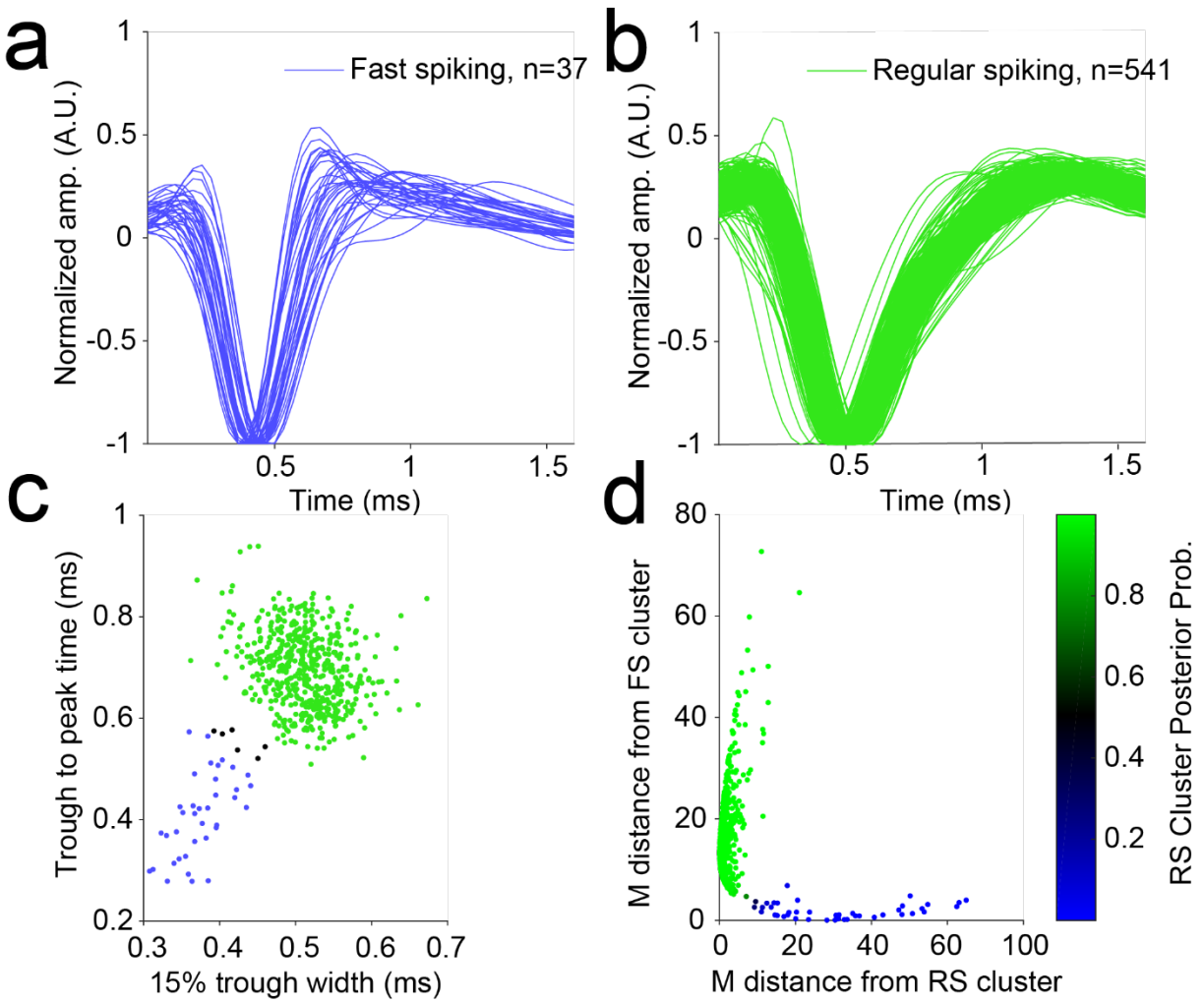

Extended Data Figure 3-1: Human neural activity classification

- **a.** Average waveform of each FS-classified unit, normalized by the value the waveform reaches at its trough. The overlaid average waveforms show visual consistency amongst all units classified as FS and as having spike widths narrower than those of RS-classified units.
- **b.** Average waveform of each RS-classified unit, normalized by the value the waveform reaches at its trough. The overlaid average waveforms show visual consistency amongst all units classified as RS and as having spike widths wider than those of FS-classified units.
- **c.** All units indicated as points in the average waveform feature space that produced optimal cluster separation, namely the width of the waveform at the potential corresponding to 15% of the potential at its trough and the time between the trough and peak of the waveform. Clustering was automated using a Gaussian Mixture Model where points with posterior probability exceeding 0.95 were assigned to the closest centroid. Black dots indicate units that did not exceed this threshold for either Gaussian cloud and were thus unclassified and not used in the remainder of the study.
- **d.** Mahalanobis distance of each unit from both the RS and FS clusters with color indicating its posterior probability of belonging to the RS cluster. Closeness of points to both axes shows that the clusters are well-separated when accounting for their different variances along different directions in feature space.

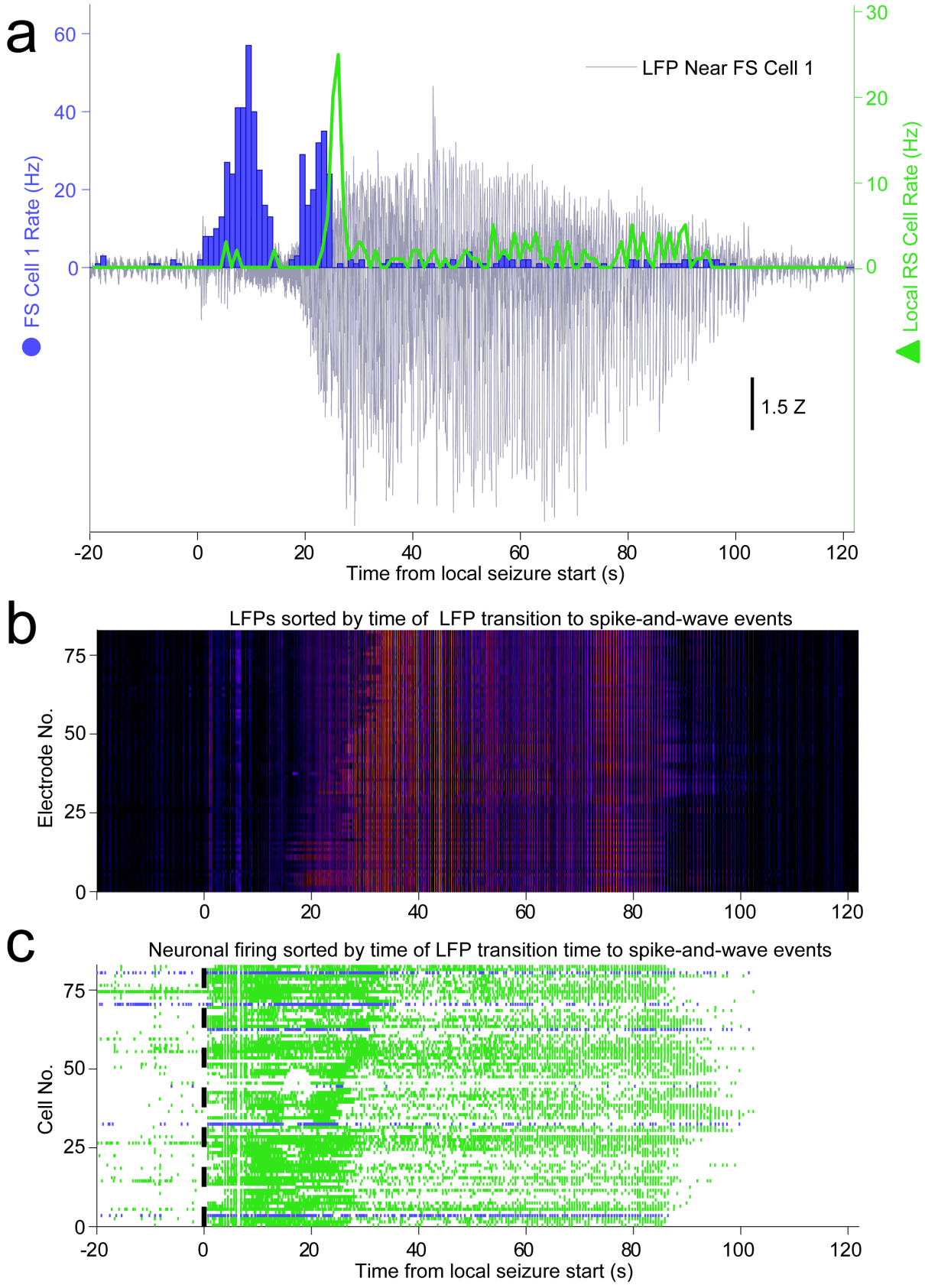
a
LFP Near FS Cell 1
FS Cell 1 Rate (Hz)
Local RS Cell Rate (Hz)
1.5 Z
Time from local seizure start (s)
b
LFPs sorted by time of LFP transition to spike-and-wave events
Electrode No.
c
Neuronal firing sorted by time of LFP transition time to spike-and-wave events
Cell No.
Time from local seizure start (s)

Extended Data Figure 3-2: Human neocortical inhibitory and excitatory neuron activities have distinct temporal profiles relative to secondarily generalized focal seizure progression on local electrodes, Patient A, Seizure 2

- **a.** The LFP (gray) recorded at the same location as FS Cell 1 (blue) dramatically increases at the same time as FS Cell 1 decreases firing. FS Cell 1 activity cessation again precedes a sharp increase in local RS cell activity (green), further suggesting an important role of FS cells in controlling local activity during seizure progression.
- **b.** Heatmap shows local LFP amplitude (absolute value) over time on each electrode in NeuroPort array exhibiting classifiable units as each row, sorted by time of start of spike-and-wave event and with brighter colors indicating larger amplitudes.
- **c.** Raster plot showing spike times of all cells on NeuroPort array in Patient B that could be classified into FS (blue) or RS (green) categories with rows sorted by the same order as in (B). Note the increasing delay to reduction in spike density corresponding to LFP transition to spike-and-wave events suggesting control of local seizure progression by local cellular spiking activity.

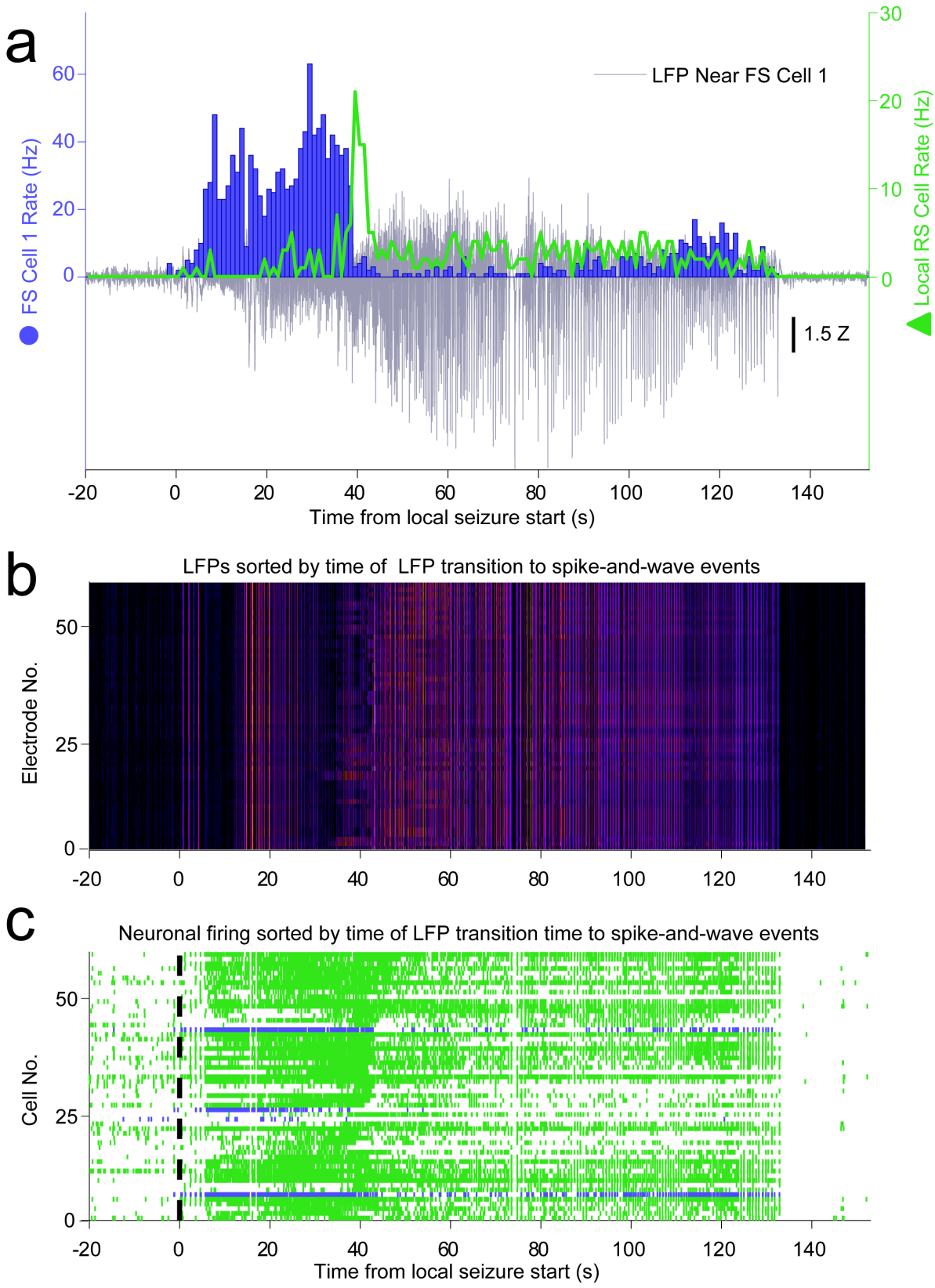

Extended Data Figure 3-3: Human neocortical inhibitory and excitatory neuron activities have

distinct temporal profiles relative to secondarily generalized focal seizure progression on local electrodes, Patient C, Seizure 2

- **a.** The LFP (gray) recorded at the same location as FS Cell 1 (blue) dramatically increases at the same time as FS Cell 1 decreases firing. FS Cell 1 activity cessation again precedes a sharp increase in local RS cell activity (green), further suggesting an important role of FS cells in controlling local activity during seizure progression.
- **b.** Heatmap shows local LFP amplitude (absolute value) over time on each electrode in NeuroPort array exhibiting classifiable units as each row, sorted by time of start of spike-and-wave event and with brighter colors indicating larger amplitudes.
- **c.** Raster plot showing spike times of all cells on NeuroPort array in Patient C that could be classified into FS (blue) or RS (green) categories with rows sorted by the same order as in (B). Note the increasing delay to reduction in spike density corresponding to LFP transition to spike-and-wave events suggesting control of local seizure progression by local cellular spiking activity.

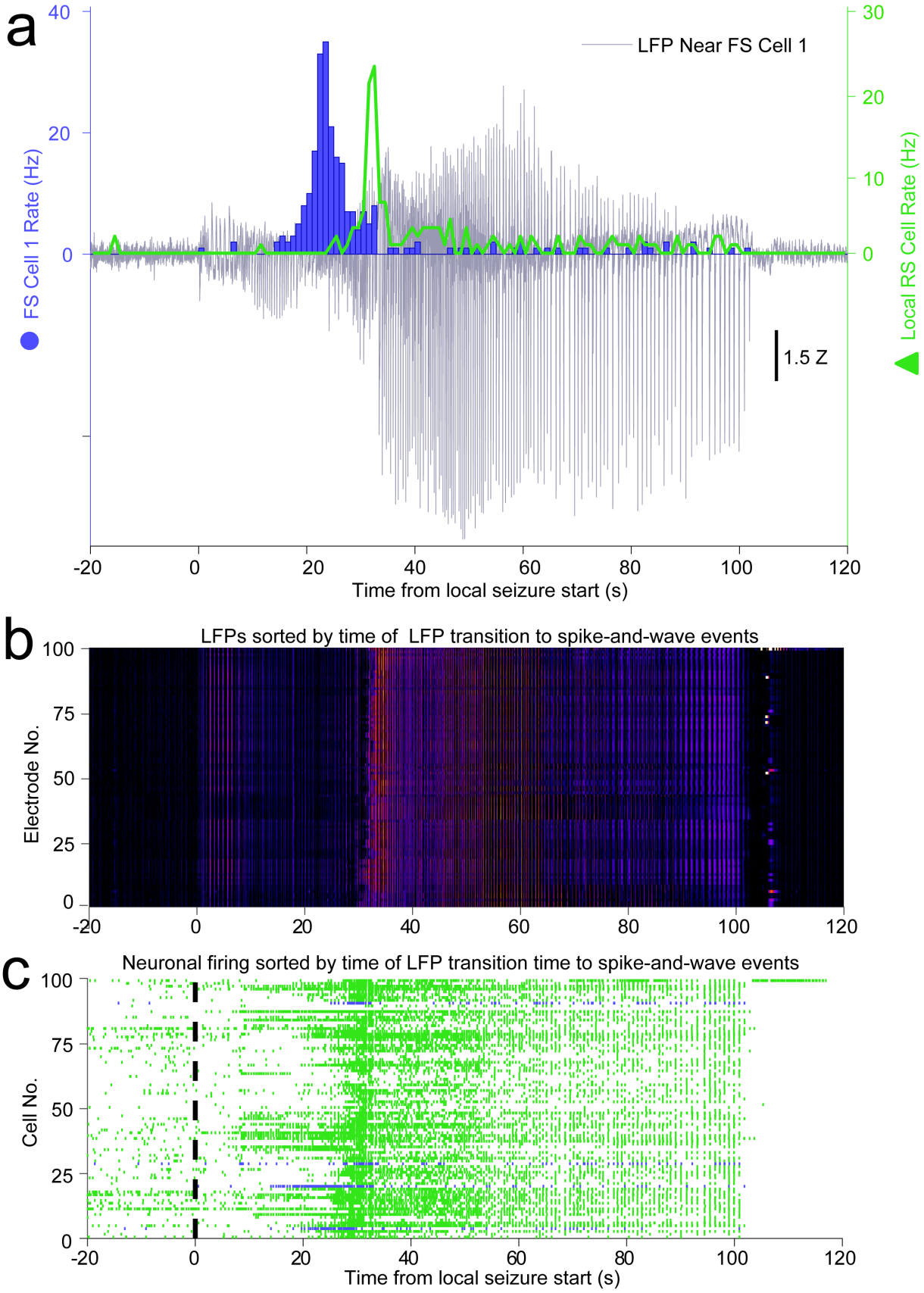
a
LFP Near FS Cell 1
FS Cell 1 Rate (Hz)
Local RS Cell Rate (Hz)
1.5 Z
Time from local seizure start (s)
b
LFPs sorted by time of LFP transition to spike-and-wave events
Electrode No.
c
Neuronal firing sorted by time of LFP transition time to spike-and-wave events
Cell No.
Time from local seizure start (s)

Extended Data Figure 3-4: Human neocortical inhibitory and excitatory neuron activities have distinct temporal profiles relative to secondarily generalized focal seizure progression on local electrodes, Patient B, Seizure 1

- **a.** The LFP (gray) recorded at the same location as FS Cell 1 (blue) dramatically increases at the same time as FS Cell 1 decreases firing. FS Cell 1 activity cessation again precedes a sharp increase in local RS cell activity (green), further suggesting an important role of FS cells in controlling local activity during seizure progression.
- **b.** Heatmap shows local LFP amplitude (absolute value) over time on each electrode in NeuroPort array exhibiting classifiable units as each row, sorted by time of start of spike-and-wave event and with brighter colors indicating larger amplitudes.
- **c.** Raster plot showing spike times of all cells on NeuroPort array in Patient C that could be classified into FS (blue) or RS (green) categories with rows sorted by the same order as in (B).

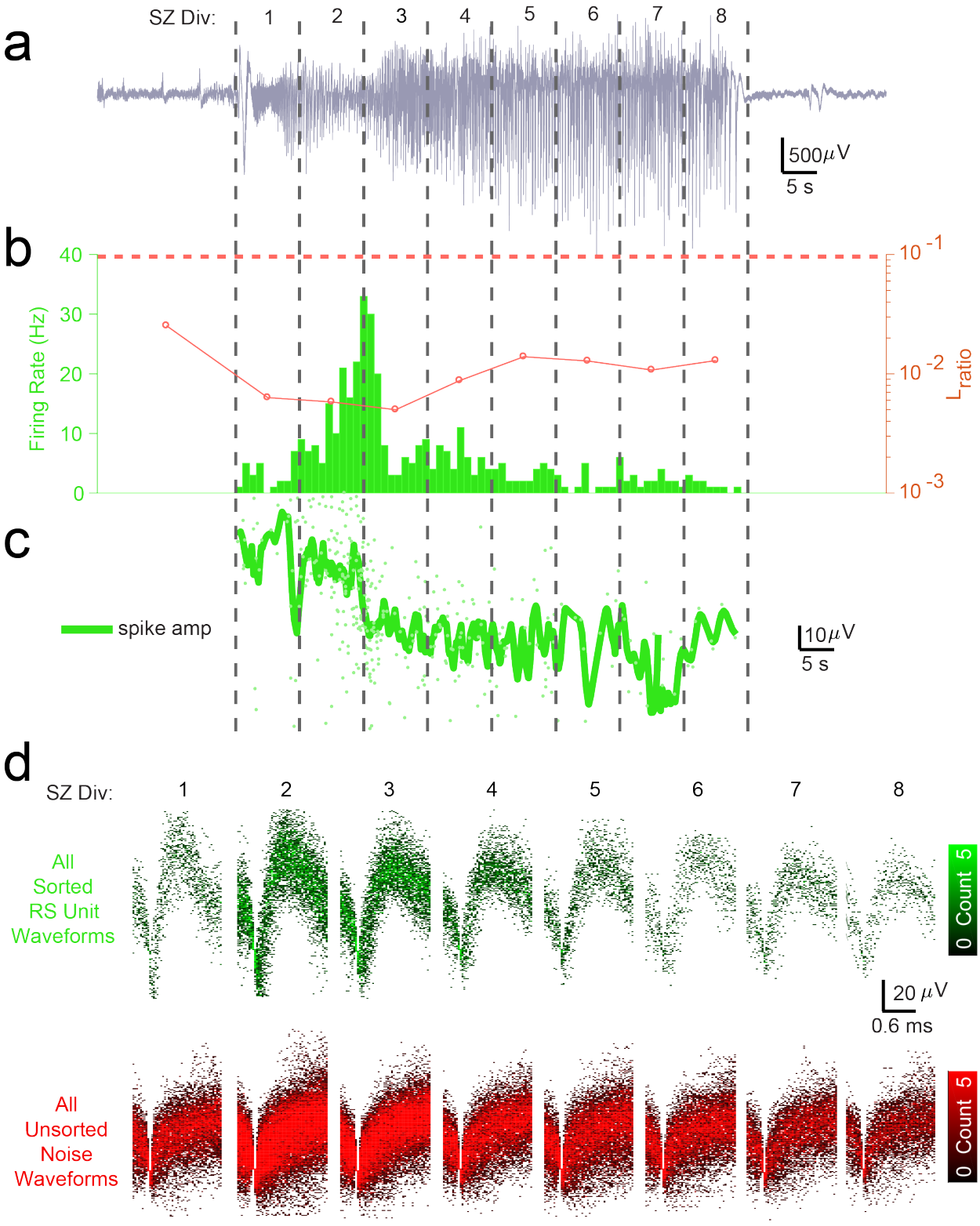

Extended Data Figure 3-5: Cluster isolation quality assessment suggests RS units are well-isolatable across seizure despite changing unit amplitude and noise structure, allowing analysis

of firing rate changes across seizure.

- **a.** LFP in Patient C indicating seizure as split into 8 equal time divisions for analysis of unit isolation quality across duration of seizure.
- **b.** Bar graph shows firing rate in 1 second bins of best-isolated example RS unit (green) in Patient C. Dotted red line indicates threshold used to determine best-isolated units using the dynamic L_{ratio} measure (see Methods) in each time division of seizure. Line plot indicates dynamic L_{ratio} in each division and shows large separation of example FS unit from noise in feature space used for clustering throughout the seizure (note log scale).
- **c.** Line plot showing average spike amplitude (dark green) and individual spike amplitudes (light green) of example RS unit over course of seizure in Patient C. Note that even as amplitude decreases the unit remains well-isolated from noise as quantified by dynamic L_{ratio} across seizure.
- **d.** Time-voltage histogram of all threshold crossings assigned to this example RS unit (green, *Upper)* and to noise (red, *Lower*) in eight divisions of seizure in Patient C. Shows unit waveforms are visually distinguishable from threshold crossings assigned as noise across seizure.

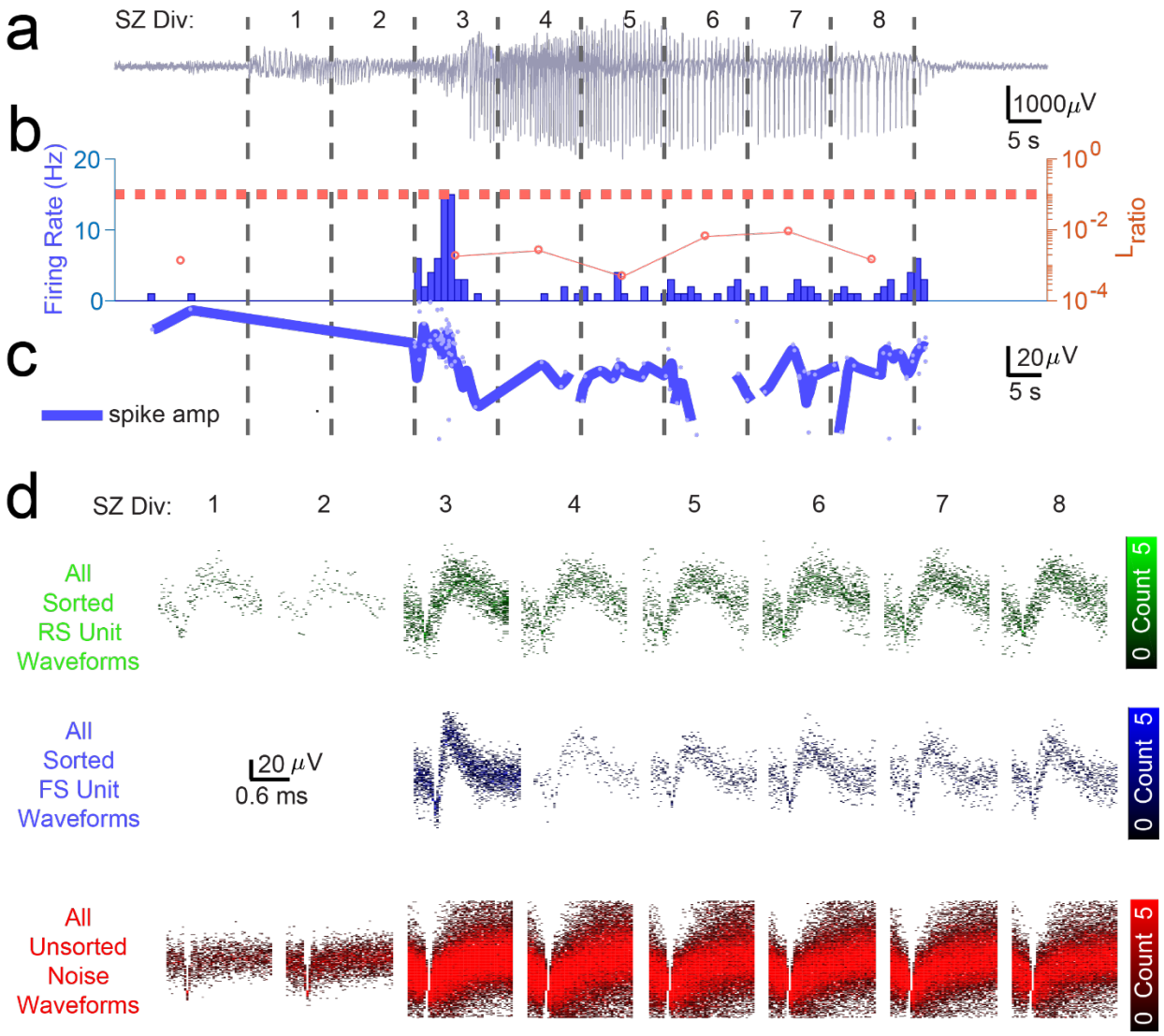
a
SZ Div:
1
2
3
4
5
6
7
8
1000μV
5 s
b
Firing Rate (Hz)
20
10
0
10^0
10^-2
10^-4
L_ratio
c
spike amp
20μV
5 s
d
SZ Div:
1
2
3
4
5
6
7
8
All Sorted RS Unit Waveforms
0 Count 5
All Sorted FS Unit Waveforms
20 μV
0.6 ms
0 Count 5
All Unsorted Noise Waveforms
0 Count 5

Extended Data Figure 3-6: Cluster isolation quality assessment suggests RS and FS units on same channel are well-isolatable across seizure despite changing unit amplitude and noise structure, allowing analysis of firing rate changes across seizure for multiple patients.

- **a.** LFP in Patient B indicating seizure as split into 8 equal time divisions for analysis of unit isolation quality across duration of seizure.
- **b.** Bar graph shows firing rate in 1 second bins of best-isolated example FS unit (blue) in Patient B. Dotted red line indicates threshold used to determine best-isolated units using the dynamic L_{ratio} measure (see Methods) in each time division of seizure. Line plot indicates dynamic L_{ratio} in each division and shows large separation of example FS unit from noise in feature space used for clustering throughout the seizure (note log scale).
- **c.** Line plot showing average spike amplitude (dark blue) and individual spike amplitudes (light blue) of example FS unit over course of seizure in Patient B. Note that even as amplitude decreases the unit remains well-isolated from noise as quantified by dynamic L_{ratio} across seizure.
- **d.** Time-voltage histogram of all threshold crossings assigned to example FS unit (blue, *Middle),* RS unit on same channel (green, *Upper*), and to noise (red, *Lower*) in eight divisions of seizure in Patient B. Shows unit waveforms are visually distinguishable from threshold crossings assigned as noise and as other units across seizure.

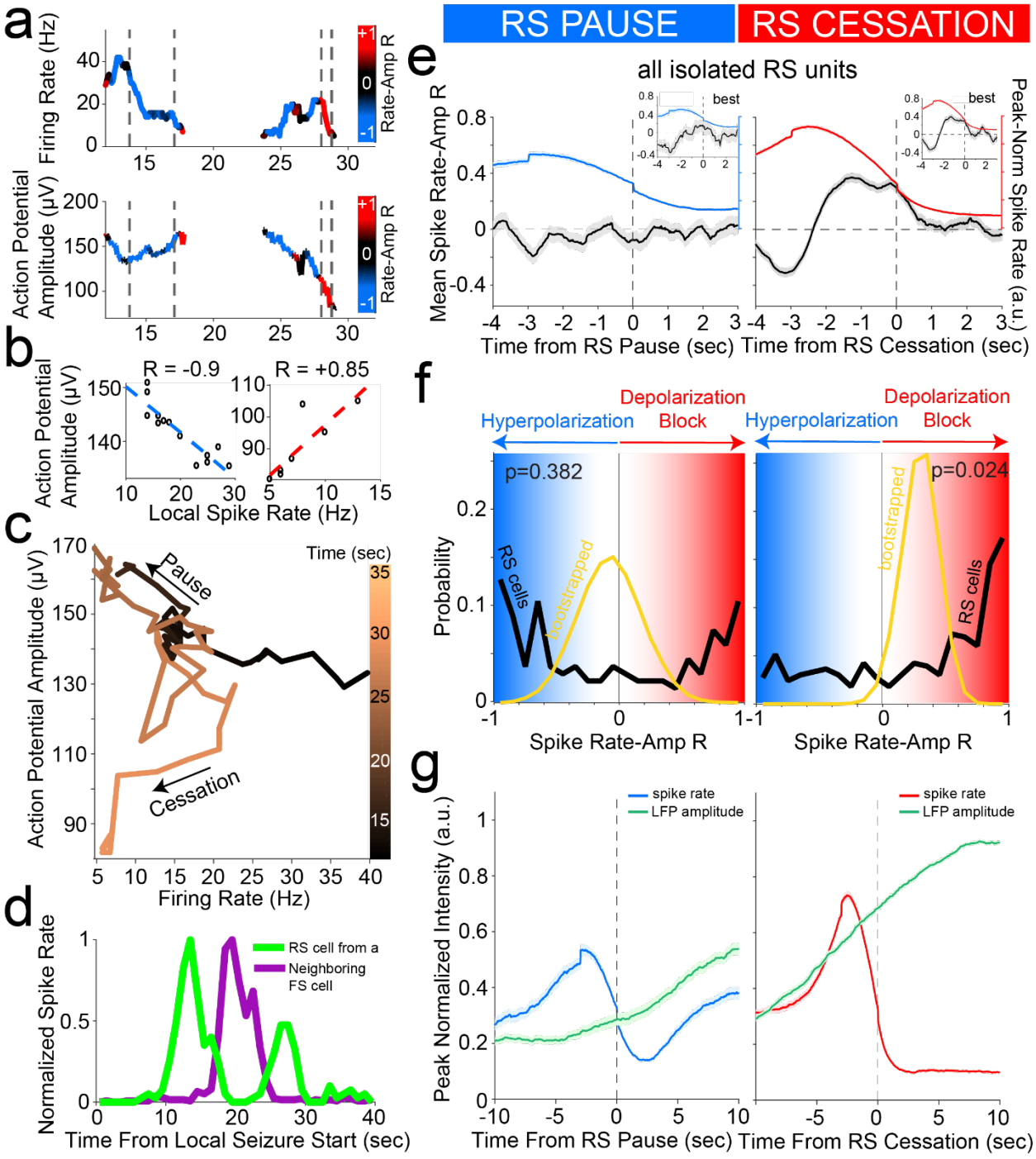

Extended Data Figure 3-7: Cessation of individual RS unit activity is consistently associated with inferred membrane potential signatures of depolarization block, despite prior pauses

a. Firing rate *(upper)* and trough-to-peak spike amplitude (*lower*) of example RS unit in Patient A, color-coded by the local correlation between spike rate and amplitude (in 1 second time bins) as an extracellular proxy for membrane potential trajectory and subthreshold input history. Dotted lines indicate starts and ends of two time periods of firing rate suppression characterized by different membrane potential signatures further characterized in (B), namely a negative

correlation regime corresponding to inhibition followed by a positive correlation regime corresponding to over-excitation ending in firing rate cessation putatively though depolarization block.

b. Example of negative correlation (*left*) between local spike rate and amplitude in first time period indicated by dotted lines in (A) and example of positive correlation (*right*) between local spike rate and amplitude in second time period indicated by dotted lines in (A). Least squares linear fit indicated in dotted lines following color scheme in (A) with Pearson's correlation coefficient indicated above each plot.

c. Trajectory of unit activity over time during seizure in local spike rate vs spike amplitude space, with increasing time indicated by increasingly lighter copper color. The first time period of firing rate reduction in dotted lines in (A) is indicated with an arrow as "Pause" and the second time period of firing rate reduction in dotted lines in (A) is indicated with an arrow as "Cessation."

d. Firing rate of unit from (A) with neighboring FS unit firing rate overlaid, giving further evidence that first period of firing rate suppression corresponds to inhibition from local FS units while second period of firing rate suppression does not correspond to inhibition from local FS units.

e. Unit cessation-triggered population average of the time course of novel membrane potential regime measure, i.e. the correlation coefficient relating spiking amplitude and rate in a local time window, around the two significant descents in firing rate (below 30% of peak rate) that occur in sequence during seizure. These are designated as pause (*left panel*) and cessation (*right panel*). Left panel shows population average firing rate (blue) and inferred membrane potential regime (black) aligned according to the time of pause in each unit, for all RS units displaying a pause (n=176), with inset showing average for best-isolated RS units displaying a pause (n=41). Right panel shows population average firing rate (red) and inferred membrane potential regime (black) aligned according to the cessation time of each unit, for all RS units meeting cessation criteria (n=379), with inset showing average for best-isolated RS units (n=111).

f. Probability distribution of membrane potential regime measure (spike rate-amplitude correlation; black line) at the time of pause (*left panel*) for RS unit pausing subpopulation (n=176) with sample mean distribution (gold line; resampling size n=10, $N_{bootstrap}$=50,000) showing a bimodal distribution of correlation coefficients near +1 and -1 , i.e. in the hyperpolarized membrane potential regime (blue) or in the highly depolarized regime (red). The population distribution of inferred membrane potential regime is also shown at the time of cessation (*right panel*) for the RS unit population meeting cessation criteria (n=379) with sample mean distribution (gold line; resampling size n=10, $N_{bootstrap}$=50,000) showing the mean correlation to be significantly above zero, i.e. in the highly depolarized membrane potential regime (red). This is indicative of widespread depolarization block occurring across RS population at the time of cessation.

g. Unit cessation-triggered population average of the time course of same-electrode LFP amplitude around unit activity pause (*left panel*) and cessation (*right panel*). In particular, left panel shows population average firing rate (blue) and LFP amplitude (black) aligned according to the time of pause in each unit, for all RS units displaying a pause (n=176). Right panel shows population average firing rate (red) and LFP amplitude (black) aligned according to the time of cessation in each unit, for all RS units (n=379).

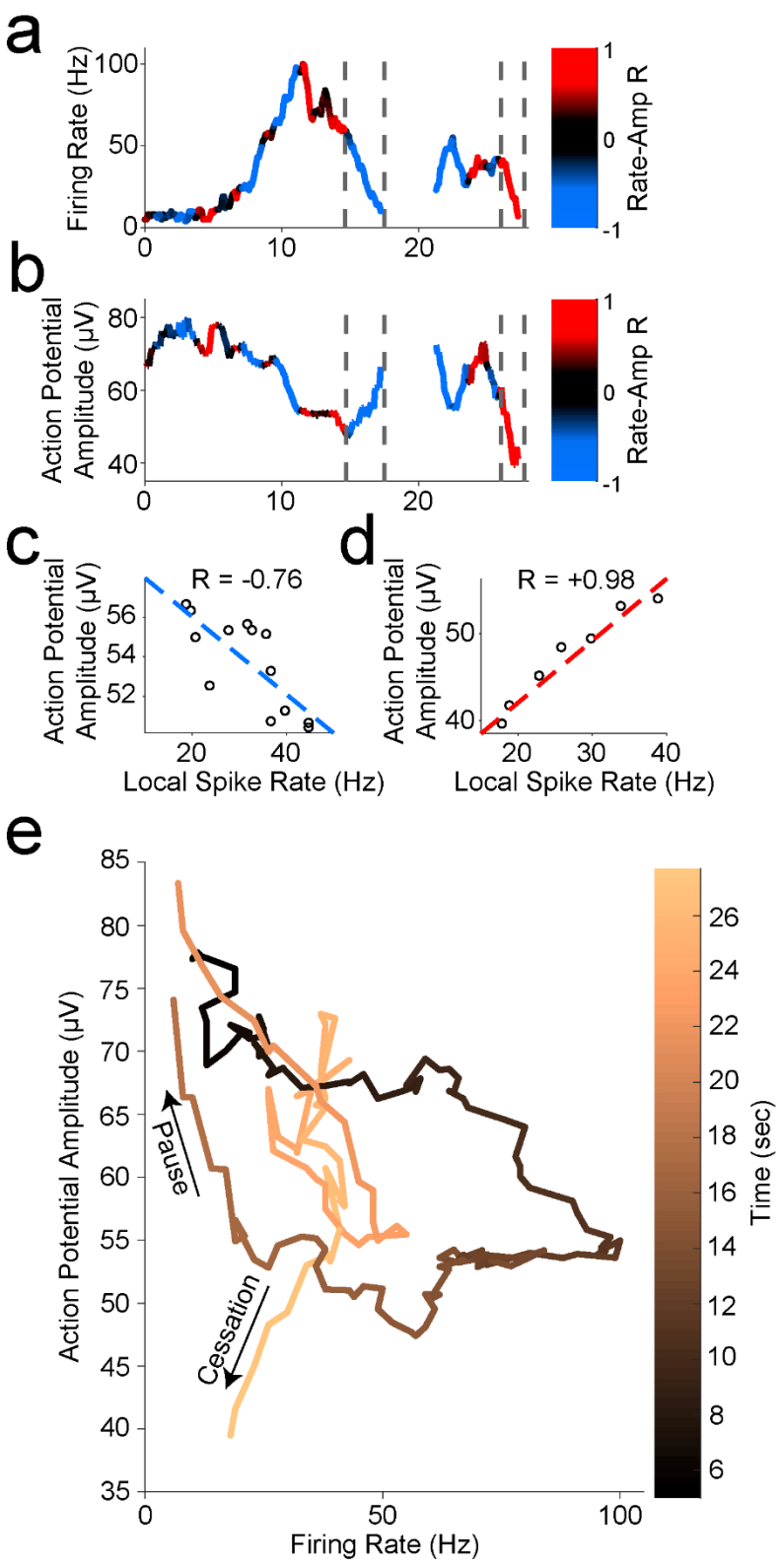

Extended Data Figure 3-8: Seizure progression is consistently associated with extracellular signs

of depolarization block preceded by inhibition in single units.

- **a.** Firing rate *(upper)* and trough-to-peak spike amplitude (*lower*) of another example FS unit in Patient A, color-coded by the local correlation between spike rate and amplitude (in 1 second time bins) as an extracellular proxy for membrane potential and subthreshold input history. Dotted lines indicate starts and ends of two time periods of firing rate suppression characterized by different membrane potential signatures further characterized in (B), namely a negative correlation regime corresponding to inhibition followed by a positive correlation regime corresponding to over-excitation ending in firing rate cessation putatively though depolarization block.
- **b.** Example of negative correlation (*left*) between local spike rate and amplitude in first time period indicated by dotted lines in (A) and example of positive correlation (*right*) between local spike rate and amplitude in second time period indicated by dotted lines in (A). Least squares linear fit indicated in dotted lines following color scheme in (A) with Pearson's correlation coefficient indicated above each plot.
- **c.** Trajectory of unit activity over time during seizure in local spike rate vs spike amplitude space, with increasing time indicated by increasingly lighter copper color. The first time period of firing rate reduction in dotted lines in (A) is indicated with an arrow as "Pause" and the second time period of firing rate reduction in dotted lines in (A) is indicated with an arrow as "Cessation."

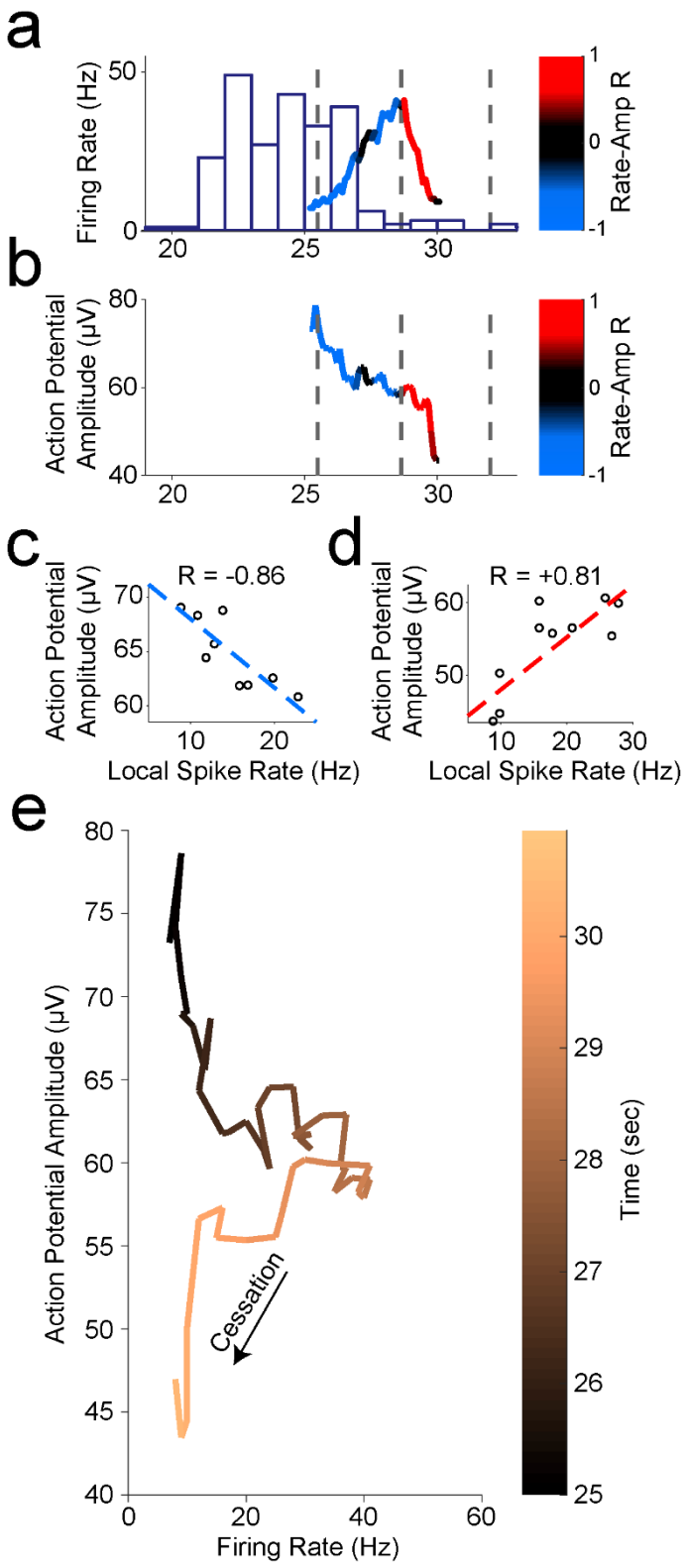
a
Firing Rate (Hz)
50
0
20
25
30
1
0
-1
Rate-Amp R
b
Action Potential Amplitude (μV)
80
60
40
20
25
30
1
0
-1
Rate-Amp R
c
R = -0.86
Action Potential Amplitude (μV)
70
65
60
10
20
Local Spike Rate (Hz)
d
R = +0.81
Action Potential Amplitude (μV)
60
50
10
20
30
Local Spike Rate (Hz)
e
Action Potential Amplitude (μV)
80
75
70
65
60
55
50
45
40
0
20
40
60
Firing Rate (Hz)
Cessation
30
29
28
27
26
25
Time (sec)

Extended Data Figure 3-9: Seizure progression is consistently associated with extracellular signs of depolarization block preceded by inhibition in single units.

- **a.** Firing rate *(upper)* and trough-to-peak spike amplitude (*lower*) of another example RS unit in Patient A, color-coded by the local correlation between spike rate and amplitude (in 1 second time bins) as an extracellular proxy for membrane potential and subthreshold input history. Firing rate of local FS unit is overlaid as purple histogram. Dotted lines indicate start and end times of two time periods of firing rate suppression characterized by different membrane potential signatures further characterized in (B), namely a negative correlation regime corresponding to inhibition followed by a positive correlation regime corresponding to over-excitation ending in firing rate cessation putatively though depolarization block.
- **b.** Example of negative correlation (*left*) between local spike rate and amplitude in first time period indicated by dotted lines in (A) and example of positive correlation (*right*) between local spike rate and amplitude in second time period indicated by dotted lines in (A). Least squares linear fit indicated in dotted lines following color scheme in (A) with Pearson's correlation coefficient indicated above each plot.
- **c.** Trajectory of unit activity over time during seizure in local spike rate vs spike amplitude space, with increasing time indicated by increasingly lighter copper color. RS unit is released from inhibition shortly following the cessation of activity in local FS unit as indicated by increasing firing rate with decreasing amplitude but then enters regime of over-excitation indicated by decreasing firing rate with decreasing amplitude at trajectory "corner" corresponding to a spiking rate of 40 Hz, until the unit ceases to fire likely due to depolarization block given these indicators of membrane potential history.

CHAPTER 4: Discussion and Future Directions

4.1 Network and cell-intrinsic dynamics interact in health and disease

This work highlights properties on the level of individual cells, including the shape of phase precession in hippocampal place cells and the sensitivity of FS neurons to depolarization block in human neocortex, as supporting stable population dynamics that are nevertheless flexible in responding to changing external and internal conditions, such as running speed and neural excitability levels. In particular, cell-type specific propensities to depolarization block determine the cell-type specific sequence of inhibition, recovery, and depolarization block that we postulate occur reproducibly across patients leading to seizure progression across the neocortex, with implications for therapeutic approaches with the proper timing relative to this sequence. Similarly, space and time coding mechanisms in the hippocampus were explored here based on the internal organization of place cell activity within theta cycles, also with consequences for the proper timing of episodic memory-supporting mechanisms that may utilize such sequences. In both cases, the dynamics of the internal network must be regulated to maintain stability while also performing behaviorally useful representation and processing of environmental inputs with their own dynamics.

Given that environmental dynamics can change rapidly, such as in the case of behavioral time warp at different running speeds, hippocampal and other neural circuits must employ mechanisms that maintain stability yet flexibility in their own dynamics. We have proposed two such mechanisms that maintain stability in the face of rapidly changing external inputs and internal conditions, first in the form of a logarithmic theta transform as implemented by the nonlinear shape of phase precession, and second in the form of fast-spiking inhibitory neuron activity prior to reaching depolarization block.

4.2 Comparison to previous studies on distance vs time coding by theta phase

It should be clarified that previous studies have systematically looked for whether the theta phase of place cell spikes correlates better with distance or with time, with the general consensus that distance correlates better on the single cell level despite variability on the population level (Gupta et al., 2012; Huxter et al., 2003; Jeewajee et al., 2014; Parra-Barrero et al., 2021). Recent insightful work has particularly shown that the related paradox of highly speed-dependent theta sequence trajectory lengths despite speed-invariant distance coding within individual place cells can be explained by a determination of place field size by the typical (“characteristic”) speed occurring at a position (Parra-Barrero et al., 2021), rather than instantaneous speed. This amounts to distance coding occurring on the individual field level across laps, and time coding being a consequence of the conditions during which the field was initially formed. We report the existence of some time coding happening across individual laps, and propose that the apparent difference can be explained by the change in position of the rodent that occurs over the course of a theta cycle at different running speeds. This is considered a

negligible amount (on the order of 1 to 10 cm) in comparison to the spatial extent of theta sequences (approximately 50 cm) in the prior study. It should be noted that, although strongly correlated, theta frequency does not follow running speed to any comparable percentage change, with no significant change when experimentally controlling for acceleration (Kropff et al., 2021), and from less than 1% to about 4% change in theta frequency (from about 7.5 Hz to 7.8 Hz) with a 32-fold increase in running speed in freely moving rats (Kennedy et al., 2022). Therefore, a multifold change in running speed would nevertheless cause an essentially multifold change in the distance traveled over the course of a theta cycle. This can cause a contraction in the phase-position relationship of up to about 20% if, for example the distance travelled in a theta cycle changes from 5 cm to 10 cm in a theta cycle that also represents a 25 cm theta sequence trajectory. Also note, the length of a theta sequence trajectory can vary independently of position or speed due to cognitive factors or navigational goals (Gupta et al., 2012; Wikenheiser & Redish, 2015a), so the theta sequence trajectory could become small relative to place field sizes depending on these factors (also discussed as cognitive space-warp in Chapter 2, Supplementary Figure 5), and increase the effective amount distortion in a purely distance coding framework. A speed-dependent contraction of the phase-position relationship of 20% is consistent with the amount of time coding observed here, and as shown in Figure 1 below, even such a 4:1 ratio of distance to time coding in phase can present significant time warp in spike time patterns. Furthermore, this warp can be alleviated by coding the part of the phase that is time-sensitive in a logarithmic fashion i.e. by LTT (Figure 2). To also prevent attributing relationships that only occur when pooling fields together of differing

characteristic speed (Parra-Barrero et al., 2021), we have analyzed all data on the individual field level in addition to pooled analysis throughout Chapter 2.

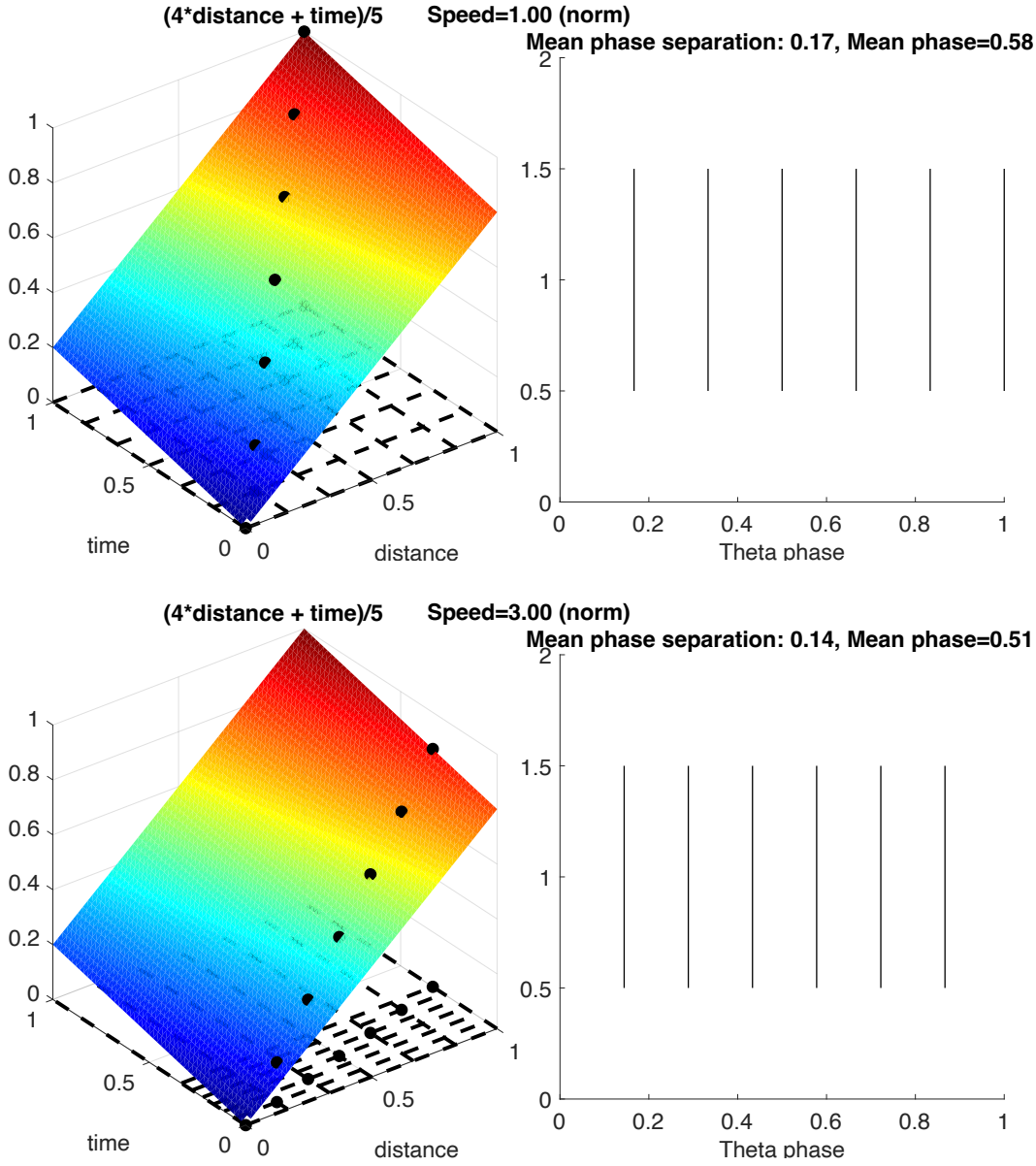

Figure 4-1. Even with dominant distance coding, just 20% time dependence of phase precession leads to contraction of spike time patterns with running speed.

Top plot shows a phase precession surface that is 4 times more sensitive to distance in field than to time in field. A running speed trajectory involving 7 simulated place cells each spiking according to this phase precession surface leads to a spike time pattern with mean separation 0.17 cycles. The same trajectory

traversed 3 times faster leads to a mean separation of 0.14 cycles, i.e. speed-dependent contraction of the resulting spike time pattern.

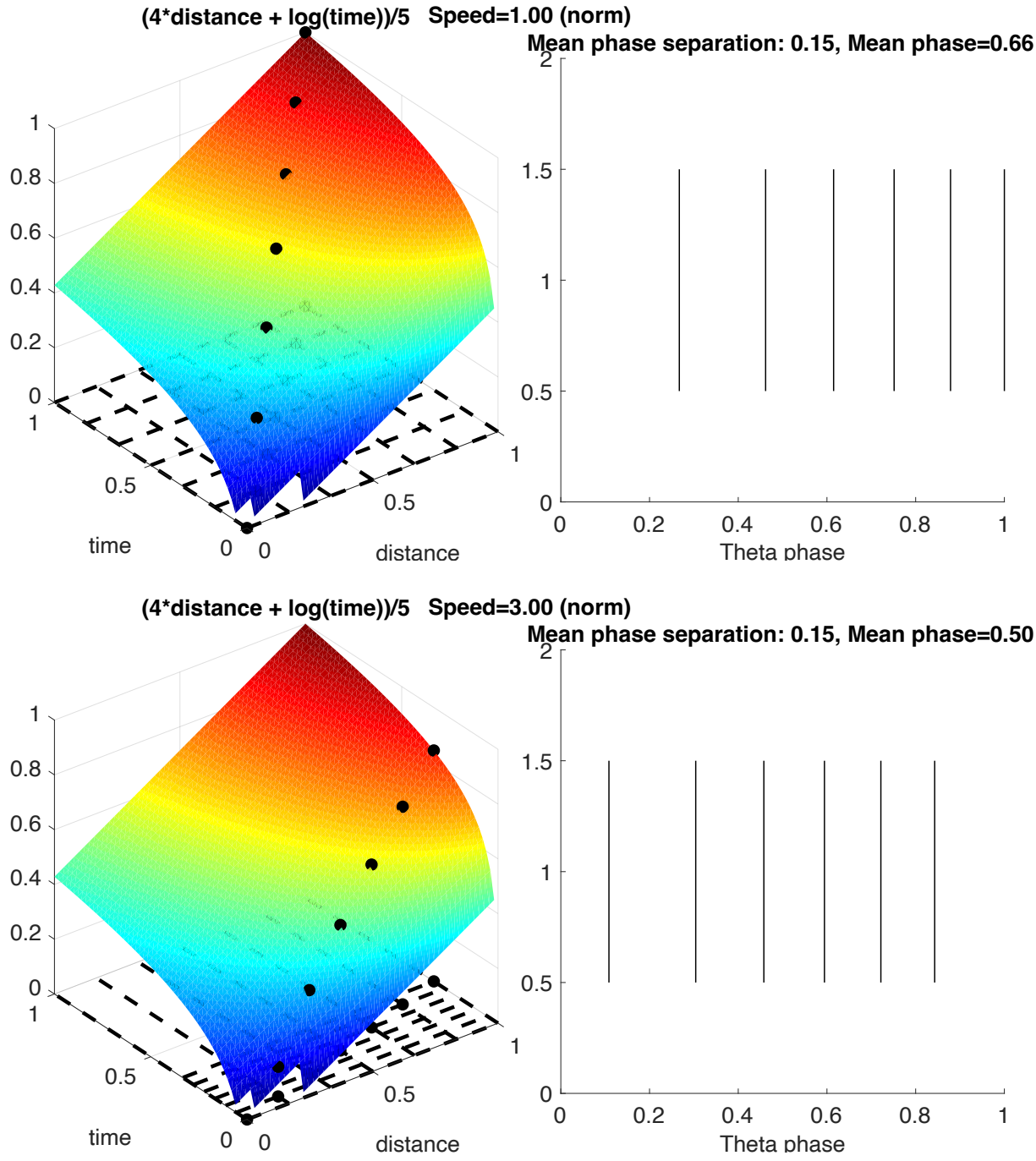

Figure 4-2. Even with dominant distance coding, logarithmic time coding of just the time-dependent portion of phase precession leads to stabilization of spike time patterns with respect to running speed.

Top plot shows a phase precession surface that is 4 times more sensitive to distance in field than to log(time). A running speed trajectory involving 7 simulated place cells each spiking according to this

phase precession surface leads to a spike time pattern with mean separation 0.15 cycles. The same trajectory traversed 3 times faster leads to a constant mean separation of 0.15 cycles, i.e. speed-invariant spike time pattern construction, while encoding speed in the offset of the pattern within a theta cycle.

4.3 Method of time-keeping in LTT in comparison to previous literature

The discretization of theta phase information from spikes is another difference from previous works that assume theta phase can continuously code for external variables (Dragoi & Buzsáki, 2006; Geisler et al., 2007). In our view, the chunking of variables into fundamental units of information processing is one of the most conspicuous potential functions of oscillations and should be considered in analysis of its phase code. As far as detection of cycles may introduce artificial bounds to this discretization, we incorporate the asymmetry of individual cycles in cycle detection and maintain that the separation of cycles is a general problem with discretizing time that these neural circuits should be robust to. Respecting the discrete nature of distinct cycles allows for analyzing relevant information closer to how neural circuits experience them, potentially with the unique advantages of time being discretized by theta cycles such as more efficient information representation. Indeed, the continuous representation of variables requires infinite information capacity. Therefore, at some point the information must be represented in a discrete form in the brain, and oscillatory cycles represent a plausible candidate for this. In terms of the effect of discretization on phase correlations, since theta phase within a cycle is positively correlated with both time and distance but the phase precession of spikes is negatively correlated with the same, discretization enhances the magnitude of circular-linear correlations by removing this within-cycle "phase rolling" effect (Sloin et al., 2022). Therefore, it was important to enforce the

same method of discretization when comparing the relative correlations of distance and time with phase to avoid unequal contributions of within-cycle phase rolling to phase correlation coefficients.

Despite the variability of theta frequency, we also consider theta cycles as keeping time for hippocampal circuits primarily in the sense that its change is accessible to a large number of neurons in the hippocampal formation and in potential decoders (Tingley & Buzsáki, 2018). Similar to discretization, this variability may also serve an information processing advantage in increasing the flexibility of temporal representations and chunking information into units that can be readout across circuits with a variety of dynamics and temporal resolutions (Deng et al., 2022). The idea of remaining time here is thus meant to encapsulate internally discretized fiducial time (Hopfield et al., 1998), not how time is traditionally defined as continuous, elapsed clock time which is not likely equally accessible by neural circuits participating in theta sequence generation.

4.4 Future Directions

The primary future direction of this work will be in demonstrating the computational benefits of temporally decoding speed-invariant theta sequences in downstream reader circuits, first within the context of a random feedforward CA3-CA1 hippocampal circuit. We propose that such an arrangement can support place field generation prior to learning via dendritic sequence decoding (Beniaguev et al., 2022; Branco et al., 2010). The stability of this network arrangement should be assessed in the extent of speed intensities for which the model maintains a given output state. The flexibility can be

quantified as the extent of linearly separable output states, i.e. downstream decoder firing rates, that can be produced by the circuit in response to different theta sequences. Temporal coding schemes like the one inspired by hippocampal circuits here may offer crucial robustness amidst variation that can be decoded by ubiquitous neural computing elements like dendritic sequence sensitivity, and therefore play an important role across the brain in handling information on patterns that evolve over time.

BIBLIOGRAPHY

Adesnik, H., & Abdeladim, L. (2021). Probing neural codes with two-photon holographic optogenetics. *Nature Neuroscience*, *24*(10), 1356–1366. https://doi.org/10.1038/s41593-021-00902-9

Ahmed, O. J., & Mehta, M. R. (2012). *Running Speed Alters the Frequency of Hippocampal Gamma Oscillations*. 11.

Annegers, J. F. (2001). The Treatment of Epilepsy: Principles and Practice. (Third Edition). In E. Wyllie (Ed.), *The Treatment of Epilepsy: Principles and PRac* (pp. 131–138). Wiley. https://doi.org/10.1002/hup.372

Aronov, D., Nevers, R., & Tank, D. W. (2017). Mapping of a non-spatial dimension by the hippocampal–entorhinal circuit. *Nature*, *543*(7647), 719–722. https://doi.org/10.1038/nature21692

Ashhad, S., & Feldman, J. L. (2020). Emergent Elements of Inspiratory Rhythmogenesis: Network Synchronization and Synchrony Propagation. *Neuron*. https://doi.org/10.1016/j.neuron.2020.02.005

Avoli, M., Biagini, G., & de Curtis, M. (2006). Do Interictal Spikes Sustain Seizures and Epileptogenesis? *Epilepsy Currents*, *6*(6), 203–207. https://doi.org/10.1111/j.1535-7511.2006.00146.x

Avoli, M., & de Curtis, M. (2011). GABAergic synchronization in the limbic system and its role in the generation of epileptiform activity. In *Progress in Neurobiology* (Vol. 95, Issue 2, pp. 104–132). https://doi.org/10.1016/j.pneurobio.2011.07.003

Barry, C., Hayman, R., Burgess, N., & Jeffery, K. J. (2007). Experience-dependent rescaling of entorhinal grids. *Nature Neuroscience*, *10*(6), 682–684. https://doi.org/10.1038/nn1905

Bell, B., Lin, J., Seidenberg, M., & Hermann, B. (2011). The neurobiology of cognitive disorders in temporal lobe epilepsy. *Nature Reviews. Neurology*, *7*, 154–164. https://doi.org/10.1038/nrneurol.2011.3

Belluscio, M. A., Mizuseki, K., Schmidt, R., Kempter, R., & Buzsáki, G. (2012). Cross-Frequency Phase–Phase Coupling between Theta and Gamma Oscillations in the Hippocampus. *Journal of Neuroscience*, *32*(2), 423–435. https://doi.org/10.1523/JNEUROSCI.4122-11.2012

Beniaguev, D., Shapira, S., Segev, I., & London, M. (2022). *Multiple Synaptic Contacts combined with Dendritic Filtering enhance Spatio-Temporal Pattern Recognition capabilities of Single Neurons* [Preprint]. Neuroscience. https://doi.org/10.1101/2022.01.28.478132

Berens, P. (2009). CircStat: A MATLAB Toolbox for Circular Statistics. *Journal of Statistical Software*, *31*(1), 1–21. https://doi.org/10.18637/jss.v031.i10

Berényi, A., Belluscio, M., Mao, D., & Buzsáki, G. (2012). Closed-loop control of epilepsy by transcranial electrical stimulation. *Science*, *337*(6095), 735–737. https://doi.org/10.1126/science.1223154

Beverlin, B., Kakalios, J., Nykamp, D., & Netoff, T. I. (2012). Dynamical changes in neurons during seizures determine tonic to clonic shift. *Journal of Computational Neuroscience*, *33*(1), 41–51. https://doi.org/10.1007/s10827-011-0373-5

Bieri, K. W., Bobbitt, K. N., & Colgin, L. L. (2014). Slow and Fast Gamma Rhythms Coordinate Different Spatial Coding Modes in Hippocampal Place Cells. *Neuron*, *82*(3), 670–681. https://doi.org/10.1016/j.neuron.2014.03.013

Bikson, M., Hahn, P. J., Fox, J. E., & Jefferys, J. G. R. (2003). Depolarization Block of Neurons During Maintenance of Electrographic Seizures. *Journal of Neurophysiology*, *90*(4), 2402–2408. https://doi.org/10.1152/jn.00467.2003

Bittner, K. C., Grienberger, C., Vaidya, S. P., Milstein, A. D., Macklin, J. J., Suh, J., Tonegawa, S., & Magee, J. C. (2015). Conjunctive input processing drives feature selectivity in hippocampal CA1 neurons. *Nature Neuroscience*, *18*(8), 1133–1142. https://doi.org/10.1038/nn.4062

Blumenfeld, H. (2005). Cellular and network mechanisms of spike-wave seizures. In *Epilepsia* (Vol. 46, Issue SUPPL. 9, pp. 21–33). https://doi.org/10.1111/j.1528-1167.2005.00311.x

Booth, V., & Bose, A. (2001). Neural Mechanisms for Generating Rate and Temporal Codes in Model CA3 Pyramidal Cells. *Journal of Neurophysiology*, *85*(6), 2432–2445. https://doi.org/10.1152/jn.2001.85.6.2432

Branco, T., Clark, B. A., & Hausser, M. (2010). Dendritic Discrimination of Temporal Input Sequences in Cortical Neurons. *Science*, *329*(5999), 1671–1675. https://doi.org/10.1126/science.1189664

Buchin, A., Chizhov, A., Huberfeld, G., Miles, R., & Gutkin, B. S. (2016). Reduced Efficacy of the KCC2 Cotransporter Promotes Epileptic Oscillations in a Subiculum Network Model. *The Journal of Neuroscience: The Official Journal of the Society for Neuroscience*, *36*(46), 11619–11633. https://doi.org/10.1523/JNEUROSCI.4228-15.2016

Buckmaster, P. S., Jongen-Rêlo, A. L., Davari, S. B., & Wong, E. H. (2000). Testing the disinhibition hypothesis of epileptogenesis in vivo and during spontaneous seizures. *The Journal of Neuroscience : The Official Journal of the Society for Neuroscience*, *20*(16), 6232–6240.

Burgess, N. (2008). Grid cells and theta as oscillatory interference: Theory and predictions. *Hippocampus*, *18*(12), 1157–1174. https://doi.org/10.1002/hipo.20518

Burgess, N., Barry, C., & O'Keefe, J. (2007). An oscillatory interference model of grid cell firing. *Hippocampus*, *17*(9), 801–812. https://doi.org/10.1002/hipo.20327

Bush, N. E., Solla, S. A., & Hartmann, M. J. (2016). Whisking mechanics and active sensing. *Current Opinion in Neurobiology*, *40*, 178–188. https://doi.org/10.1016/j.conb.2016.08.001

Butera, R. J., Rinzel, J., & Smith, J. C. (1999). Models of Respiratory Rhythm Generation in the Pre-Bötzinger Complex. I. Bursting Pacemaker Neurons. *Journal of Neurophysiology*, *82*(1), 382–397. https://doi.org/10.1152/jn.1999.82.1.382

Buzsáki, G. (2010). Neural Syntax: Cell Assemblies, Synapsembles, and Readers. *Neuron*, *68*(3), 362–385. https://doi.org/10.1016/j.neuron.2010.09.023

Buzsáki, G., & Mizuseki, K. (2014). The log-dynamic brain: How skewed distributions affect network operations. *Nature Reviews Neuroscience*, *15*(4), 264–278. https://doi.org/10.1038/nrn3687

Buzsáki, G., & Moser, E. I. (2013). Memory, navigation and theta rhythm in the hippocampal-entorhinal system. *Nature Neuroscience*, *16*(2), 130–138. https://doi.org/10.1038/nn.3304

Cammarota, M., Losi, G., Chiavegato, A., Zonta, M., & Carmignoto, G. (2013). Fast spiking interneuron control of seizure propagation in a cortical slice model of focal epilepsy. *The Journal of Physiology*, *591*(4), 807–822. https://doi.org/10.1113/jphysiol.2012.238154

Cardin, J. A., Carlén, M., Meletis, K., Knoblich, U., Zhang, F., Deisseroth, K., Tsai, L. H., & Moore, C. I. (2009). Driving fast-spiking cells induces gamma rhythm and controls sensory responses. *Nature*, *459*(7247), 663–667. https://doi.org/10.1038/nature08002

Carr, C. E. (1993). Delay Line Models of Sound Localization in the Barn Owl. *American Zoologist*, *33*(1), 79–85.

Chagnac-Amitai, Y., & Connors, B. W. (1989). Horizontal spread of synchronized activity in neocortex and its control by GABA-mediated inhibition. *Journal of Neurophysiology*, *61*(4), 747–758. https://doi.org/10.1152/jn.1989.61.4.747

Charupanit, K., Sen-Gupta, I., Lin, J. J., & Lopour, B. A. (2020). Amplitude of high frequency oscillations as a biomarker of the seizure onset zone. *Clinical Neurophysiology*, *131*(11), 2542–2550. https://doi.org/10.1016/j.clinph.2020.07.021

Chervin, R. D., Pierce, P. A., & Connors, B. W. (1988). Periodicity and directionality in the propagation of epileptiform discharges across neocortex. *Journal of Neurophysiology*, *60*(5), 1695–1713. https://doi.org/10.1152/jn.1988.60.5.1695

Climer, J. R., Newman, E. L., & Hasselmo, M. E. (2013). Phase coding by grid cells in unconstrained environments: Two-dimensional phase precession. *The European Journal of Neuroscience*, *38*(4), 2526–2541. https://doi.org/10.1111/ejn.12256

Colgin, L. L. (2015). Theta–gamma coupling in the entorhinal–hippocampal system. *Current Opinion in Neurobiology*, *31*, 45–50. https://doi.org/10.1016/j.conb.2014.08.001

Connors, B. W., Pinto, D. J., & Telfeian, A. E. (2001). Local pathways of seizure propagation in neocortex. *International Review of Neurobiology*, *45*, 527–546. https://doi.org/10.1016/s0074-7742(01)45027-6

Cope, D. W., Di Giovanni, G., Fyson, S. J., Orbán, G., Errington, A. C., Lrincz, M. L., Gould, T. M., Carter, D. A., & Crunelli, V. (2009). Enhanced tonic GABA A inhibition in typical absence epilepsy. *Nature Medicine*, *15*(12), 1392–1398. https://doi.org/10.1038/nm.2058

Cruikshank, S. J., Lewis, T. J., & Connors, B. W. (2007). Synaptic basis for intense thalamocortical activation of feedforward inhibitory cells in neocortex. *Nature Neuroscience*, *10*(4), 462–468. https://doi.org/10.1038/nn1861

de Polavieja, G. G. (2005). Stimulus History Reliably Shapes Action Potential Waveforms of Cortical Neurons. *Journal of Neuroscience*, *25*(23), 5657–5665. https://doi.org/10.1523/JNEUROSCI.0242-05.2005

Deng, X., Chen, S., Sosa, M., Karlsson, M. P., Wei, X.-X., & Frank, L. M. (2022). A Variable Clock Underlies Internally Generated Hippocampal Sequences. *The Journal of Neuroscience: The Official Journal of the Society for Neuroscience*, *42*(18), 3797–3810. https://doi.org/10.1523/JNEUROSCI.1120-21.2022

Deschênes, M., Moore, J., & Kleinfeld, D. (2012). Sniffing and whisking in rodents. *Current Opinion in Neurobiology*, *22*(2), 243–250. https://doi.org/10.1016/j.conb.2011.11.013

Douchamps, V., Jeewajee, A., Blundell, P., Burgess, N., & Lever, C. (2013). Evidence for Encoding versus Retrieval Scheduling in the Hippocampus by Theta Phase and Acetylcholine. *Journal of Neuroscience*, *33*(20), 8689–8704. https://doi.org/10.1523/JNEUROSCI.4483-12.2013

Dragoi, G., & Buzsáki, G. (2006). Temporal Encoding of Place Sequences by Hippocampal Cell Assemblies. *Neuron*, *50*(1), 145–157. https://doi.org/10.1016/j.neuron.2006.02.023

Elahian, B., Lado, N. E., Mankin, E., Vangala, S., Misra, A., Moxon, K., Fried, I., Sharan, A., Yeasin, M., Staba, R., Bragin, A., Avoli, M., Sperling, M. R., Engel, J., & Weiss, S. A. (2018). Low-voltage fast seizures in humans begin with increased interneuron firing. *Annals of Neurology*, *84*(4), 588–600. https://doi.org/10.1002/ana.25325

Eliav, T., Geva-Sagiv, M., Yartsev, M. M., Finkelstein, A., Rubin, A., Las, L., & Ulanovsky, N. (2018). Nonoscillatory Phase Coding and Synchronization in the Bat Hippocampal Formation. *Cell*, *175*(4), 1119-1130.e15. https://doi.org/10.1016/j.cell.2018.09.017

Farrell, J. S., Nguyen, Q.-A., & Soltesz, I. (2019). Resolving the Micro-Macro Disconnect to Address Core Features of Seizure Networks. *Neuron*, *101*(6), 1016–1028. https://doi.org/10.1016/j.neuron.2019.01.043

Feng, T., Silva, D., & Foster, D. J. (2015). Dissociation between the Experience-Dependent Development of Hippocampal Theta Sequences and Single-Trial Phase Precession. *Journal of Neuroscience*, *35*(12), 4890–4902. https://doi.org/10.1523/JNEUROSCI.2614-14.2015

Fernández-Ruiz, A., Oliva, A., Nagy, G. A., Maurer, A. P., Berényi, A., & Buzsáki, G. (2017). Entorhinal-CA3 Dual-Input Control of Spike Timing in the Hippocampus by Theta-Gamma Coupling. *Neuron*, *93*(5), 1213-1226.e5. https://doi.org/10.1016/j.neuron.2017.02.017

Fisher, R. S., Pedley, T. A., Moody, W. J., & Prince, D. A. (1976). The role of extracellular potassium in hippocampal epilepsy. *Archives of Neurology*, *33*(2), 76–83. https://doi.org/10.1001/archneur.1976.00500020004002

Foster, D. J., & Wilson, M. A. (2007). Hippocampal theta sequences. *Hippocampus*, *17*(11), 1093–1099. https://doi.org/10.1002/hipo.20345

Fröhlich, F., Bazhenov, M., Iragui-Madoz, V., & Sejnowski, T. J. (2008). Potassium Dynamics in the Epileptic Cortex: New Insights on an Old Topic. *The Neuroscientist*, *14*(5), 422–433. https://doi.org/10.1177/1073858408317955

Fröhlich, F., Sejnowski, T. J., & Bazhenov, M. (2010). Network Bistability Mediates Spontaneous Transitions between Normal and Pathological Brain States. *Journal of Neuroscience*, *30*(32), 10734–10743. https://doi.org/10.1523/JNEUROSCI.1239-10.2010

Geiller, T., Sadeh, S., Rolotti, S. V., Blockus, H., Vancura, B., Negrean, A., Murray, A. J., Rózsa, B., Polleux, F., Clopath, C., & Losonczy, A. (2022). Local circuit amplification of spatial selectivity in the hippocampus. *Nature*, *601*(7891), 105–109. https://doi.org/10.1038/s41586-021-04169-9

Geisler, C., Robbe, D., Zugaro, M., Sirota, A., & Buzsaki, G. (2007). Hippocampal place cell assemblies are speed-controlled oscillators. *Proceedings of the National Academy of Sciences*, *104*(19), 8149–8154. https://doi.org/10.1073/pnas.0610121104

Ghosh, M., Shanahan, B. E., Furtak, S. C., Mashour, G. A., Burwell, R. D., & Ahmed, O. J. (2020). Instantaneous amplitude and shape of postrhinal theta oscillations differentially encode running speed. *Behavioral Neuroscience*, *134*(6), 516–528. https://doi.org/10.1037/bne0000416

Golomb, D., & Amitai, Y. (1997). Propagating neuronal discharges in neocortical slices: Computational and experimental study. *Journal of Neurophysiology*, *78*(3), 1199–1211. https://doi.org/10.1152/jn.1997.78.3.1199

Gotman, J. (1991). Relationships Between Interictal Spiking and Seizures: Human and Experimental Evidence. *Canadian Journal of Neurological Sciences / Journal Canadien Des Sciences Neurologiques*, *18*(S4), 573–576. https://doi.org/10.1017/S031716710003273X

Grosmark, A. D., & Buzsáki, G. (2016). Diversity in neural firing dynamics supports both rigid and learned hippocampal sequences. *Science*, *351*(6280), 1440–1443. https://doi.org/10.1126/science.aad1935

Gupta, A. S., van der Meer, M. A. A., Touretzky, D. S., & Redish, A. D. (2012). Segmentation of spatial experience by hippocampal theta sequences. *Nature Neuroscience*, *15*(7), 1032–1039. https://doi.org/10.1038/nn.3138

Gutnick, M. J., Connors, B. W., & Prince, D. A. (1982). Mechanisms of neocortical epileptogenesis in vitro. *Journal of Neurophysiology*, *48*(6), 1321–1335. https://doi.org/10.1152/jn.1982.48.6.1321

Harvey, C. D., Collman, F., Dombeck, D. A., & Tank, D. W. (2009). Intracellular dynamics of hippocampal place cells during virtual navigation. *Nature*, *461*(7266), 941–946. https://doi.org/10.1038/nature08499

Hinman, J. R., Brandon, M. P., Climer, J. R., Chapman, G. W., & Hasselmo, M. E. (2016). Multiple Running Speed Signals in Medial Entorhinal Cortex. *Neuron*, *91*(3), 666–679. https://doi.org/10.1016/j.neuron.2016.06.027

Hoffman, D. A., Magee, J. C., Colbert, C. M., & Johnston, D. (1997). K+ channel regulation of signal propagation in dendrites of hippocampal pyramidal neurons. *Nature*, *387*(6636), 869–875. https://doi.org/10.1038/43119

Hopfield, J. J. (1995). Pattern recognition computation using action potential timing for stimulus representation. *Nature*, *376*(6535), 33–36. https://doi.org/10.1038/376033a0

Hopfield, J. J. (1996). Transforming neural computations and representing time. *Proceedings of the National Academy of Sciences*, *93*(26), 15440–15444. https://doi.org/10.1073/pnas.93.26.15440

Hopfield, J. J., & Brody, C. D. (2001). What is a moment? Transient synchrony as a collective mechanism for spatiotemporal integration. *PNAS*, *98*(3), 1282–1287.

Hopfield, J. J., Brody, C., & Roweis, S. (1998). Computing with Action Potentials. *Advances in Neural Information Processing Systems*, *10*. https://papers.nips.cc/paper/1997/hash/6c1da886822c67822bcf3679d04369fa-Abstract.html

Howard, M. W., MacDonald, C. J., Tiganj, Z., Shankar, K. H., Du, Q., Hasselmo, M. E., & Eichenbaum, H. (2014). A Unified Mathematical Framework for Coding Time, Space, and Sequences in the Hippocampal Region. *Journal of Neuroscience*, *34*(13), 4692–4707. https://doi.org/10.1523/JNEUROSCI.5808-12.2014

Howard, M. W., Shankar, K. H., Aue, W. R., & Criss, A. H. (2015). A distributed representation of internal time. *Psychological Review*, *122*(1), 24–53. https://doi.org/10.1037/a0037840

Huxter, J., Burgess, N., & O'Keefe, J. (2003). Independent rate and temporal coding in hippocampal pyramidal cells. *Nature*, *425*(6960), 828–832. https://doi.org/10.1038/nature02058

Ishikawa, T., & Ikegaya, Y. (2020). Locally sequential synaptic reactivation during hippocampal ripples. *Science Advances*, *6*(7), eaay1492. https://doi.org/10.1126/sciadv.aay1492

Jaramillo, J., & Kempter, R. (2017). Phase precession: A neural code underlying episodic memory? *Current Opinion in Neurobiology*, *43*, 130–138. https://doi.org/10.1016/j.conb.2017.02.006

Jeewajee, A., Barry, C., Douchamps, V., Manson, D., Lever, C., & Burgess, N. (2014). Theta phase precession of grid and place cell firing in open environments. *Philosophical Transactions of the Royal Society B: Biological Sciences*, *369*(1635). https://doi.org/10.1098/rstb.2012.0532

Jirsa, V. K., Stacey, W. C., Quilichini, P. P., Ivanov, A. I., & Bernard, C. (2014). On the nature of seizure dynamics. *Brain*, *137*(8), 2210–2230. https://doi.org/10.1093/brain/awu133

John, T., Kiss, T., Lever, C., & Érdi, P. (2014). Anxiolytic drugs and altered hippocampal theta rhythms: The quantitative systems pharmacological approach. *Network (Bristol, England)*, *25*(1–2), 20–37. https://doi.org/10.3109/0954898X.2013.880003

Johnson, K. O. (2000). Neural Coding. *Neuron*, *26*(3), 563–566. https://doi.org/10.1016/S0896-6273(00)81193-9

Jones, M. W., & Wilson, M. A. (2005). Phase precession of medial prefrontal cortical activity relative to the hippocampal theta rhythm. *Hippocampus*, *15*(7), 867–873. https://doi.org/10.1002/hipo.20119

Kaplan, R., Doeller, C. F., Barnes, G. R., Litvak, V., Düzel, E., Bandettini, P. A., & Burgess, N. (2012). Movement-Related Theta Rhythm in Humans: Coordinating Self-Directed Hippocampal Learning. *PLOS Biology*, *10*(2), e1001267. https://doi.org/10.1371/journal.pbio.1001267

Karlócai, M. R., Kohus, Z., Káli, S., Ulbert, I., Szabó, G., Máté, Z., Freund, T. F., & Gulyás, A. I. (2014). Physiological sharp wave-ripples and interictal events in vitro: What's the difference? *Brain : A Journal of Neurology*, *137*(Pt 2), 463–485. https://doi.org/10.1093/brain/awt348

Katz, P. S. (2016). Evolution of central pattern generators and rhythmic behaviours. *Philosophical Transactions of the Royal Society B: Biological Sciences*, *371*(1685), 20150057. https://doi.org/10.1098/rstb.2015.0057

Kawaguchi, Y. (1995). Physiological subgroups of nonpyramidal cells with specific morphological characteristics in layer II/III of rat frontal cortex. *Journal of Neuroscience*, *15*(4), 2638–2655. https://doi.org/10.1523/jneurosci.15-04-02638.1995

Kempter, R., Leibold, C., Buzsáki, G., Diba, K., & Schmidt, R. (2012). Quantifying circular–linear associations: Hippocampal phase precession. *Journal of Neuroscience Methods*, *207*(1), 113–124. https://doi.org/10.1016/j.jneumeth.2012.03.007

Kennedy, J. P., Zhou, Y., Qin, Y., Lovett, S. D., Sheremet, A., Burke, S. N., & Maurer, A. P. (2022). A Direct Comparison of Theta Power and Frequency to Speed and Acceleration. *The Journal of Neuroscience*, *42*(21), 4326–4341. https://doi.org/10.1523/JNEUROSCI.0987-21.2022

Khoshkhoo, S., Vogt, D., & Sohal, V. S. (2017). Dynamic, Cell-Type-Specific Roles for GABAergic Interneurons in a Mouse Model of Optogenetically Inducible Seizures. *Neuron*, *93*(2), 291–298. https://doi.org/10.1016/j.neuron.2016.11.043

Klausberger, T., & Somogyi, P. (2008). Neuronal Diversity and Temporal Dynamics: The Unity of Hippocampal Circuit Operations. *Science*, *321*(5885), 53–57. https://doi.org/10.1126/science.1149381

Koizumi, H., & Smith, J. C. (2008). Persistent Na+ and K+-Dominated Leak Currents Contribute to Respiratory Rhythm Generation in the Pre-Botzinger Complex In Vitro. *Journal of Neuroscience*, *28*(7), 1773–1785. https://doi.org/10.1523/JNEUROSCI.3916-07.2008

Kramer, M. A., Truccolo, W., Eden, U. T., Lepage, K. Q., Hochberg, L. R., Eskandar, E. N., Madsen, J. R., Leek, J. W., Maheshwari, A., Halgren, E., Chu, C. J., & Cash, S. S. (2012). Human seizures self-terminate across spatial scales via a critical transition. *Proceedings of the National Academy of Sciences of the United States of America*, *109*(51), 21116–21121. https://doi.org/10.1073/pnas.1210047110

Kraus, B. J., Brandon, M. P., Robinson, R. J., Connerney, M. A., Hasselmo, M. E., & Eichenbaum, H. (2015). During Running in Place, Grid Cells Integrate Elapsed Time and Distance Run. *Neuron*, *88*(3), 578–589. https://doi.org/10.1016/j.neuron.2015.09.031

Kraus, B. J., Robinson, R. J., White, J. A., Eichenbaum, H., & Hasselmo, M. E. (2013). Hippocampal "Time Cells": Time versus Path Integration. *Neuron*, *78*(6), 1090–1101. https://doi.org/10.1016/j.neuron.2013.04.015

Krook-Magnuson, E., Armstrong, C., Oijala, M., & Soltesz, I. (2013). On-demand optogenetic control of spontaneous seizures in temporal lobe epilepsy. *Nature Communications*, *4*(1), 1–8. https://doi.org/10.1038/ncomms2376

Kropff, E., Carmichael, J. E., Moser, E. I., & Moser, M.-B. (2021). Frequency of theta rhythm is controlled by acceleration, but not speed, in running rats. *Neuron*, *109*(6), 1029-1039.e8. https://doi.org/10.1016/j.neuron.2021.01.017

Leifeld, J., Förster, E., Reiss, G., & Hamad, M. I. K. (2022). Considering the Role of Extracellular Matrix Molecules, in Particular Reelin, in Granule Cell Dispersion Related to Temporal Lobe Epilepsy. *Frontiers in Cell and Developmental Biology*, *10*. https://www.frontiersin.org/articles/10.3389/fcell.2022.917575

Lengyel, M., Szatmáry, Z., & Erdi, P. (2003). Dynamically detuned oscillations account for the coupled rate and temporal code of place cell firing. *Hippocampus*, *13*(6), 700–714. https://doi.org/10.1002/hipo.10116

Lever, C., Wills, T., Cacucci, F., Burgess, N., & O'Keefe, J. (2002). Long-term plasticity in hippocampal place-cell representation of environmental geometry. *Nature*, *416*(6876), 90–94. https://doi.org/10.1038/416090a

Lévesque, M., Herrington, R., Hamidi, S., & Avoli, M. (2016). Interneurons spark seizure-like activity in the entorhinal cortex. *Neurobiology of Disease*, *87*, 91–101. https://doi.org/10.1016/j.nbd.2015.12.011

Lien, C. C., & Jonas, P. (2003). Kv3 potassium conductance is necessary and kinetically optimized for high-frequency action potential generation in hippocampal interneurons. *Journal of Neuroscience*, *23*(6), 2058–2068. https://doi.org/10.1523/jneurosci.23-06-02058.2003

Liljenström, H. (2003). Neural Stability and Flexibility: A Computational Approach. *Neuropsychopharmacology*, *28*(1), S64–S73. https://doi.org/10.1038/sj.npp.1300137

Liou, J. Y., Smith, E. H., Bateman, L. M., Bruce, S. L., McKhann, G. M., Goodman, R. R., Emerson, R. G., Schevon, C. A., & Abbott, L. F. (2020). A model for focal seizure onset, propagation, evolution, and progression. *ELife*, *9*. https://doi.org/10.7554/eLife.50927

Lisman, J. E., & Jensen, O. (2013). The Theta-Gamma Neural Code. *Neuron*, *77*(6), 1002–1016. https://doi.org/10.1016/j.neuron.2013.03.007

Long, M. A., Jin, D. Z., & Fee, M. S. (2010). Support for a synaptic chain model of neuronal sequence generation. *Nature*, *468*(7322), 394–399. https://doi.org/10.1038/nature09514

Marder, E., & Bucher, D. (2001). Central pattern generators and the control of rhythmic movements. *Current Biology*, *11*(23), R986–R996. https://doi.org/10.1016/S0960-9822(01)00581-4

Markram, H., Toledo-Rodriguez, M., Wang, Y., Gupta, A., Silberberg, G., & Wu, C. (2004). Interneurons of the neocortical inhibitory system. In *Nature Reviews Neuroscience* (Vol. 5, Issue 10, pp. 793–807). https://doi.org/10.1038/nrn1519

Martina, M., Schultz, J. H., Ehmke, H., Monyer, H., & Jonas, P. (1998). Functional and molecular differences between voltage-gated K+ channels of fast-spiking interneurons and pyramidal neurons of rat hippocampus. *Journal of Neuroscience*, *18*(20), 8111–8125. https://doi.org/10.1523/jneurosci.18-20-08111.1998

Maturana, M. I., Meisel, C., Dell, K., Karoly, P. J., D'Souza, W., Grayden, D. B., Burkitt, A. N., Jiruska, P., Kudlacek, J., Hlinka, J., Cook, M. J., Kuhlmann, L., & Freestone, D. R. (2020). Critical slowing down as a biomarker for seizure susceptibility. *Nature Communications*, *11*(1), 2172. https://doi.org/10.1038/s41467-020-15908-3

Maurer, A. P., Burke, S. N., Lipa, P., Skaggs, W. E., & Barnes, C. A. (2012). Greater running speeds result in altered hippocampal phase sequence dynamics. *Hippocampus*, *22*(4), 737–747. https://doi.org/10.1002/hipo.20936

McClain, K., Tingley, D., Heeger, D. J., & Buzsáki, G. (2019). Position–theta-phase model of hippocampal place cell activity applied to quantification of running speed modulation of firing rate. *Proceedings of the National Academy of Sciences*, *116*(52), 27035–27042. https://doi.org/10.1073/pnas.1912792116

McCormick, D. A., Connors, B. W., Lighthall, J. W., & Prince, D. A. (1985). Comparative electrophysiology of pyramidal and sparsely spiny stellate neurons of the neocortex. *Journal of Neurophysiology*, *54*(4), 782–806. https://doi.org/10.1152/jn.1985.54.4.782

Meer, M. A. A. van der, & Redish, A. D. (2011). Theta Phase Precession in Rat Ventral Striatum Links Place and Reward Information. *Journal of Neuroscience*, *31*(8), 2843–2854. https://doi.org/10.1523/JNEUROSCI.4869-10.2011

Megías, M., Emri, Z., Freund, T. F., & Gulyás, A. I. (2001). Total number and distribution of inhibitory and excitatory synapses on hippocampal CA1 pyramidal cells. *Neuroscience*, *102*(3), 527–540. https://doi.org/10.1016/S0306-4522(00)00496-6

Mehta, M. R., Lee, A. K., & Wilson, M. A. (2002). Role of experience and oscillations in transforming a rate code into a temporal code. *Nature*, *417*(6890), 741–746. https://doi.org/10.1038/nature00807

Merricks, E. M., Smith, E. H., McKhann, G. M., Goodman, R. R., Bateman, L. M., Emerson, R. G., Schevon, C. A., & Trevelyan, A. J. (2015). Single unit action potentials in humans and the

effect of seizure activity. *Brain : A Journal of Neurology*, *138*(Pt 10), 2891–2906. https://doi.org/10.1093/brain/awv208

Miri, M. L., Vinck, M., Pant, R., & Cardin, J. A. (2018). Altered hippocampal interneuron activity precedes ictal onset. *ELife*, *7*, e40750. https://doi.org/10.7554/eLife.40750

Mizuseki, K., & Buzsáki, G. (2013). Preconfigured, Skewed Distribution of Firing Rates in the Hippocampus and Entorhinal Cortex. *Cell Reports*, *4*(5), 1010–1021. https://doi.org/10.1016/j.celrep.2013.07.039

Mizuseki, K., Sirota, A., Pastalkova, E., & Buzsáki, G. (2009). Theta Oscillations Provide Temporal Windows for Local Circuit Computation in the Entorhinal-Hippocampal Loop. *Neuron*, *64*(2), 267–280. https://doi.org/10.1016/j.neuron.2009.08.037

Neumann, A. R., Raedt, R., Steenland, H. W., Sprengers, M., Bzymek, K., Navratilova, Z., Mesina, L., Xie, J., Lapointe, V., Kloosterman, F., Vonck, K., Boon, P. A. J. M., Soltesz, I., McNaughton, B. L., & Luczak, A. (2017). Involvement of fast-spiking cells in ictal sequences during spontaneous seizures in rats with chronic temporal lobe epilepsy. *Brain : A Journal of Neurology*, *140*(9), 2355–2369. https://doi.org/10.1093/brain/awx179

Nitzan, N., McKenzie, S., Beed, P., English, D. F., Oldani, S., Tukker, J. J., Buzsáki, G., & Schmitz, D. (2020). Propagation of hippocampal ripples to the neocortex by way of a subiculum-retrosplenial pathway. *Nature Communications*, *11*(1), 1947. https://doi.org/10.1038/s41467-020-15787-8

Nowak, L. G., Azouz, R., Sanchez-Vives, M. V., Gray, C. M., & McCormick, D. A. (2003). Electrophysiological classes of cat primary visual cortical neurons in vivo as revealed by

quantitative analyses. *Journal of Neurophysiology*, *89*(3), 1541–1566. https://doi.org/10.1152/jn.00580.2002

O'Keefe, J., & Burgess, N. (2005). Dual phase and rate coding in hippocampal place cells: Theoretical significance and relationship to entorhinal grid cells. *Hippocampus*, *15*(7), 853–866. https://doi.org/10.1002/hipo.20115

O'Keefe, J., & Recce, M. L. (1993). Phase relationship between hippocampal place units and the EEG theta rhythm. *Hippocampus*, *3*(3), 317–330. https://doi.org/10.1002/hipo.450030307

Parra-Barrero, E., Diba, K., & Cheng, S. (2021). Neuronal sequences during theta rely on behavior-dependent spatial maps. *ELife*, *10*, e70296. https://doi.org/10.7554/eLife.70296

Pastalkova, E., Itskov, V., Amarasingham, A., & Buzsáki, G. (2008). Internally Generated Cell Assembly Sequences in the Rat Hippocampus. *Science*, *321*(5894), 1322–1327. https://doi.org/10.1126/science.1159775

Pavlov, I., & Walker, M. C. (2013). Tonic GABAA receptor-mediated signalling in temporal lobe epilepsy. In *Neuropharmacology* (Vol. 69, pp. 55–61). Pergamon. https://doi.org/10.1016/j.neuropharm.2012.04.003

Paz, J. T., Davidson, T. J., Frechette, E. S., Delord, B., Parada, I., Peng, K., Deisseroth, K., & Huguenard, J. R. (2013). Closed-loop optogenetic control of thalamus as a tool for interrupting seizures after cortical injury. *Nature Neuroscience*, *16*(1), 64–70. https://doi.org/10.1038/nn.3269

Paz, J. T., & Huguenard, J. R. (2015). Microcircuits and their interactions in epilepsy: Is the focus out of focus? *Nature Neuroscience*, *18*(3), 351–359. https://doi.org/10.1038/nn.3950

Petersen, C. C. H. (2017). Whole-Cell Recording of Neuronal Membrane Potential during Behavior. In *Neuron* (Vol. 95, Issue 6, pp. 1266–1281). Cell Press. https://doi.org/10.1016/j.neuron.2017.06.049

Phillips, R. S., John, T. T., Koizumi, H., Molkov, Y. I., & Smith, J. C. (2019). Biophysical mechanisms in the mammalian respiratory oscillator re-examined with a new data-driven computational model. *ELife*, *8*, e41555. https://doi.org/10.7554/eLife.41555

Portugal, R. D., & Svaiter, B. F. (2011). Weber-Fechner Law and the Optimality of the Logarithmic Scale. *Minds and Machines*, *21*(1), 73–81. https://doi.org/10.1007/s11023-010-9221-z

Pouille, F., & Scanziani, M. (2004). Routing of spike series by dynamic circuits in the hippocampus. *Nature*, *429*(6993), 717–723. https://doi.org/10.1038/nature02615

Poulter, S., Hartley, T., & Lever, C. (2018). The Neurobiology of Mammalian Navigation. *Current Biology*, *28*(17), R1023–R1042. https://doi.org/10.1016/j.cub.2018.05.050

Prince, D. A., & Connors, B. W. (1984). Mechanisms of epileptogenesis in cortical structures. *Annals of Neurology*, *16*(1 S), S59–S64. https://doi.org/10.1002/ana.410160710

Rolotti, S. V., Blockus, H., Sparks, F. T., Priestley, J. B., & Losonczy, A. (2022). Reorganization of CA1 dendritic dynamics by hippocampal sharp-wave ripples during learning. *Neuron*, S0896627321010345. https://doi.org/10.1016/j.neuron.2021.12.017

Roxin, A., Brunel, N., Hansel, D., Mongillo, G., & van Vreeswijk, C. (2011). On the Distribution of Firing Rates in Networks of Cortical Neurons. *Journal of Neuroscience*, *31*(45), 16217–16226. https://doi.org/10.1523/JNEUROSCI.1677-11.2011

Rubin, J. E., Hayes, J. A., Mendenhall, J. L., & Del Negro, C. A. (2009). Calcium-activated nonspecific cation current and synaptic depression promote network-dependent burst oscillations. *Proceedings of the National Academy of Sciences*, *106*(8), 2939–2944. https://doi.org/10.1073/pnas.0808776106

Rubin, J. E., Shevtsova, N. A., Ermentrout, G. B., Smith, J. C., & Rybak, I. A. (2009). Multiple Rhythmic States in a Model of the Respiratory Central Pattern Generator. *Journal of Neurophysiology*, *101*(4), 2146–2165. https://doi.org/10.1152/jn.90958.2008

Rubin, J., & Smith, J. (2019). *Robustness of respiratory rhythm generation across dynamic regimes* [Preprint]. Neuroscience. https://doi.org/10.1101/549444

Rudy, B., Fishell, G., Lee, S. H., & Hjerling-Leffler, J. (2011). Three groups of interneurons account for nearly 100% of neocortical GABAergic neurons. *Developmental Neurobiology*, *71*(1), 45–61. https://doi.org/10.1002/dneu.20853

Rudy, B., & McBain, C. J. (2001). Kv3 channels: Voltage-gated K+ channels designed for high-frequency repetitive firing. In *Trends in Neurosciences* (Vol. 24, Issue 9, pp. 517–526). https://doi.org/10.1016/S0166-2236(00)01892-0

Sabolek, H. R., Swiercz, W. B., Lillis, K. P., Cash, S. S., Huberfeld, G., Zhao, G., Ste. Marie, L., Clemenceau, S., Barsh, G., Miles, R., & Staley, K. J. (2012). A candidate mechanism underlying the variance of interictal spike propagation. *Journal of Neuroscience*, *32*(9), 3009–3021. https://doi.org/10.1523/JNEUROSCI.5853-11.2012

Samsonovich, A., & McNaughton, B. L. (1997). Path Integration and Cognitive Mapping in a Continuous Attractor Neural Network Model. *The Journal of Neuroscience*, *17*(15), 5900–5920. https://doi.org/10.1523/JNEUROSCI.17-15-05900.1997

Schevon, C. A., Weiss, S. A., McKhann, G., Goodman, R. R., Yuste, R., Emerson, R. G., & Trevelyan, A. J. (2012). Evidence of an inhibitory restraint of seizure activity in humans. *Nature Communications*, *3*, 1060. https://doi.org/10.1038/ncomms2056

Schlesiger, M. I., Cannova, C. C., Boublil, B. L., Hales, J. B., Mankin, E. A., Brandon, M. P., Leutgeb, J. K., Leibold, C., & Leutgeb, S. (2015). The medial entorhinal cortex is necessary for temporal organization of hippocampal neuronal activity. *Nature Neuroscience*, *18*(8), 1123–1132. https://doi.org/10.1038/nn.4056

Schmidt, R., Diba, K., Leibold, C., Schmitz, D., Buzsáki, G., & Kempter, R. (2009). Single-Trial Phase Precession in the Hippocampus. *Journal of Neuroscience*, *29*(42), 13232–13241. https://doi.org/10.1523/JNEUROSCI.2270-09.2009

Schomburg, E. W., Fernández-Ruiz, A., Mizuseki, K., Berényi, A., Anastassiou, C. A., Koch, C., & Buzsáki, G. (2014). Theta Phase Segregation of Input-Specific Gamma Patterns in Entorhinal-Hippocampal Networks. *Neuron*, *84*(2), 470–485. https://doi.org/10.1016/j.neuron.2014.08.051

Schwartzkroin, P. A., & Prince, D. A. (1980). Changes in excitatory and inhibitory synaptic potentials leading to epileptogenic activity. *Brain Research*, *183*(1), 61–77. https://doi.org/10.1016/0006-8993(80)90119-5

Sessolo, M., Marcon, I., Bovetti, S., Losi, G., Cammarota, M., Ratto, G. M., Fellin, T., & Carmignoto, G. (2015). Parvalbumin-positive inhibitory interneurons oppose

propagation but favor generation of focal epileptiform activity. *Journal of Neuroscience*, *35*(26), 9544–9557. https://doi.org/10.1523/JNEUROSCI.5117-14.2015

Shen, E., Wang, R., & Zhang, Z. (2008). Theta Phase Precession Enhance Single Trial Learning in an STDP Network. In R. Wang, E. Shen, & F. Gu (Eds.), *Advances in Cognitive Neurodynamics ICCN 2007* (pp. 109–114). Springer Netherlands.

Silva, F. L. D., Blanes, W., Kalitzin, S. N., Parra, J., Suffczynski, P., & Velis, D. N. (2003). Epilepsies as Dynamical Diseases of Brain Systems: Basic Models of the Transition Between Normal and Epileptic Activity. *Epilepsia*, *44*(s12), 72–83. https://doi.org/10.1111/j.0013-9580.2003.12005.x

Sloin, H. E., Levi, A., Someck, S., Spivak, L., & Stark, E. (2022). High Fidelity Theta Phase Rolling of CA1 Neurons. *Journal of Neuroscience*, *42*(15), 3184–3196. https://doi.org/10.1523/JNEUROSCI.2151-21.2022

Smith, J. C., Abdala, A. P. L., Borgmann, A., Rybak, I. A., & Paton, J. F. R. (2013). Brainstem respiratory networks: Building blocks and microcircuits. *Trends in Neurosciences*, *36*(3), 152–162. https://doi.org/10.1016/j.tins.2012.11.004

Smith, J. C., Abdala, A. P. L., Rybak, I. A., & Paton, J. F. R. (2009). Structural and functional architecture of respiratory networks in the mammalian brainstem. *Philosophical Transactions of the Royal Society B: Biological Sciences*, *364*(1529), 2577–2587. https://doi.org/10.1098/rstb.2009.0081

Somjen, G. G. (2004). *Ions in the Brain: Normal Function, Seizures, and Stroke*. Oxford University Press, USA.

Souza, B. C., & Tort, A. B. L. (2017). Asymmetry of the temporal code for space by hippocampal place cells. *Scientific Reports*, *7*(1). https://doi.org/10.1038/s41598-017-08609-3

Sritharan, D., & Sarma, S. V. (2014). Fragility in Dynamic Networks: Application to Neural Networks in the Epileptic Cortex. *Neural Computation*, *26*(10), 2294–2327. https://doi.org/10.1162/NECO_a_00644

Stemmler, M., Mathis, A., & Herz, A. V. M. (2015). Connecting multiple spatial scales to decode the population activity of grid cells. *Science Advances*, *1*(11), e1500816. https://doi.org/10.1126/science.1500816

Stensola, H., Stensola, T., Solstad, T., Frøland, K., Moser, M.-B., & Moser, E. I. (2012). The entorhinal grid map is discretized. *Nature*, *492*(7427), 72–78. https://doi.org/10.1038/nature11649

Sukhotinsky, I., Chan, A. M., Ahmed, O. J., Rao, V. R., Gradinaru, V., Ramakrishnan, C., Deisseroth, K., Majewska, A. K., & Cash, S. S. (2013). Optogenetic Delay of Status Epilepticus Onset in an In Vivo Rodent Epilepsy Model. *PLoS ONE*, *8*(4). https://doi.org/10.1371/journal.pone.0062013

Tank, D. W., & Hopfield, J. J. (1987). Neural computation by concentrating information in time. *Proceedings of the National Academy of Sciences*, *84*(7), 1896–1900. https://doi.org/10.1073/pnas.84.7.1896

Thurman, D. J., Beghi, E., Begley, C. E., Berg, A. T., Buchhalter, J. R., Ding, D., Hesdorffer, D. C., Hauser, W. A., Kazis, L., Kobau, R., Kroner, B., Labiner, D., Liow, K., Logroscino, G., Medina, M. T., Newton, C. R., Parko, K., Paschal, A., Preux, P.-M., … Wiebe, S. (2011).

Standards for epidemiologic studies and surveillance of epilepsy. *Epilepsia*, *52*(SUPPL. 7), 2–26. https://doi.org/10.1111/j.1528-1167.2011.03121.x

Tingley, D., & Buzsáki, G. (2018). Transformation of a Spatial Map across the Hippocampal-Lateral Septal Circuit. *Neuron*, *98*(6), 1229-1242.e5. https://doi.org/10.1016/j.neuron.2018.04.028

Tolman, E. C. (1948). Cognitive maps in rats and men. *Psychological Review*, *55*(4), 189–208. https://doi.org/10.1037/h0061626

Trevelyan, A. J., & Schevon, C. A. (2013). How inhibition influences seizure propagation. *Neuropharmacology*, *69*, 45–54. https://doi.org/10.1016/j.neuropharm.2012.06.015

Trevelyan, A. J., Sussillo, D., & Yuste, R. (2007). Feedforward Inhibition Contributes to the Control of Epileptiform Propagation Speed. *The Journal of Neuroscience*, *27*(13), 3383–3387. https://doi.org/10.1523/JNEUROSCI.0145-07.2007

Truccolo, W., Ahmed, O. J., Harrison, M. T., Eskandar, E. N., Cosgrove, G. R., Madsen, J. R., Blum, A. S., Potter, N. S., Hochberg, L. R., & Cash, S. S. (2014). Neuronal Ensemble Synchrony during Human Focal Seizures. *Journal of Neuroscience*, *34*(30), 9927–9944. https://doi.org/10.1523/JNEUROSCI.4567-13.2014

Truccolo, W., Donoghue, J. A., Hochberg, L. R., Eskandar, E. N., Madsen, J. R., Anderson, W. S., Brown, E. N., Halgren, E., & Cash, S. S. (2011). Single-neuron dynamics in human focal epilepsy. *Nature Neuroscience*, *14*(5), 635–641. https://doi.org/10.1038/nn.2782

Tsodyks, M. V., Skaggs, W. E., Sejnowski, T. J., & McNaughton, B. L. (1996). Population dynamics and theta rhythm phase precession of hippocampal place cell firing: A spiking neuron

model. *Hippocampus*, *6*(3), 271–280. https://doi.org/10.1002/(SICI)1098-1063(1996)6:3<271::AID-HIPO5>3.0.CO;2-Q

Vogels, T. P., Rajan, K., & Abbott, L. F. (2005). *NEURAL NETWORK DYNAMICS*. 22.

Wang, X.-J. (2010). Neurophysiological and Computational Principles of Cortical Rhythms in Cognition. *Physiological Reviews*, *90*(3), 1195–1268. https://doi.org/10.1152/physrev.00035.2008

Wang, Y., Romani, S., Lustig, B., Leonardo, A., & Pastalkova, E. (2015). Theta sequences are essential for internally generated hippocampal firing fields. *Nature Neuroscience*, *18*(2), 282–288. https://doi.org/10.1038/nn.3904

Wei, X.-X., Prentice, J., & Balasubramanian, V. (2015). A principle of economy predicts the functional architecture of grid cells. *ELife*, *4*, e08362. https://doi.org/10.7554/eLife.08362

Weiss, S. A., Alvarado-Rojas, C., Bragin, A., Behnke, E., Fields, T., Fried, I., Engel, J., & Staba, R. (2016). Ictal onset patterns of local field potentials, high frequency oscillations, and unit activity in human mesial temporal lobe epilepsy. *Epilepsia*, *57*(1), 111–121. https://doi.org/10.1111/epi.13251

Wikenheiser, A. M., & Redish, A. D. (2015a). Hippocampal theta sequences reflect current goals. *Nature Neuroscience*, *18*(2), 289–294. https://doi.org/10.1038/nn.3909

Wikenheiser, A. M., & Redish, A. D. (2015b). Decoding the cognitive map: Ensemble hippocampal sequences and decision making. *Current Opinion in Neurobiology*, *32*, 8–15. https://doi.org/10.1016/j.conb.2014.10.002

Wykes, R. C., Heeroma, J. H., Mantoan, L., Zheng, K., MacDonald, D. C., Deisseroth, K., Hashemi, K. S., Walker, M. C., Schorge, S., & Kullmann, D. M. (2012). Epilepsy: Optogenetic and potassium channel gene therapy in a rodent model of focal neocortical epilepsy. *Science Translational Medicine*, *4*(161). https://doi.org/10.1126/scitranslmed.3004190

Xu, H., Jeong, H. Y., Tremblay, R., & Rudy, B. (2013). Neocortical Somatostatin-Expressing GABAergic Interneurons Disinhibit the Thalamorecipient Layer 4. *Neuron*, *77*(1), 155–167. https://doi.org/10.1016/j.neuron.2012.11.004

Yamaguchi, Y., Aota, Y., Mcnaughton, B. L., Lipa, P., Neurophysiol, J., Yamaguchi, Y., Aota, Y., Mcnaughton, B. L., Lipa, P., Aota, Y., & Mcnaughton, B. L. (2001). Bimodality of theta phase precession in hippocampal place cells in freely running rats. *J. Neurophysiol*, 2642.

Yuste, R., MacLean, J. N., Smith, J., & Lansner, A. (2005). The cortex as a central pattern generator. *Nature Reviews Neuroscience*, *6*(6), 477–483. https://doi.org/10.1038/nrn1686

Zemel, R. S., Dayan, P., & Pouget, A. (1997). Probabilistic Interpretation of Population Codes. In M. C. Mozer, M. I. Jordan, & T. Petsche (Eds.), *Advances in Neural Information Processing Systems 9* (pp. 676–684). MIT Press. http://papers.nips.cc/paper/1324-probabilistic-interpretation-of-population-codes.pdf

Zhang, L., Lee, J., Rozell, C., & Singer, A. C. (2019). Sub-second dynamics of theta-gamma coupling in hippocampal CA1. *ELife*, *8*, e44320. https://doi.org/10.7554/eLife.44320

Zhang, Z. J., Koifman, J., Shin, D. S., Ye, H., Florez, C. M., Zhang, L., Valiante, T. A., & Carlen, P. L. (2012). Transition to Seizure: Ictal Discharge Is Preceded by Exhausted Presynaptic GABA

Release in the Hippocampal CA3 Region. *Journal of Neuroscience*, *32*(7), 2499–2512. https://doi.org/10.1523/JNEUROSCI.4247-11.2012

Zheng, C., Bieri, K. W., Hsiao, Y.-T., & Colgin, L. L. (2016). Spatial Sequence Coding Differs during Slow and Fast Gamma Rhythms in the Hippocampus. *Neuron*, *89*(2), 398–408. https://doi.org/10.1016/j.neuron.2015.12.005

Zheng, C., Bieri, K. W., Trettel, S. G., & Colgin, L. L. (2015). The relationship between gamma frequency and running speed differs for slow and fast gamma rhythms in freely behaving rats. *Hippocampus*, *25*(8), 924–938. https://doi.org/10.1002/hipo.22415

Ziburkus, J., Cressman, J. R., Barreto, E., & Schiff, S. J. (2006). Interneuron and Pyramidal Cell Interplay During In Vitro Seizure-Like Events. *Journal of Neurophysiology*, *95*(6), 3948–3954. https://doi.org/10.1152/jn.01378.2005

Žiburkus, J., Cressman, J. R., & Schiff, S. J. (2012). Seizures as imbalanced up states: Excitatory and inhibitory conductances during seizure-like events. *Journal of Neurophysiology*, *109*(5), 1296–1306. https://doi.org/10.1152/jn.00232.2012

Žiburkus, J., Cressman, J. R., & Schiff, S. J. (2013). Seizures as imbalanced up states: Excitatory and inhibitory conductances during seizure-like events. *Journal of Neurophysiology*, *109*(5), 1296–1306. https://doi.org/10.1152/jn.00232.2012

Zilli, E. A., & Hasselmo, M. E. (2010). Coupled Noisy Spiking Neurons as Velocity-Controlled Oscillators in a Model of Grid Cell Spatial Firing. *Journal of Neuroscience*, *30*(41), 13850–13860. https://doi.org/10.1523/JNEUROSCI.0547-10.2010

Zutshi, I., Valero, M., Fernández-Ruiz, A., & Buzsáki, G. (2021). Extrinsic control and intrinsic computation in the hippocampal CA1 circuit. *Neuron*, S0896627321009533. https://doi.org/10.1016/j.neuron.2021.11.015